

**Flow visualisation and quantification using
high frame rate ultrasound imaging and
microbubble contrast agents**

Chee Hau Leow

Department of Bioengineering

Imperial College London

This dissertation is submitted for the degree of

Doctor of Philosophy

Declaration of Originality

I hereby declare that except where specific reference is made to the work of others, the contents of this dissertation are original and have not been submitted in whole or in part for consideration for any other degree or qualification. This dissertation is my own work unless otherwise attributed.

Chee Hau Leow

December 2016

Copyright Declaration

The copyright of this thesis rests with the author and is made available under a Creative Commons Attribution Non-Commercial No Derivatives licence. Researchers are free to copy, distribute or transmit the thesis on the condition that they attribute it, that they do not use it for commercial purposes and that they do not alter, transform or build upon it. For any reuse or redistribution, researchers must make clear to others the licence terms of this work

Acknowledgment

Firstly, I would like to express my sincere gratitude to my supervisor Dr Meng-Xing Tang for his continuous support of my PhD study and related research, for his patience, motivation and immense knowledge. His guidance helped me in all the time of research and writing of this thesis.

Besides my supervisor, many people have contributed to this thesis, which are included but may not be limited to those acknowledged below. I owe my acknowledge to Prof. Peter Weinberg and Dr Elene Bazigou for their help in setting-up the *in-vivo* animal experiments, Dr Alfred Yu and Billy Yiu from University of Waterloo for providing the *in-vitro* flow phantom and useful discussion on the image beamforming, Prof Colin Caro, Dr Peter Vincent, Dr Richard Corbett, Dr Neil Duncan and Francesco Iori for their contributions in Microbubble Void Imaging study. Without their helps, much of the work presented in this thesis would not have been successful.

I would also like to thank all the members of Ultrasound Imaging and Sensing Group from Imperial College London and Ultrasound Imaging Group from King's College London, Dr Robert Eckersley, Prof. David Cosgrove, Dr James Choi, Prof. Kim Parker for their stimulating discussions and useful feedbacks. My appreciations also go to Dr Meng-Xing Tang and Yuanwei Li for their help in thorough proof-reading and corrections on this thesis.

Last but not least, I would like to thank my family: my parents, grandmother, brothers and sisters, and my beloved girlfriend, Chi Ching Lau, for all their love and supports.

Abstract

Non-invasive techniques capable of visualising and quantifying blood flow *in-vivo* are highly desirable in studying a wide range of cardiovascular diseases. Although existing ultrasound imaging techniques have been widely used clinically to visualise and quantify blood flow, they have various limitations in terms of field of view, temporal and spatial resolution, imaging sensitivity, and beam-flow angle dependence. In this thesis, our aim is to develop flow quantification tools capable of non-invasively measuring the flow velocity, wall shear stress (WSS) as well as intraluminal mixing.

Firstly, a high frame-rate ultrasound imaging velocimetry (UIV) system was developed based on tracking the speckle patterns of microbubble contrast agents in contrast-enhanced ultrasound image sequences acquired from a plane wave imaging system. Initial evaluation of the system demonstrated the potential of the new system as a flow velocity mapping tool capable of tracking fast and dynamic flow and we improved our flow velocity measurement technique by introducing an incoherent ensemble correlation approach in the UIV tracking algorithm. Such a modified UIV technique avoids the motion artifact which could potentially affect the velocity measurement as compounded plane wave images are not coherently summed during the compounded plane wave image formation. Ultrasound flow simulations were conducted to fully evaluate our new modified-UIV technique. Together with some *in-vitro* experiments on physiologically relevant flow phantoms, we demonstrated the capability of our system to provide robust, angle independent, sensitive, and accurate two-dimensional velocity measurements.

Secondly, as studies have revealed strong correlation between WSS and the initiation and development of atherosclerosis, we extended our UIV technique to the derive spatio-temporal wall shear rate from the velocity flow profile. The performance of the system to provide wall

shear stress distributions was initially evaluated in simulation and demonstrated *in-vitro* using physiologically relevant flow phantoms.

Thirdly, a novel approach which uses the high frame rate system and controlled microbubble destruction for flow visualisation and intraluminal mixing quantification was also proposed. Three different model vessel geometries: straight, planar curved and helical, with known effects on the flow field and mixing were evaluated against computational fluid dynamics (CFD) results. The findings indicated the technique is not only capable of visualising the secondary flows, but also able to quantify the degree of mixing in the different configurations.

Finally, real time processing of the image formation and flow quantification technique were explored due to the large amount of data generated from the high frame rate ultrasound system. Initial development of a graphic processing unit (GPU) accelerated plane wave UIV system was demonstrated with the potential for real time measurements.

Table of Contents

Declaration of Originality	ii
Copyright Declaration	iii
Acknowledgment.....	iv
Abstract.....	v
Table of Contents	vii
List of Tables	xii
List of Figures.....	xiii
Chapter 1 – Introduction.....	1
1.1 Arteriosclerosis and the role of hemodynamics	1
1.2 Ultrasound imaging	2
1.2.1 Conventional ultrasound	3
1.2.2 Synthetic Aperture	5
1.2.3 Plane wave ultrasound	7
1.3 Ultrasound Contrast Imaging	8
1.3.1 Microbubbles Contrast Agent	9
1.4 Ultrasound techniques of measuring blood flow.....	12
1.4.1 Doppler-based technique	12
1.4.2 Non-Doppler techniques	15
1.5 Other imaging modalities	17
1.6 Ultrasound Imaging Velocimetry (UIV).....	17

1.6.1	Background and Principle of UIV	17
1.6.2	Current limitations of UIV	22
1.7	Purpose and Thesis Structure	23
1.8	Scientific contributions	25
Chapter 2 - Initial development of flow velocity mapping using plane wave UIV.....		27
2.1	Introduction	27
2.2	Methods and Material.....	29
2.2.1	Microbubbles Contrast Agents	29
2.2.2	Fast ultrasound imaging system and Pulse Inversion	30
2.2.3	UIV Analysis	31
2.2.4	Straight vessel flow phantom.....	32
2.2.5	<i>In-vitro</i> Carotid Bifurcation Model.....	35
2.2.6	<i>In vivo</i> Rabbit Experiment	36
2.3	Results	36
2.3.1	Straight vessel phantom	36
2.3.2	Carotid Bifurcation Model.....	42
2.3.3	Rabbit.....	44
2.4	Discussion	46
2.5	Conclusion.....	50
Chapter 3 - Toward a reliable and accurate flow velocity measurement using plane wave UIV		51
3.1	Introduction	51

3.2	Methods.....	54
3.2.1	Velocity Estimation using a modified UIV analysis.....	54
3.2.2	Ultrasound Flow Simulation.....	56
3.2.3	In vitro flow experiment	61
3.2.4	Error Quantification.....	63
3.3	Results.....	64
3.3.1	Poiseuille Flow Simulation.....	64
3.3.2	Pulsatile Flow Simulation.....	68
3.3.3	In-vitro flow experiments	73
3.4	Discussion	78
3.5	Conclusion.....	81
Chapter 4 - Accuracy of Plane wave UIV for Wall Shear Stress measurement		82
4.1	Introduction	82
4.2	Methods.....	84
4.2.1	Wall shear rate estimation.....	84
4.2.2	Ultrasound flow simulation.....	86
4.2.3	In-vitro flow experiments	86
4.2.4	WSR Assessment.....	87
4.3	Results.....	87
4.3.1	Ultrasound flow simulation.....	87
4.3.2	In-vitro WSR measurements.....	93

4.4	Discussion	95
4.5	Conclusion.....	98
Chapter 5 - Microbubbles void imaging		99
5.1	Introduction	100
5.2	Methods.....	103
5.2.1	Experimental flow set up	103
5.2.2	Microbubble contrast agent.....	106
5.2.3	Void creation by bubble destruction	106
5.2.4	Ultrasound imaging.....	107
5.2.5	Ultrasound image enhancement.....	107
5.2.6	Computational fluid dynamics.....	108
5.3	Results	113
5.3.1	Microbubble void concentration	113
5.3.2	Mixing evaluation	115
5.4	Discussion	117
5.5	Conclusion.....	120
Chapter 6 - Graphics Processing Unit (GPU) accelerated ultrasound image beamforming and UIV tracking		121
6.1	Introduction	121
6.2	Methods.....	123
6.2.1	Overview.....	123
6.2.2	Computation Platform.....	127

6.2.3	CPU implementation.....	127
6.2.4	GPU implementation	128
6.3	Results	130
6.3.1	Plane wave image reconstruction.....	130
6.3.2	UIV analyses.....	133
6.4	Discussion	135
6.5	Conclusion.....	137
Chapter 7 - Conclusion and future work.....		138
7.1	Summary and conclusions.....	138
7.2	Future works.....	140
Bibliography		143

List of Tables

Table 1.1: Multipulse techniques used to detect non-linear microbubble signal. Adapted from [61].....	12
Table 1.2: Three-point estimator for determining the subpixel displacement from the correlation peak[102].....	19
Table 2.1: Flow parameters of 3 different laminar flows	34
Table 2.2: Comparison of the peak velocity measurement estimated from spectral doppler and UIV with the analytical velocities.....	37
Table 3.1: Flow parameters of 3 simulated laminar flows.....	57
Table 3.2: Fourier components for flow velocities in the common carotid artery and common femoral artery. (Data adapted from Evans[168]).....	58
Table 3.3: Field II simulation setup	60
Table 3.4: Ultrafast imaging data acquisition configurations.....	62
Table 3.5: Accuracy of the normal UIV and the modified-UIV approach a under different flow rates. Note that the error is calculated based on the radial velocity profile.....	67
Table 3.6: Accuracy of the normal UIV and the modified-UIV approach under different beam-to-flow angle. Note that the error is calculated based on the radial velocity profile	68
Table 3.7: Accuracy of the normal UIV and the modified UIV approach under different simulated artery.....	71
Table 4.1: Error analysis on the estimated wall shear rate	92
Table 5.1: Estimated set of parameters for $\hat{\sigma}(x)$	111
Table 6.1: Field II simulation setup	132

List of Figures

Figure 1.1: Delay-and-sum receive focusing in a conventional ultrasound system. Adapted from [16].....	4
Figure 1.2: Optimum focus (f) achieved by blending several focal zones (a-e) with several transmissions. Adapted from [17].....	4
Figure 1.3: Principle of synthetic transmit aperture ultrasound imaging. Adapted from [22] ..	6
Figure 1.4: Basic principle of single plane wave imaging: (a) A pulse plane wave transmitted by exciting all elements; (b) The backscattered echoes recorded by the transducer array. (c) Dynamic beamforming of plane-wave imaging. Adapted from [50].	8
Figure 1.5: Basic principle of UIV	18
Figure 1.6: Multi-grid iterative window deformation technique in which interrogations are progressively deformed according to the velocity field measured from the previous iteration. [102].....	21
Figure 1.7: Ensemble correlation technique in which multiple instantaneous correlation planes are averaged to enhance the peak detectability and signal to noise ratio[112].....	22
Figure 2.1: Overview of the system hardware and data acquisition scheme involve in plane wave UIV.....	31
Figure 2.2: The basic workflow of UIV algorithm.....	32
Figure 2.3: Schematic of the straight tube flow system.....	33
Figure 2.4: (a) Schematic of the carotid bifurcation experimental setup. (b) Carotid bifurcation tube without stenosis.	35
Figure 2.5: <i>In vivo</i> experimental set up. Contrast agents were injected through the anaesthetised rabbit's ear and the rabbit abdominal aorta was scanned using an L12-3 probe.	36
Figure 2.6: Comparison of Doppler ultrasound with plane wave UIV under 3 flow rates with peak velocities of 10cm/s, 38cm/s and 59cm/s. (a)-(c) Colour Doppler obtained using standard beam-formed colour Doppler processing. (d)-(f) Spectral Doppler measurements acquired from the corresponding window located in the colour images. The red line indicates the maximum velocity. (g)-(i) UIV derived quantitative vector visualization. Each	

measurement is averaged over 5 ms. (j)-(l) Measured flow profiles corresponding to the three flow conditions show a high correlation with the analytical derived flow profile (dashed line). Note: results in (j)-(l) were averaged over a 1mm lateral position where the solid line represents the mean value and the shading represents the standard deviation.39

Figure 2.7: Visualization and quantification of pulsatile flow at the four phases indicated by dotted lines in (m). (a)-(d) Colour Doppler measurement acquired at the 4 different phases. (e)-(h) Colour vector of flow measurements obtained using plane wave UIV, and their corresponding flow profiles (i)-(l). (m) Comparison of centreline velocity obtained from plane wave UIV (blue line) with spectral Doppler. Note: results shown in (i)-(l) were averaged over a 1mm lateral position where the solid line represents the mean value and the shading represents the standard deviation. Spectral Doppler measurement and plane wave UIV results shown in (m) were averaged over a 1mm x 1mm window located at the centre of the vessel.41

Figure 2.8: (a)-(f) Quantitative visualization of key flow patterns obtained at different phases under pulsatile conditions in a model of a healthy carotid bifurcation. (g) Centreline velocity obtained using UIV from a 1 x 1 mm range gate located within the CCA. The relative time positions of each flow pattern are marked in the velocity plot.43

Figure 2.9: (a)-(d) Quantitative visualisation of the flow patterns within a rabbit aorta. (e) Centreline velocity plot obtained using UIV from a 1 x 1mm range gate within the aorta. The relative positions of each flow pattern are marked in the velocity plot.44

Figure 2.10: Comparison of (a) a colour Doppler image, (b) quantitative visualisation of flow patterns estimated using UIV analysis and (c) centreline velocity extracted from a 1 x 1mm range gate within the aorta shown in (b).45

Figure 3.1: (a) Compounded plane wave image at the peak systole shows the motion artefacts at the stenosed bifurcations area due to high velocity flow. (b) Flow velocity vectors estimated using normal UIV shows significant underestimation of the jet flow due to the presence of motion artefacts in the compounded plane wave images.53

Figure 3.2: (a) Basic workflow of our modified UIV analysis to generate velocity mapping overlaid on the high resolution images (HRI) (b) Principle of incoherent ensemble-correlation approach where cross-correlation is applied to each pair of low resolution images (LRI) to generate an average correlation with higher signal to noise ratio and peak detectability.55

Figure 3.3: A scatterer model consisting of stationary vessel wall scatterers (yellow) and moving flow scatterers(blue).60

Figure 3.4: The effects of flow velocity on the compounded plane wave image quality.65

Figure 3.5: Flow velocity vectors estimated using normal (left) and modified UIV(right) under slow, medium and fast flow. The tube is tilted in an angle of 60^0 to the ultrasound beam.66

Figure 3.6: (a-d) Snapshots of the flow velocity vectors derived using the modified ultrasound imaging velocimetry (UIV) method obtained at different phases in a simulated common carotid artery. (e) Comparison of the centreline velocity estimated using the UIV method and the analytical ground truth. The relative time of each flow pattern is marked in the centreline velocity plot and the shading in the UIV measurement represents the standard deviation.69

Figure 3.7: (a-d) Quantitative flow measurements of the modified ultrasound imaging velocimetry (UIV) obtained at four phases in a simulated common femoral artery (e) Estimated centreline velocity overlaid on the ground truth solution to show the accuracy of UIV. The relative time of each flow pattern is marked in the centreline velocity plot and the shading in UIV measurement represents the standard deviation.70

Figure 3.8: Flow velocity vectors before and after the spurious vectors elimination process. Note that the red vectors are the velocity estimations replaced after the spatial filtering.72

Figure 3.9: Temporal variation of the normalised root mean square error (NRMSE) calculated using the normal UIV and modified UIV in a simulated common carotid artery (CCA) and a common femoral artery (CFA).72

Figure 3.10: Key quantitative velocity measurements derived from modified ultrasound imaging velocimetry (UIV) to highlight the spatio-temporal varying flow profile in (a-d) a healthy carotid bifurcation phantom; (f-i) a diseased carotid bifurcation phantom. (e,j) Centreline velocity extracted from the common carotid artery. The relative position of each flow velocity is marked in the velocity plot.....75

Figure 3.11: Quantitative flow velocity extracted from the yellow boxes depicted in the streamline images on a healthy and diseased carotid phantom. Note that the streamline images are generated from velocity estimation during diastole.....76

Figure 3.12: (a-d) Comparison of the flow velocity mapping at peak systole demonstrate the robustness of modified UIV approach to track highly-accelerated flow when similar amount

of high resolution images (N) are used to estimate the flow velocity. (e) Velocity plot extracted at the stenosed throat marked in (a)-(d). It should be noted that normal UIV approach estimate the flow using the final compounded images (N) but modified UIV analysis is performed on the multiple low resolution images ($M \times N$, and $M=3$) used to construct the same compounded image. 77

Figure 4.1: (a) Vector velocity mapping derived from the simulated steady flow. (b-c) Comparison of the analytical ground truth with the pre- and post- Savitzky-golay (SV) filter velocity profile and shear rate estimation. (d) Effects of filter length relative to the diameter of the tube and the filter order toward the WSR estimation error. n =filter length, dr =image resolution, D =vessel radial diameter..... 88

Figure 4.2: (a) Effect of estimated wall location error toward the WSR estimation error. (b) Shear rate profile corresponding to different wall locations which deviate from the ground truth location. 90

Figure 4.3: Quantitative measurements of the ultrasound imaging velocimetry (UIV) obtained at four different cardiac phases highlight the key flow patterns and wall shear rate distributions in (a-d) common carotid artery (CCA), (f-i) a common femoral artery (CFA). The centreline velocity of the (e) CCA and CFA are overlaid on the ground truth solution and the relative time of each flow pattern is marked in the centreline velocity plot. Note that the shading in UIV measurement in (e)&(j) represents the standard deviation..... 91

Figure 4.4: Spatial-averaged WSR estimation overlay on the analytical solution derived from the ground truth in (a) common carotid artery (CCA); (b) common femoral artery (CFA). ... 92

Figure 4.5: Key quantitative measurements derived from ultrasound imaging velocimetry (UIV) to highlight the spatio-temporal varying wall shear stress (WSS) distribution in (a-d) a healthy carotid bifurcation phantom; (f-i) a diseased carotid bifurcation phantom with 50% eccentric stenosis. (e,j) Inlet centreline velocity extracted from the common carotid artery in both carotid models. The relative times when the images are acquired is marked in the velocity plot. 94

Figure 5.1: Three geometries used as phantoms: L_E - entrance length, R_C - radius of curvature, A- location of microbubble destruction transducer, B- location of detection transducer, AB- path taken by microbubble void prior to detection and direction of flow ... 104

Figure 5.2: Illustration of the contrast enhancing filter used on data from a planar bend (a) raw data; (b) region of interest cropped from raw data; (c) Snapshot POD is calculated and

the image is reconstructed using the first n modes; (d) Contrast is enhanced using a sigmoid function 108

Figure 5.3: Ultrasound peak-to-peak pressure profile (dashed line) and the microbubble-void transition profile (dot-dash line) reconstructed from the fitted ultrasound beam profile function (solid line). Note that the left y-axis corresponds to the measured peak-to-peak ultrasound pressures and the fit function σx while right y-axis corresponds to the microbubble-void transition profile 111

Figure 5.4: A cross-sectional view of the O-grid used. The section was swept along the centrelines of each vessel to produce hexahedral cells 112

Figure 5.5: The arrival of the microbubble void observed by high frame-rate contrast enhanced ultrasound at different time points within an image plane along the vessel axis (left) and cross-sectional view (right). The elliptical dark wave front is the front of the evolved void (absence of bubbles) travelling along the vessel..... 113

Figure 5.6: Temporal snapshots of microbubble concentration in a plane orthogonal to the vessel centreline at different times. Images on the left are CFD solutions, whereas images on the right are ultrasound images after contrast enhancement. Note that the outer wall for the curved and helical tubes are on the left hand side, 114

Figure 5.7: Time evolution of entropy measure (S) calculated from CFD (solid line) and two experiments (dashed and dashed-dot lines) obtained using ultrasound imaging in different geometries: (a) straight, (b) curved and (c) helix 116

Figure 5.8: Peak entropy obtained over each time series (S_p) obtained using the experimental approach (twice) and the computational results for each geometry. 117

Figure 6.1: Principle workflow of image formation for coherent plane wave compounding technique. 124

Figure 6.2: Geometry associated with the delay calculation of the coherent plane wave compounding imaging technique..... 125

Figure 6.3: (b) Principle workflow of an advanced UIV analysis which incorporates the multigrid window deformation algorithm, the ensemble correlation approach and spurious vector elimination. 126

Figure 6.4: Schematic representation of CUDA threads and memory hierarchy [237]..... 129

Figure 6.5: (a) Images generated using the CPU and GPU implemented image reconstruction. (b-c) Axial plot and lateral plot of normalised signal intensity to compare the image resolution and signal to noise ratio. 131

Figure 6.6: Processing throughput of the plane wave image reconstruction using CPU and GPU. Note that the performance test was repeated for 5 times. 132

Figure 6.7: Vector images generated using (a) CPU implementation, (b) GPU implementation. (c) Comparison of the axial velocity profiles generated using different implementations.... 134

Figure 6.8: Comparison of the average processing time to generate single vector image using CPU- and GPU-based UIV implementation. 135

Chapter 1 – Introduction

1.1 Arteriosclerosis and the role of hemodynamics

Cardiovascular disease remains the major cause of mortality globally. The principle pathology is atherosclerosis, a long-term inflammation disease beginning at the artery wall and causing endothelial dysfunction. The inflammatory response, promoted by low-density lipoproteins (LDL), resulting in the thickening and hardening of vascular wall. The progressive accumulation of atheroma narrowing the artery and this can cause complete closure of the lumen. Stable plaques tend to be asymptomatic until the lumen stenosis is so severe that occlude the normal blood supply to the downstream tissues. Unstable plaques, on the other hand, are vulnerable and prone to rupture. Upon ruptures, the formation of thrombus can rapidly slow or stop the blood flow, but more often they detach, travel downstream and lead to thromboembolism.

Depending on the localization of atherosclerosis, marked narrowing of the arteries or rupture of plaques can lead to conditions such as heart attack, stroke, angina, peripheral arterial disease etc. Although risk factors such as genetic and environmental factors may predispose to the occurrence and progression of atherosclerosis[1], [2], the influence of the local vascular flow field toward the formation of atherosclerotic plaque has generated considerable interest[3], [4]. The occurrence of atherosclerotic plaques in regions of bifurcation, branching and curvature suggests that the arterial geometry and local hemodynamics have strong influence over the plaque formation[5]. Extensive numerical and experimental studies have been conducted to correlate the local flow field and the preferential site of atheroma[5]–[7]. Among their findings are that vascular lesions predominantly developed at regions where the blood flow is non-uniform and flow rate is relatively low. The magnitude and rate of change of blood flow near the vessel wall can be expressed in terms of wall shear stress and the

influence of the spatial and temporal wall shear stress distribution on the pathogenesis of atherosclerosis has been investigated. Evidences from *in-vitro* and *in-vivo* studies have demonstrated that the local sites which experience low and oscillatory wall shear stress were associated with atheroma formation and intimal wall thickening, whereas the regions with moderate to high shear stress was relatively uncommon for the lesion to develop[8], [9].

While arteriosclerosis develops preferentially at regions with low wall shear stress, studies in vessel wall mass transport provide better understanding on the underlying mechanism of the pathology[3], [10]. The flow-induced mechanical stresses can change the orientation and morphology of the vascular endothelial cells [11], alter their metabolic activities and gene expression[12], [13]. Disturbed flow with low and oscillatory wall shear stress induces the activation of atherogenic genes (eg. Monocyte chemotactic protein-1) which may result in endothelial cell dysfunction and inflammation, whereas uniform flow with high shear stress stimulates the release of atheroprotective genes and antioxidant that prevent coagulation, migration of leukocytes, and smooth muscle proliferation while promoting endothelial cell survival[10], [14]. Such observations are strong evidence that local hemodynamic factors are associated with vascular diseases; therefore, non-invasive imaging techniques capable of assessing hemodynamics *in-vivo* are most desirable in vascular disease diagnostics and treatment progression.

1.2 Ultrasound imaging

Ultrasound imaging has been extensively used clinically in both structural and functional imaging. Compared to other imaging modalities such as computed tomography (CT) and Magnetic Resonance Imaging (MRI), ultrasound is more accessible, safer, cheaper, and capable of real-time imaging. It is based on the principle of pulse-echo sequences. Generally, a short pulse is initially emitted from an array transducer. Depending on the bandwidth of the transducer, ultrasound pulses of a certain frequency and pulse length are transmitted to scan

the medium. When the acoustic wave interacts with the medium, either tissue or blood, it is transmitted, reflected or scattered according to the impedance mismatch of the medium structure. The echoes received by the same transducer are then beamformed into ultrasound images. Although the process of acquiring an ultrasound image can be simplified using the pulse-echo sequence, the working principle to form an ultrasound image, and its implementation in the beamformer, can be different between each imaging system.

1.2.1 Conventional ultrasound

Medical applications of ultrasound imaging can be traced back to the early 20th century. Using a single element transducer held in a stationary position, a one-dimensional scan was demonstrated to image soft tissue. This technique is known as an A-mode scan where the information is displayed as a function of depth or time, and amplitude of the enveloped detected signal is used to reveal the local difference in density and velocity. Similar to A-mode ultrasound, the B-mode scan was later introduced by mechanically sweeping the single element transducer to acquire 2D images. As technology developed, line-by-line acquisition using array transducer and electronic focusing have become a standard way to acquire B-mode images.

In the early ultrasound systems, the transmit and receive focus is fixed in a specific spatial location using a dedicated hardware beamformer. As a result, the image quality decreases as the beam generated only narrows in the vicinity of transmit focus and broadens when moving away from the focal point. It was soon discovered that dynamic receive focusing can significantly improve the image resolution across the imaging depth [15]. This technique allows data from multiple channels to delay-and-sum in such a way that signals at different depth are dynamically focussed as shown in Figure 1.1.

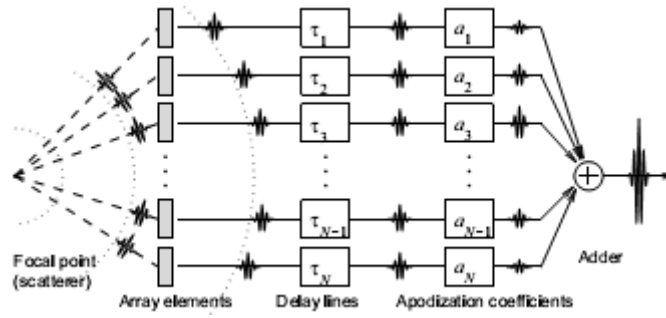


Figure 1.1: Delay-and-sum receive focusing in a conventional ultrasound system. Adapted from [16]

While dynamic receive focussing has been shown to improve the image resolution of conventional ultrasound imaging, spatial resolution is still fundamentally limited by the transmit focussing. To obtain optimum focus over the entire depth of the field, dynamic transmit focussing, also known as multi-zone transmit, was developed [17]. As illustrated in Figure 1.2, this technique relies on the transmission of several pulses, each focused at different depth, to form a single line image. Together with the dynamic receive focusing, multi-zone transmit focusing technique allows a higher image resolution across the depth, however, the imaging frame rate is reduced in proportion to the number of focal zones.

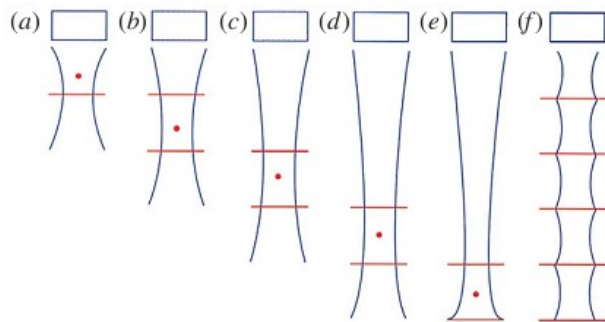


Figure 1.2: Optimum focus (f) achieved by blending several focal zones (a-e) with several transmissions. Adapted from [17]

1.2.2 Synthetic Aperture

Synthetic aperture imaging is an alternative way to improve the image quality and overcome the low temporal resolution limitation of a conventional ultrasound system. It was originally used in radar systems to obtain high resolution imaging by narrowing the antenna beam width using synthetic aperture. Instead of enlarging the physical antenna to enhance the cross-range resolution, a large antenna can be synthesised by sequentially examining the volume of interest with small real antenna moved along a known path. The idea of synthetic aperture was initially considered for medical ultrasound imaging due to the reduction of system complexity and cost. The classical mode of synthetic aperture ultrasound imaging is more or less a direct implementation of the classic synthetic aperture principle, known as monostatic synthetic aperture imaging [18], [19]. The system complexity is reduced since only a single element is active during each pulse-echo sequence, but it suffers from low SNR and poor contrast resolution. To overcome these problems, a synthetic receive aperture (SRA), in which pulses are transmitted from all the elements and a small receive aperture (one or several active elements) is used to form a single line of the image, was considered due to its hardware simplicity and the possibility for real time imaging [20], [21]. The transmitted beams are defocussed to emulate a single element response and dynamic receive focusing is performed to form a single line of image. Despite achieving a higher SNR, the frame rate of SRA imaging is reduced depending on the number of pulses transmitted to form an image line.

The most common synthetic aperture technique applied in ultrasonic imaging is synthetic transmit aperture (STA) and the principle of synthetic transmit aperture ultrasound imaging is illustrated in Figure 1.3. Unlike a conventional ultrasound system, a single element emits a spherical wave which covers the whole interrogation region. For each transmission, echoes are received by all the elements in the transducer and all the scan lines can be beamformed in

parallel. A low resolution image is created for each transmission as there is no focussing during the transmission and dynamic focussing is done solely in reception. Finally after the emission in the last element, all the low resolution images are summed coherently. As a result, virtual dynamic transmit focussing is synthesised during the coherent compounding and a high resolution image is created.

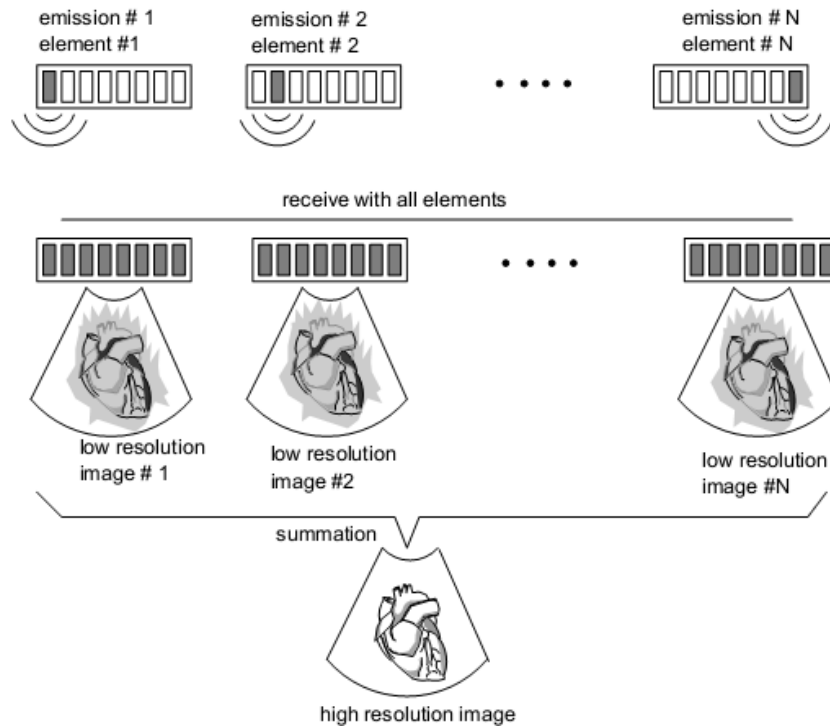


Figure 1.3: Principle of synthetic transmit aperture ultrasound imaging. Adapted from [22]

To speed up the acquisition process, sparse array synthetic transmit aperture (STA) [23]–[26], in which a sparse set of emissions is used for creating a full image, has been applied to increase the frame rate while maintaining the image resolution. A very fast imaging at the pulse repetition frequency can also be attained by using recursive imaging as demonstrated by Nikolov and colleagues[27]. Despite achieving a very high frame rate, the major problem of STA imaging is the limited penetration depth as an un-focussed wave is used and low energy is transmitted by single elements. To circumvent this problem, various techniques, such as multi-element STA [28], [29], spatial and temporal encoding STA [30]–[33], have been studied to increase penetration and SNR while maintaining the spatial resolution.

1.2.3 Plane wave ultrasound

The development of plane wave ultrasound is closely related to the progression of ultrafast ultrasound imaging where a large field-of-view can be achieved at thousands frames per second. The concept of ultrafast ultrasound imaging can be traced back to three decades ago where Brunnell and colleagues published a paper entitled “Ultrafast echotomographic system using optical processing of ultrasound signal”. Since then, several methodologies of ultrafast ultrasound imaging were devised and demonstrated, for example, through parallel beamforming processing of ultrasound images [34], [35], time-reversal processor[36], digital parallel receive beamforming[37]–[39], and non-diffraction beams[40], [41]. Despite having the capabilities of such imaging demonstrated more than 25 years ago, the ultrafast ultrasound system was not translated out of research labs until recently when the software beamformer technologies become available. [42]–[44].

Plane wave imaging is capable of imaging a large field-of-view with a single pulse-echo sequence [45], [46]. Conceptually, it is analogous to time-reversal ultrasound[39], a technique developed based on optical holography. A wide-field wave is transmitted to illuminate the entire FOV and the backscattered echoes are recorded on a transducer array. To re-create a virtual image representing the initial scattering object, time-reversal focusing or digital receive beamforming are utilised. The former involves re-emitting time-reversed echoes to build a wave-field that is refocused optimally on the original medium while the latter refocused the initial object in a numerical model of the propagation medium, assuming a constant speed of sound.

Figure 1.4 illustrates the principle of plane wave imaging. Contrary to conventional ultrasound imaging, the image can be reconstructed from a single pulse-echo sequence in plane wave imaging, achieving the highest frame rate that is only fundamentally limited by the speed of sound; however, compared to the conventional ultrasound imaging, plane wave

imaging has lower resolution and contrast. This is mainly due to the lack of transmit focussing in the image formation process. To overcome such problem, coherent spatial compounding, initially proposed in [47], has been applied to plane wave imaging to enhance the image quality[48]–[50]. Multiple plane waves are transmitted, each tilted at a different angle, are used to form low resolution images, and eventually coherently summed to synthesise a dynamically focussed high resolution image. A detailed investigation on the compounded plane wave imaging to improve image qualities in terms of resolution, contrast and signal to noise ratio is given in [50], [51]. Besides, it should be noted that such coherent compounding to form higher resolution image is analogous to the synthetic aperture imaging, but with better penetration as higher power is transmitted.

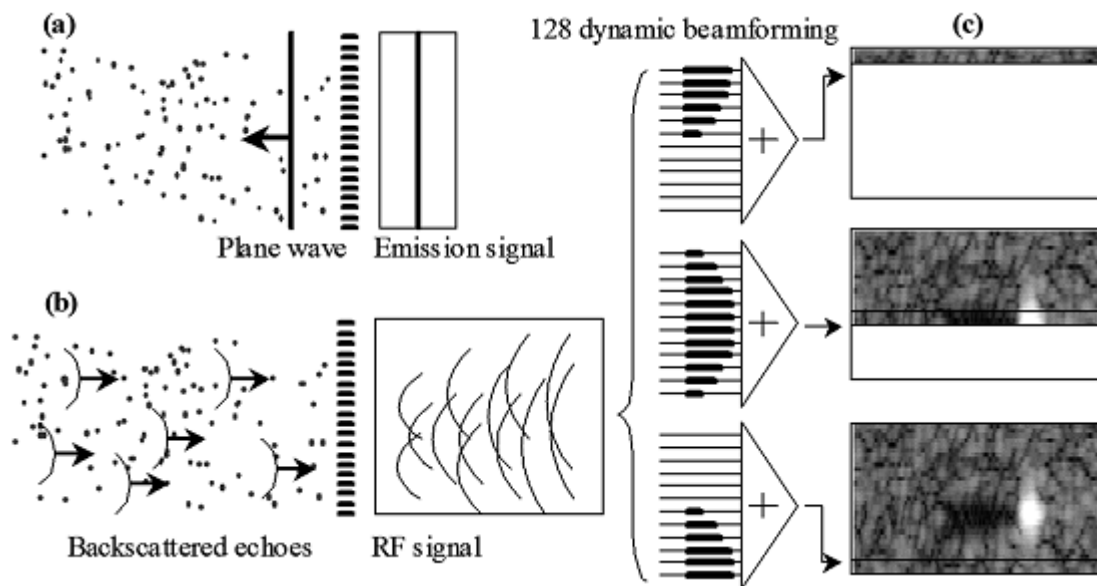


Figure 1.4: Basic principle of single plane wave imaging: (a) A pulse plane wave transmitted by exciting all elements; (b) The backscattered echoes recorded by the transducer array. (c) Dynamic beamforming of plane-wave imaging. Adapted from [50].

1.3 Ultrasound Contrast Imaging

Contrast imaging is a technique utilised in many imaging modalities to enhance image contrast with the use of contrast agents. In ultrasound imaging, microbubble contrast agents are used to increase imaging sensitivity by enhancing the scattering in areas where the

ultrasound signal is weak. As a result, it expands the diagnostic capabilities to detect smaller and deeper structures [52]. For instance, contrast agent has been used as blood pool agent to enhance cardiovascular structure, define anatomy, and quantify tissue perfusion. With the progressive development of contrast-specific imaging techniques and improvement in microbubbles, ultrasound contrast imaging has shown the potential to expand to broader range of diagnostic and therapeutic applications [53], [54].

1.3.1 Microbubbles Contrast Agent

Ultrasound contrast agents (UCA) are microbubbles (MBs) filled with gas and surrounded by a thin shell. Typically, it has average diameter of 1-8 μ m which is comparable to a red blood cell, and together with the shell, microbubbles can pass through the lung and survive in the circulation for enough time to allow a reproducible contrast effect.

Although air bubbles (without shell coating) can work as contrast agents, they diffuse quickly in the surrounding liquid and have limited lifetime. The stabilising shell (albumin, surfactant or phospholipids) and the gas content (air or perflouro gas) are critical to extend the lifetime of contrast agents in the circulation after injection in vivo. Over the years, several commercial microbubbles, such as Albunex, Optison, Levovist, Sonovue and Definity, have been developed and extensive reviews on the properties of these commercial microbubbles can be found in [55] and [56].

The response of microbubbles to an ultrasound field is more complex than the tissue due to its highly compressible properties. When an acoustic pulse insonates a microbubble, it forces the microbubble to expand and contract with the applied oscillating pressure. The strongest scattering effect occurs when the frequency of the ultrasound wave reaches the resonant frequency of the microbubble. With the size similar to a red blood cell, microbubbles resonate within the frequency range employed in diagnostic ultrasound. However, the

situation is complicated by the fact that the range in size may vary, and therefore result in a wide range of frequencies over which resonant behaviour may be observed.

Studies have shown that acoustic pressure is a major parameter affecting microbubble response and it has an important role in contrast imaging[57]. Since mechanical index (MI) is normally used in clinical ultrasound system to represent acoustic pressure, the response of microbubbles with acoustic pressure is discussed in the context of MI, which is defined as:

$$MI = \frac{P_r}{\sqrt{f}} \quad 1-1$$

where P_r is the peak negative pressure, and f is the transducer frequency. Principally, microbubble response can be divided into three domains when interacting with different acoustic pressures, and each domain results in a different type of image. At low MI, linear oscillation occurs where microbubbles oscillate symmetrically and the ultrasound is scattered with the same frequency as the incident wave. The acoustic response is optimised at the resonant frequency of the microbubbles and the strongly scattered echoes are used to enhance the contrast of B-mode and colour Doppler images.

At medium MI, microbubbles start to show non-linear behaviour, oscillating asymmetrically in a way that it expands more than it contracts. As a result, the ultrasound signal will be scattered in different magnitude and frequency. For an incident wave at the fundamental frequency (f_0), harmonics ($2f_0, 3f_0, 4f_0, \text{etc}$) and subharmonics ($f_0/2, f_0/3, f_0/4, \text{etc}$) can be observed in the backscattered signal. Despite a wide range of harmonics or subharmonics being generated, because the ultrasound transducer has limited bandwidth, normally only the second harmonic or subharmonic component is detected and used in harmonic imaging or subharmonic imaging to discriminate bubble from tissue[58]. The clinical potential of such response is further increased by the development of contrast specific imaging sequences that will be discussed in the following section.

At high MI, the microbubble shell is no longer able to sustain the non-linear oscillation. The gas is released from microbubbles when it ruptures and results in strongly scattered ultrasound signals with a wide range of frequencies. However, the scattering effect lasts only for a few frames as the gas will dissolve rapidly into the bloodstream. This type of imaging is known as intermittent imaging, and combined with B-mode, Doppler or harmonic imaging, has been used *in-vivo* to investigate myocardial perfusion[59].

1.3.2 Contrast Specific Imaging

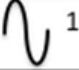




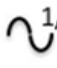

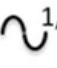

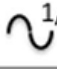

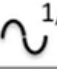

Current techniques for imaging microbubbles rely predominantly on separating the different frequency components from tissue and microbubbles. Initially, harmonic imaging is developed to detect bubble signal for contrast-enhanced imaging and it relies on simple high pass filtering techniques to extract the harmonic microbubble signals from the surrounding tissue which consists predominantly of linear signals. However, it is difficult to completely separate the broadband fundamental signal from the second harmonic signal within the limited bandwidth. Therefore, a typical compromise needs to be made between image contrast and spatial resolution[57]. In the attempt to overcome such limitations, the emergence of multi-pulse sequence imaging techniques has shown the feasibility to provide higher sensitivity and suppression of tissue harmonic signal.

Generally, multi-pulse sequences techniques rely on the different behaviour of microbubbles when exposed to consecutive pulses which vary in amplitude, phase or both. These multi-pulse techniques are illustrated in Table 1.1 and the mathematical generalisation can be found in [60]. Pulse inversion (PI) is the summation of echoes from two transmitted pulses of opposite polarities (180° out of phase) which cancels out the linear tissue signals. The inherent nature of the PI method overcomes the problematic frequency separation of harmonic imaging which often requires either a narrowband pulse or a broadband transducer

to ensure that the second harmonics do not overlap with the fundamental signals. Similar to PI, amplitude modulation (AM) and contrast-pulse sequencing (CPS) employing multiple consecutive pulses can also be used (see Table 1.1). Since low-amplitude pulses generate less harmonics from microbubbles than higher amplitude pulses, by linearly combining the echoes from the high-amplitude and low amplitude pulses the linear contribution to the scattered signal can be removed while non-linear signals remains.

While multiple transmitted pulses implies a reduced frame rate of the imaging system, the contrast and spatial resolution are improved compared to harmonic imaging. With the emergence of ultrafast ultrasound system, the temporal resolution of this imaging technique can be compensated[61], [62].

Table 1.1: Multipulse techniques used to detect non-linear microbubble signal. Adapted from [61]

Pulse	1	2	3	Linear comb.	Non-linear
Linear					—
Pulse-Inversion				—	
Amplitude Modulation				—	
Contrast Pulse Sequencing				—	

1.4 Ultrasound techniques of measuring blood flow

1.4.1 Doppler-based technique

Spectral Doppler and colour Doppler have been extensively employed for clinical measurement of blood flow. Similar to sonar or radar, the blood velocity can be extracted from the changes in either frequency or phase of the scattered echoes from moving red blood

cells. The Doppler frequency, f_d of a pulse-wave system, in its simplest form, is given as follows:

$$f_d = \frac{2|\vec{v}|\cos\theta}{c}f_0 = \frac{2v_z}{c}f_0 \quad 1-2$$

where c is the speed of sound, f_0 is the centre frequency of the transmitted ultrasound frequency, $|\vec{v}|$ is the blood velocity, θ is the beam-to-flow angle and v_z is the axial velocity component.

As pulse-wave results in a broadband response, phase-based Doppler estimators, for instance autocorrelation estimator [63] and cross-correlation estimator[64] , have been developed to refine the axial velocity measurement and are implemented on most ultrasound systems today. However, the major limitation of a conventional Doppler system is the angle dependent measurements [65], [66]. It can only determine the motion along the ultrasound beam and the axial velocity needs to be corrected with the assumption that the direction of the flow must be known prior to the estimation. This is nearly impossible when the geometry is not uniform and complex flow patterns are present, leading to significant errors in the estimated velocity[66].

In the attempt to mitigate such angle dependence, various Doppler techniques have been developed to provide velocity estimation in two or three directions as the velocity vector is three dimensional. Cross-beam vector Doppler is one of the earliest approaches developed which uses multiple beams from different angles to the estimate the velocity vector. With the known orientation of the beams, the axial (v_z) and transverse (v_x) velocity components can be calculated by solving the frequency shift equation as follow:

$$v_z (\cos \theta_1 + \cos \theta_2) + v_x (\sin \theta_1 + \sin \theta_2) = \frac{c}{f_0} f_d \quad 1-3$$

where θ_1 and θ_2 are the beam-to-flow angle of the two independent cross-beams. Variations of the cross-beam method can be found in [67], [68]. Early formulations of this method involved two or multiple transducers that alternate as transmitter and receivers, aligned in a trigonometric scheme. With the progressive array transducer technology, electronic splitting of the array into sub-apertures become possible and this approach is exploited to derive velocity vectors using single transducer arrays[69]–[72]. However, common to all these methods is that the estimation accuracy is dependent on the angle between the two beams. The error in either one of the estimated frequency may cause significant variance to the estimation. To overcome such problems, reformulation of the multi-beam approach in an over-determined system of equations which can be solved in a least square computation method has been proposed recently to minimise the errors[73].

Another Doppler technique to find multi-directional velocity vector known as Transverse Oscillation (TO) was introduced by Anderson, Jensen and Munk[74]–[76]. Similar to the principle of estimating the axial velocity from the ultrasound oscillation, the basic idea of this method is to generate a controlled spatial oscillation lateral to the emitted ultrasound beam, creating a double oscillating field for velocity estimation. As the Fourier relationship between the apodization and beam pattern exists, sinusoidal oscillation in the lateral direction can be generated by manipulating the receive apodization. Many apodization schemes have been investigated to optimise the transverse oscillation point spread function (PSF), including spatial quadrature signal generation[75], Hilbert transform apodization waveform[74], dynamic apodization[77] and plane wave TO imaging[78]. To estimate the two velocity components, a phase-based estimator, which is essentially an extension of the autocorrelation estimator has been derived [79]. However, as the estimation of the lateral velocity component depends on the resulting oscillation field, the lateral wavelength which is predicted from the receive apodization may bias the estimation and affects the accuracy.

Although the phase shift estimator has been widely implemented on pulse-Doppler system, a major limitation of using a phase shift estimator is that aliasing can occur when estimating flow with high velocity. To circumvent the aliasing problem, a time shift estimator has been implemented to estimate axial velocity[80]–[82], by cross-correlating successive A-line signals in time-domain. The Directional Beamforming technique is one of the Doppler methods which uses time shift estimator to determine the velocity vector in any direction[83]. The angle of the flow is initially estimated through prior knowledge [83], [84] or from normalised correlation from multiple directional signals[85]–[87]. With the known directional signal along the flow direction, the velocity can be estimated by means of time domain cross-correlation. This approach is shown to provide very accurate flow measurements, however it is very computationally intensive.

Temporal resolution is critical to estimate the blood flow velocity. In conventional Doppler system, although over each pulse-echo line the pulse repetition frequency is high and fast flow along the axial direction can be tracked, the line sweeping process to form the Doppler image significantly limits the effectiveness of the existing Doppler estimation technique. Trade-off between the frame rate of the Doppler imaging and the size of the field-of-view is often required. In addition, short ensemble length may also hinder the ability to separate blood signal from tissue signal. This is mainly because the designing of the FIR or IIR filter to operate on very short vectors is a great challenge. With the emerging high frame rate system which enable frame rate up to two orders of magnitude over the conventional line-by-line imaging, the benefits of ultrafast Doppler [51] and plane wave vector Doppler[78], [88], [89] has been demonstrated.

1.4.2 Non-Doppler techniques

Along with the new developments in Doppler techniques, the ultrasound speckle tracking method based on ultrasound B-mode images has been applied in [45], [90], [91] to provide

angle independent flow measurement. With sufficient signal scattered by the red blood cells (RBCs), speckle images are tracked by means of image tracking techniques such as block matching and optical flow[92]. While various techniques exist, block matching methods such as cross-correlation or sum-absolute-difference are commonly used to extract large displacements in blood flow imaging. However, as the signal generated from RBCs results in low SNR and the speckles are heterogeneous, temporal averaging is often needed to enhance the signals from RBCs and reject the high-amplitude signal from surrounding tissue[93]. To achieve this, a high temporal resolution imaging system is required to avoid speckle decorrelation and generate enough frames for temporal averaging [89]. This therefore limits the application of speckle tracking in conventional ultrasound imaging.

To mitigate the effects of low SNR from RBCs, another non-Doppler technique known as echo Particle Image Velocimetry (echo-PIV) or Ultrasound Imaging Velocimetry (UIV) is proposed. It is a technique which originated from Optical PIV [94], [95]. Optical-PIV relies on the visualisation of flow by means of small tracer particles illuminated by a laser sheet to track the movement of the particles recorded in consecutive images; UIV, on the other hand, estimate the flow by tracking the flow speckle pattern generated in the ultrasound images. Initial study using medical ultrasound system was reported by [96] to investigate the flow field up to 6 cm/s using sediment-laden flow images containing kaolin particles as a flow tracer. However, it wasn't until the advent of microbubble contrast agents that UIV became more extensively studied [97]–[99]. Promising results under *in-vitro* and *in-vivo* conditions have been demonstrated to provide angle independent vector flow imaging[99]–[101], however the accuracy of UIV to provide quantitative measurement is still limited when a conventional ultrasound imaging system with low temporal resolution is used. With the emerging high frame ultrasound system, it is believed that the frame-rate limitation from conventional ultrasound imaging can be overcome.

1.5 Other imaging modalities

In addition to ultrasound, imaging modalities such as Magnetic Resonance Imaging (MRI) and Computed Tomography (CT) are routinely used in clinic to assess blood flow. Local injection of contrast agents are typically required to track the blood flow over space and time. For instance, iodine or barium compounds are used in contrast-enhanced CT whereas gadolinium-based compounds are commonly used for visualising flow in-vivo. While these techniques can provide high anatomical and geometric resolution, they still have limitations in terms of rapid and contemporaneous assessment in three-dimensional geometry and flow. MRI imaging suffered from long acquisition time and high cost whereas CT involves the use of ionising radiation. The procedure can be highly invasive and the injection of contrast medium can be difficult to control. Although some MRI techniques such as arterial spin labelling and phase contrast can track flow without contrast injection, they suffer from poor signal-to-noise ratio and currently are used predominantly to assess tissue perfusion.

1.6 Ultrasound Imaging Velocimetry (UIV)

1.6.1 Background and Principle of UIV

The UIV technique is one of the techniques that solved the angle-dependence of classical Doppler method. Originating from Optical PIV, UIV overcomes the major limitation of optical-PIV which required a transparent medium condition. Microbubbles, the flow tracers, are tracked in contrast imaging to calculate the velocity of the intravascular flow. The principle of UIV is shown in Figure 1.5. Sequential ultrasound B-mode or contrast images, consist of either the individual flow tracer or speckle patterns, are acquired using a medical ultrasound system. To obtain the local velocity vectors, two subsequent images are divided into several smaller interrogation windows (sub-images) and a 2D cross-correlation function is efficiently performed for individual interrogation windows using an FFT-based cross-correlation function defined as

$$R^k(x, y) = \mathcal{F}^{-1}\{\mathcal{F}(w_1^k) \mathcal{F}^*(w_2^k)\} \quad 1-4$$

where $w_1(i, j)$ and $w_2(i + x, j + y)$ denote the image intensity distributions of the sub-image pairs, x and y represent the pixel displacement between the two images, \mathcal{F} and \mathcal{F}^{-1} denote the forward and inverse Fourier transform, and $*$ denotes the complex conjugate. From the correlation plane, the displacement (in pixels) between two windows is given by the peak location.

$$(u^k, v^k) = \arg \max (R_k(x, y)) \quad 1-5$$

To achieve sub-pixel accuracy, various methods of estimating the location of the correlation peak have been utilised [102]. A simple yet robust method is to fit the correlation peak to a three-point estimator listed in Table 1.2. Other estimators such as 2D-Gaussian estimator [103], sinc or Whittaker interpolator[104], [105] are also worth mentioning as they are capable of providing a higher accuracy estimation. However, along with the accuracy improvement, the computational load to perform 2D and sinc interpolation increases significantly; therefore a three-point estimator is preferable as it is sufficient to perform one-dimensional fits in practice. Among all estimators, the Gaussian peak fit is the most common sub-pixel estimator used both in Optical PIV and UIV as the particle or speckle pattern generated are approximated well by a Gaussian intensity distribution.

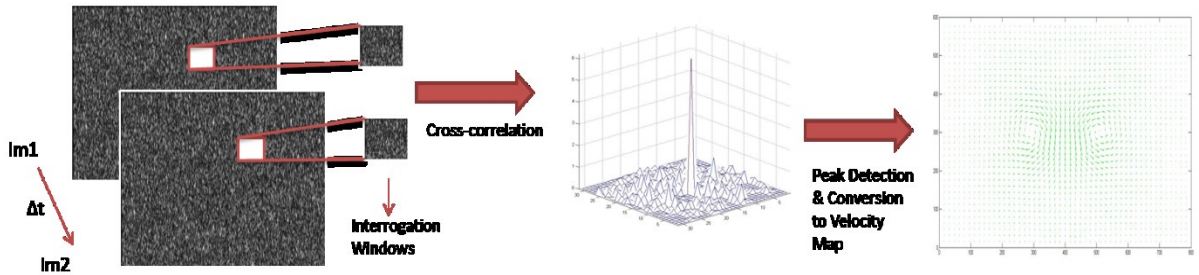


Figure 1.5: Basic principle of UIV

Table 1.2: Three-point estimator for determining the subpixel displacement from the correlation peak[102].

Fitting function	Estimators
Peak centroid $f(x) = \frac{\text{first order moment}}{\text{zero order moment}}$	$x_0 = \frac{(i-1)R_{(i-1,j)} + i R_{(i,j)} + (i+1)R_{(i+1,j)}}{R_{(i-1,j)} + R_{(i,j)} + R_{(i+1,j)}}$ $y_0 = \frac{(j-1)R_{(i,j-1)} + j R_{(i,j)} + (j+1)R_{(i,j+1)}}{R_{(i,j-1)} + R_{(i,j)} + R_{(i,j+1)}}$
Parabolic fit $f(x) = Ax^2 + Bx + c$	$x_0 = i + \frac{R_{(i-1,j)} - R_{(i+1,j)}}{2R_{(i-1,j)} - 4 R_{(i,j)} + 2R_{(i+1,j)}}$ $y_0 = j + \frac{R_{(i,j-1)} - R_{(i,j+1)}}{2R_{(i,j-1)} - 4 R_{(i,j)} + 2R_{(i,j+1)}}$
Gaussian peak fit $f(x) = C \exp \left[\frac{-(x_0 - x)^2}{k} \right]$	$x_0 = \frac{\ln R_{(i-1,j)} - \ln R_{(i+1,j)}}{2 \ln R_{(i-1,j)} - 4 \ln R_{(i,j)} + 2 \ln R_{(i+1,j)}}$ $y_0 = \frac{\ln R_{(i,j-1)} - \ln R_{(i,j+1)}}{2 \ln R_{(i,j-1)} - 4 \ln R_{(i,j)} + 2 \ln R_{(i,j+1)}}$

While sub-pixel accuracy can be achieved using peak fitting methods, conventional PIV only considers the linear translation and no rotation and deformation can be recovered by this first order estimation. To tackle this problem, several advanced techniques developed in Optical-PIV, have been adapted to ultrasound imaging. Multi-pass interrogation with discrete offset is one of the earliest techniques to enhance the accuracy of PIV[106], [107]. The principle of this technique is similar to the conventional method; however, a window offset is applied to each interrogation window during the iteration process until the offset vectors converge to a single pixel. A hierarchical approach in which the sampling grid is continually refined can

also be used to further improve the accuracy of the multi-pass techniques [108]. Due to its simple implementation and accurate measurement, this technique has been adapted to UIV to investigate intravascular flow both *in-vitro* and *in-vivo* [98], [101], [109].

Another advanced Optical-PIV technique which has been widely used is the windows deformation iterative multi-grid approach (WIDIM) [108]. This technique has also been demonstrated in ultrasound imaging to improve high gradient flow estimation [110]. By deforming the image according to the velocity field, image deformation is conceived for the compensation of the in-plane velocity gradient and peak broadening effect. The iterative multi-grid approach, on the other hand, is incorporated to further refine the measurement to higher accuracy and spatial resolution as shown in Figure 1.6. The displacement field is first acquired by means of the undeformed coarse-grid interrogation and then progressively estimated from a smaller deformed grid. In this context, predictors for the displacement field are generated from the estimated flow field to interpolate the image. Several common interpolation approaches such as bilinear interpolation, sinc interpolation, cubic interpolation, and spline interpolation, are commonly used to deform the image. Thus, cross-correlation is done on a finer grid and a higher spatial resolution is obtained. Despite using smaller interrogation windows, the probability to detect the real peak in the correlation plane remains high when using the image deformation approach.

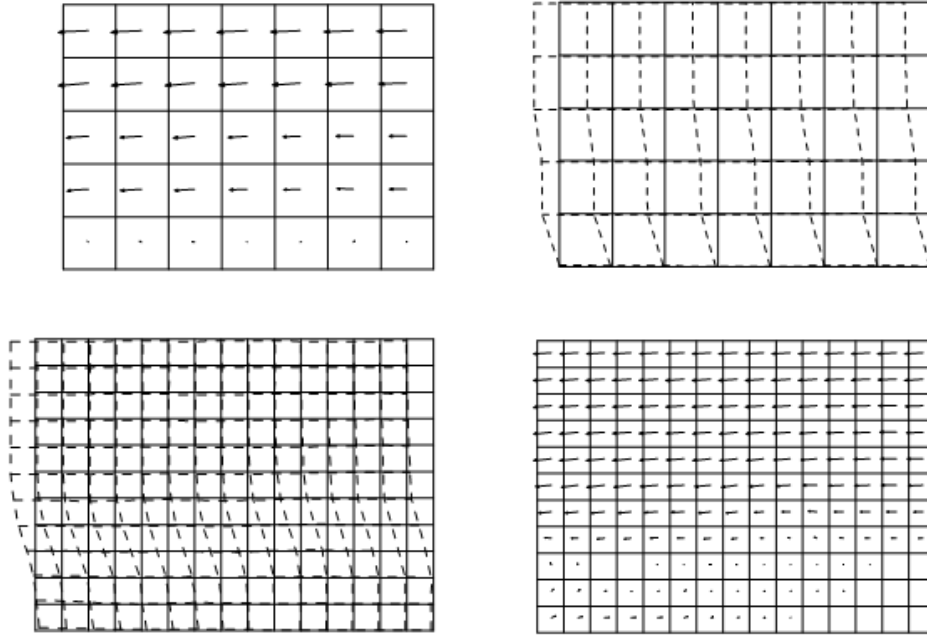


Figure 1.6: Multi-grid iterative window deformation technique in which interrogations are progressively deformed according to the velocity field measured from the previous iteration. [102]

It is generally assumed that the measured displacement field is uniform and that a certain coherence can be expected. As the flow displacement is directly estimated from the cross-correlation function which is a statistical measure, a spurious vector may emerge if the displacement-correlation peak does not exceed that of the random correlation peak. The peak detectability may be impeded by the loss of correlation due to fast in-plane and out-of-plane motion, local variations of the velocity field, and poor image quality. Statistically a spurious vector elimination algorithm such as normalised median filter[111] is normally applied as a post-processing step to replace outliers. A more sophisticated algorithm known as ensemble correlation can also be incorporated in the existing techniques to enhance tracking accuracy. The principle of ensemble correlation is illustrated in Figure 1.7 [112]. By averaging a series of instantaneous correlation planes acquired at each measurement point, the SNR and peak detectability are enhanced. This therefore drastically improves the measurement quality and increases the spatial resolution by allowing a smaller interrogation area to be employed in the

analysis. The effectiveness of ensemble correlation has been demonstrated both in Optical PIV [113] and UIV[114].

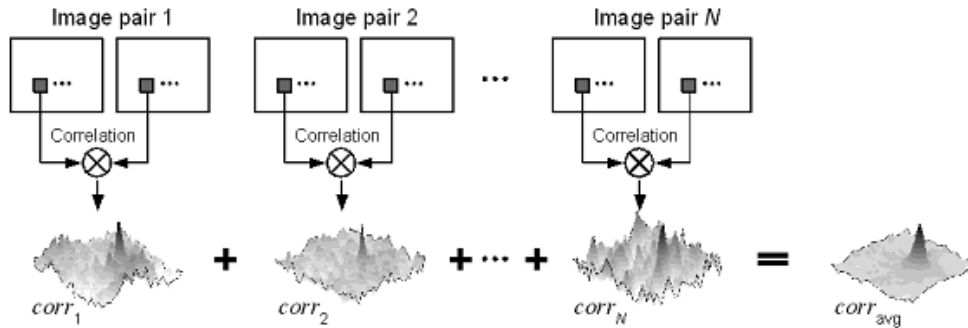


Figure 1.7: Ensemble correlation technique in which multiple instantaneous correlation planes are averaged to enhance the peak detectability and signal to noise ratio[112].

1.6.2 Current limitations of UIV

Studies have shown the potential of UIV to non-invasively measure the hemodynamics. Initial validation of the UIV system against other imaging modalities has been demonstrated. For example, [99] reported the capability of UIV to accurately measure the flow velocity in a carotid bifurcation model when validated with PC-MRI derived measurement,[101] and [115] demonstrated a highly correlated 2D velocity vector flow field of a vortex ring between UIV and optical-PIV. *In-vivo* studies were also demonstrated in carotid arteries [99], [100], small animal arteries and veins[116], and the left ventricle [115], [117], [118].

Although a number of studies have been reported, the application of the UIV is restricted due to the frame rate limitation of clinical ultrasound system [99], [101], [119]. Low temporal resolution results in large estimation errors as the cross-correlation is unable to track the fast flow within the limited field of view. Therefore, trade-off between field of view and temporal resolution is often required in UIV analysis to increase the measured velocity range [98], [120]. Besides, the beam-sweeping process of a conventional ultrasound system and the sweeping direction have been reported to introduce significant errors to flow velocity

estimation [100], [120]. Velocity is overestimated when the beam sweeps in the same direction as the flow direction, whereas underestimation occurs when the sweeping direction is opposite to the flow direction. A correction method for steady flow has been proposed by [120], however this cannot be applied to a physiological flow which is pulsatile and complex. To address all the problems aforementioned, a fast UIV system which could provide highly accurate measurement is needed.

1.7 Purpose and Thesis Structure

As underlined in the previous section, the UIV technique has shown its merit to provide accurate, angle independent flow velocity vectors. However, the application of this technique has been hindered due to the limitation of the conventional ultrasound systems. With the recent developments in high frame rate ultrasound imaging technology, this offers new possibilities especially in quantitative flow imaging.

The aim of this thesis is to investigate and develop flow visualisation and quantification techniques using high frame rate ultrasound imaging and microbubble contrast agents. In this context, the work presented is divided into seven chapters where the first is the introduction and literature review. The following chapters are as follow:

Chapter 2: Initial development of flow velocity mapping using plane wave UIV

This chapter presents the development of a quantitative flow velocity mapping system, which integrates plane wave ultrasound imaging, ultrasound imaging velocimetry, contrast agent and pulse inversion contrast imaging. Initial evaluations were conducted *in vitro* on flow phantoms and *in-vivo* in the rabbit aorta.

Chapter 3: Toward a reliable and accurate flow velocity measurement using plane wave UIV

This chapter presents the full evaluation of plane wave UIV to provide reliable and accurate velocity measurements. A modified UIV technique was introduced to provide a more robust measurement when plane wave images are not coherently summed during the image formation. Ultrasound flow simulation was conducted to fully evaluate the performance of the system and *in-vitro* study on two anthropomorphic phantoms was demonstrated.

Chapter 4: Accuracy of Plane wave UIV for Wall Shear Stress measurement

This chapter presents the extension of plane wave UIV system to provide spatio-temporal wall shear stress (WSS) measurement in addition to quantitative velocity flow field measurement. Optimization and evaluation of the system to provide accurate WSS were performed using the ultrasound flow simulation described in Chapter 4. *In-vitro* studies were also demonstrated.

Chapter 5: Microbubble void imaging

This chapter summarises a novel method utilising the high frame rate ultrasound system and controlled microbubbles destruction for visualising flow and quantifying mixing in large vessels. An *in-vitro* experiment was performed on three different vascular geometries, and the results were compared with numerical computational fluid dynamics (CFD) solutions.

Chapter 6: GPU-accelerated UIV system

This chapter presents a development of a GPU-accelerated UIV system. This includes the GPU acceleration of the plane wave ultrasound image beamforming and the UIV algorithm using Compute Unified Device Architecture (CUDA). Initial performance of the GPU implementation was compared to a normal CPU system implementation.

Chapter 7: Conclusion and future work

This chapter summarises the contributions of this thesis and future work.

1.8 Scientific contributions

The scientific contribution of this thesis is mainly presented in 3 journal papers and 5 conference abstracts. The author has also contributed to an additional journal paper listed at the end.

Journal Paper

Leow, C. H., Bazigou, E., Eckersley, R. J., Alfred, C. H., Weinberg, P. D., & Tang, M. X. (2015). Flow Velocity Mapping Using Contrast Enhanced High-Frame-Rate Plane Wave Ultrasound and Image Tracking: Methods and Initial in Vitro and in Vivo Evaluation. *Ultrasound in Medicine & Biology*, 41(11),

Leow, C. H., Iori, F., Corbett, R., Duncan, N., Caro, C., Vincent, P., & Tang, M. X. (2015). Microbubble Void Imaging: A Non-invasive Technique for Flow Visualisation and Quantification of Mixing in Large Vessels Using Plane Wave Ultrasound and Controlled Microbubble Contrast Agent Destruction. *Ultrasound in Medicine & Biology*, 41(11), 2926-2937.

Leow, Tang, M. X. Accurate Spatio-temporal Flow Velocity Mapping and Wall Shear Stress Measurement using High-Frame Rate Ultrasound Imaging Velocimetry. *Ultrasound in Medicine & Biology* (under review).

Conference proceedings/abstracts

Leow, C. H., Tang, M. X. High Accuracy Flow Velocity Mapping and Wall Shear Rate Measurement Using High Frame-Rate Ultrasound Imaging Velocimetry. 22nd Congress of European Society of Biomechanics, 10th July – 13th July 2016.

Leow, C. H., Iori, F., Corbett, R., Duncan, N., Caro, C., Vincent, P., & Tang, M. X. Microbubble void imaging – a novel technique for the qualitative and quantitative

assessment of intravascular mixing using contrast enhanced ultrasound. Summer Biomechanics, Bioengineering and Biotransport Conference, Utah, USA, 29th June – 2nd July 2015.

Leow, C. H., Bazigou, E., Eckersley, R. J., Alfred, C. H., Weinberg, P. D., & Tang, M. X.. Ultrafast Ultrasound Imaging and Microbubbles for Blood Flow Visualisation and Quantification. 2015 Joint BHF Centres of Research Excellence Imaging Symposium, London, UK, 18th June 2015.

Leow, C. H., Eckersley, R. J., Alfred, C. H., & Tang, M. X. Plane Wave Ultrasound Imaging and Tracking of Microbubbles for Flow Visualisation, Quantification and Initial Evaluation on a Carotid Bifurcation Phantom. 19th European Symposium on Ultrasound Contrast Imaging, Rotterdam, Netherland, 22-23 January 2015.

Leow, C. H., E., Eckersley, Tang, M. X. Plane Wave Ultrasound Imaging Velocimetry. IEEE International Ultrasonics Symposium, Chicago, USA, 3-6 September 2014.

Co-authored journal paper

Ja'afar, F., Leow, C. H., Garbin, V., Sennoga, C. A., Tang, M. X., & Seddon, J. M. (2015). Surface Charge Measurement of SonoVue, Definity and Optison: A Comparison of Laser Doppler Electrophoresis and Micro-Electrophoresis. *Ultrasound in Medicine & Biology*, 41(11), 2990-3000.

Chapter 2 - Initial development of flow velocity mapping using plane wave UIV

In this chapter, we present the development of an ultrasound imaging velocimetry approach capable of visualising and quantifying dynamic flow, by combining high frame-rate plane wave ultrasound imaging, microbubble contrast agents, pulse inversion contrast imaging and speckle tracking algorithms. The system has been initially evaluated *in vitro* on both straight and carotid-mimicking vessels with steady and pulsatile flows, and *in vivo* in the rabbit aorta. Colour and spectral Doppler measurements were also made. Initial flow mapping results were compared with theoretical prediction and reference Doppler measurements and demonstrate the potential of the new system as a highly sensitive, accurate, angle-independent and full field-of-view velocity mapping tool capable of tracking and quantifying fast and dynamic flows. This work was in collaboration with Dr. Alfred Yu from University of Hong Kong, who provided the carotid bifurcation phantoms for validation, and Dr Eleni Bazigou who provided assistant to acquire *in-vivo* rabbit data. The results shown in this chapter has been included in [121]

2.1 Introduction

Techniques capable of quantitative mapping blood flow velocity *in vivo* are highly desirable in studying a wide range of cardiovascular diseases. As mentioned in the previous chapter, flow velocity and its derivatives such as vorticity and wall shear stress are essential in the study of the pathogenesis of atherosclerosis [4], [122]. However, existing non-invasive techniques for flow velocity mapping have various limitations. Phase-contrast magnetic resonance imaging (MRI) and phase velocity mapping are valuable clinical modalities which offer the potential to obtain volumetric velocity vectors *in vivo*. However, they suffer from low temporal resolution and lack of accessibility [123], [124]. Doppler ultrasound is

extensively used for visualisation and measurement of blood flow clinically [65], [125], [126]; the blood velocity is calculated from the changes in either frequency or phase of the ultrasound reflected from moving red blood cells. However, in most existing ultrasound scanners images are formed line by line resulting in an inherent trade-off between field of view and Doppler sensitivity or frequency resolution. Additionally, due to the weak scattering from blood cells Doppler also has a trade-off between spatial/temporal resolution and signal-to-noise ratio (SNR). The performance can also be affected by various artefacts due to aliasing and beam-flow angle variations [127]. Some new Doppler techniques have been developed including crossed-beam vector Doppler [69], [70], [72], [128], vector flow mapping [129], [130], directional cross-correlation method [83], [87], transverse oscillation method [131], [132] and pulse inversion Doppler [133], [134]. Non-Doppler ultrasound techniques including ultrasound Speckle Tracking [90] and Ultrasound Imaging Velocimetry (UIV) [99], [114], [135] have also been investigated. The main difference between Speckle Tracking and UIV is that Speckle Tracking relies on the speckle images generated from the red blood cells to estimate the flow field whereas UIV tracks the microbubble contrast agents injected intravenously. Swillens and colleagues compared Vector Doppler and Speckle Tracking for quantifying blood flow using line-by-line scanning ultrasound and concluded that high frame rate plane wave ultrasound would address the current limitations of both approaches [136].

Recent developments in high frame-rate ultrasound imaging technology offer new possibilities for flow estimation. By transmitting unfocussed ultrasound pulses and using parallel receive beamforming instead of line by line scanning, substantially higher acquisition rates (up to twenty thousand frames per second) can be achieved [50], [137]. Notably in flow imaging, fast imaging techniques show promising results especially in ultrafast Doppler [51], [86] and vector Doppler [73], [88], [138], [139]. The use of high frame-rate ultrasound to

track microbubbles in the blood stream between imaging frames (high frame-rate UIV) has not been reported.

In this study, we aim to develop a highly sensitive, accurate, angle-independent and full field-of-view flow velocity mapping tool capable of tracking fast and dynamic flows, by combining high frame-rate plane wave ultrasound imaging, ultrasound imaging velocimetry, microbubble contrast agents and pulse inversion contrast imaging. The system has been initially evaluated in vitro on flow phantoms with highly dynamic and pulsatile flows and in vivo in the rabbit aorta.

2.2 Methods and Material

A high frame rate ultrasound imaging velocimetry (UIV) system has been developed based on tracking the speckle patterns of microbubble contrast agents in contrast enhanced ultrasound image sequences acquired from a high frame-rate plane wave imaging system.

2.2.1 Microbubbles Contrast Agents

Decafluorobutane microbubbles were prepared as described by [140]. 1,2-dipalmitoyl-sn-glycero 3-phosphatidylcholine(DPPC), 1,2-dipalmitoyl-sn-glycero-3-phosphatidylethanolamine-polyethyleneglycol-2000(DPPE-PEG-2000), and 1,2-dipalmitoyl-3-trimethylammonium propanoate(chloride salt; 16:0 TAP) were dissolved in a molar ratio of 65:5:30 and a total lipid concentration of 0.75mg/mL, 1.5mg/mL, and 3mg/mL, resulting in a solution comprised of propylene glycol, 15% glycol, 5% glycerol and 80% normal saline. Microbubbles were generated via agitation of a 2mL sealed vial containing 1.5mL of the resulting solution, using a shaker for 60 seconds.

The microbubble solution generated was sized and counted according to [141] and was found to have a concentration of about 5×10^9 microbubbles/mL with an average size of 1 micron. In this study, microbubbles were diluted in gas equilibrated water [142] to a concentration of

2×10^5 microbubbles/mL, a clinically relevant concentration as used in previous studies[143], [144].

2.2.2 Fast ultrasound imaging system and Pulse Inversion

A L12-3v linear array probe connected to a Verasonics Vantage 128 research platform (Verasonic Inc, Redmon,WA,United State) was used to acquire high frame-rate ultrasound images as shown in Figure 2.1. Since the platform consists of 128 transmit and receive channels, 128 elements located at the centre of the 192 elements probe were used in each pulse echo sequence, resulting in a 25mm lateral field of view. A plane wave Pulse Inversion imaging scheme was used to acquire contrast images. Twelve plane waves with six angles tilted between -18 and +18 degrees (7.2 degree step) were transmitted with a pulse repetition frequency of 15.5kHz to form an image after coherent compounding [50], achieving a frame rate of 1000 Hz for an imaging depth of 25 mm. For each angle, a 3 MHz 1 cycle plane wave pulse followed by its phase inverted counterpart (Pulse Inversion) was transmitted before moving to another angle. The radio frequency (RF) echoes for each transmission were recorded in the local memory. The RF data collected were then transferred back to a computer through a high-speed PCI-Express, and software beamformed into images for further analysis using Matlab.

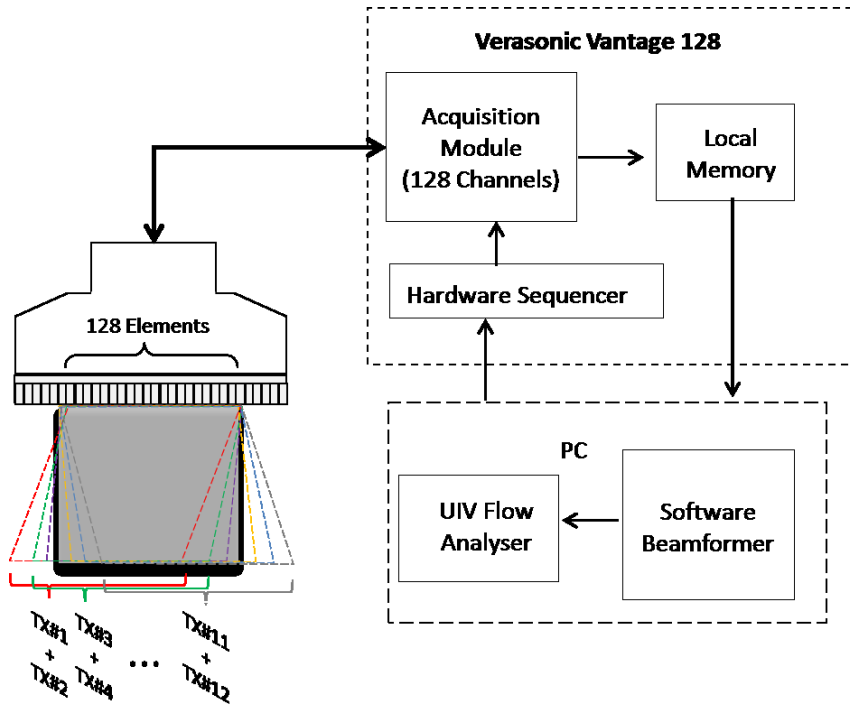


Figure 2.1: Overview of the system hardware and data acquisition scheme involve in plane wave UIV.

2.2.3 UIV Analysis

A UIV analysis algorithm was implemented to provide quantitative flow velocity mapping. This well-established method is a modification of the conventional PIV algorithm [145], and incorporates several improvements including windows deformations iterative multigrid (WIDIM) [108], [110] and ensemble correlation technique [112], [113] which have been described in Chapter 2. A 3-point Gaussian peak fitting and a simple 3x3 spatial medium filter were implemented for sub-pixel displacement and spurious vector elimination. The schematic work flow of the UIV algorithm is illustrated in Figure 2.2.

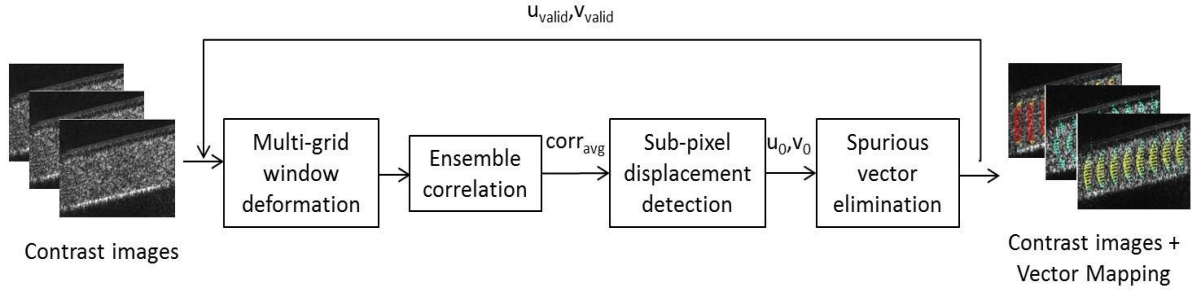


Figure 2.2: The basic workflow of UIV algorithm

2.2.4 Straight vessel flow phantom

To evaluate the system, *in-vitro* experiments on a straight vessel phantom were performed, and measurements made with plane wave UIV were compared with both analytically derived values and ultrasound Doppler under various flow conditions. The flow system was constructed as shown in Figure 2.3. A 6mm latex tube (098 XA/XB, Pipeline Industries, Denver, CO, USA) was placed in a water tank filled with gas equilibrated water. Microbubble solution was uniformly mixed in a reservoir contain of gas equilibrium water and circulated in the latex tube. The L12-3v transducer mounted on a Verasonics Platform was placed above the tube to acquire the contrast images while an 11L4 transducer mounted on a Toshiba ultrasound system (AplioXG, Toshiba Medical Systems Corp, Otawara, Japan) was placed 5cm away from the L12-3v transducer to acquire Doppler measurements. With 8MHz long cycle pulses transmitted, the pulse repetition frequency and the angle were manually adjusted to avoid aliasing and compensate the angle dependent measurement. Both transducers were tilted with an angle of 8 degree to the flow direction but were operated alternately to avoid interference. An acoustic absorber was placed at the bottom of the tank to prevent reflection from the tank walls.

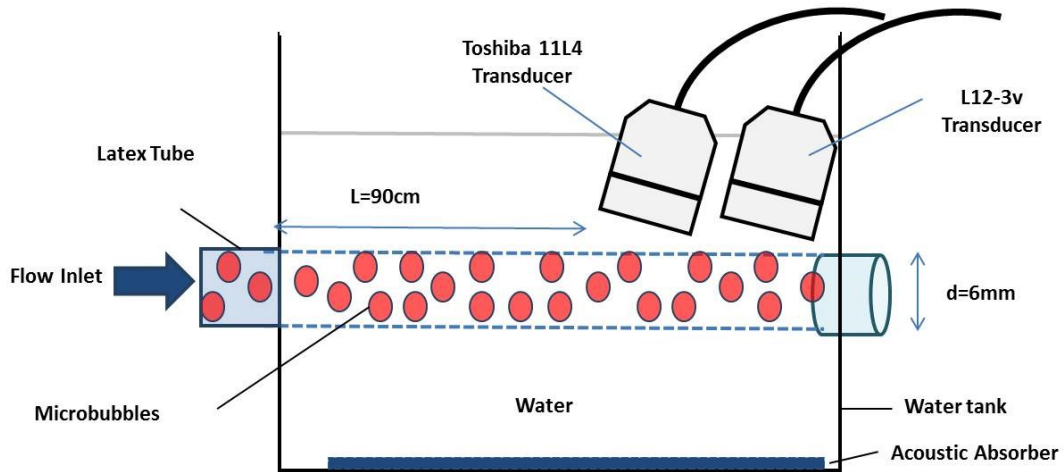


Figure 2.3: Schematic of the straight tube flow system.

2.2.4.1 Steady Laminar Flow

A gravity flow setup was employed to create a steady laminar flow through the latex tube. The working fluid flow through the tube was a diluted microbubble solution which had been mixed uniformly by manual stirring at the source tank before the experiment began. The volume flow rate, Q was recorded using a bucket and stopwatch. Both transducers were placed more than 70cm away from the inlet in order to measure a region where a fully developed laminar flow with parabolic velocity profile could be observed. The maximum velocity is calculated as defined in Eq 2-1:

$$V_{max} = \frac{8Q}{\pi d^2} \quad 2-1$$

where Q is the volume flow rate and d is the diameter of the tube. The inlet length L was then calculated with the formula taken from [146]:

$$L = 0.04d Re \quad 2-2$$

$$Re = \frac{vd\rho}{\mu} \quad 2-3$$

where, Re is the Reynold Number, V is the average velocity, ρ is the fluid density and μ is the dynamic viscosity.

Measurements were obtained with 3 flow rates, as shown in Table 2.1. A series of contrast images were acquired at a 1000 Hz frame rate using the Verasonics platform and analysed using the UIV algorithm. The results were then compared to the analytical velocity profile calculated based on the measured average flow rate using a bucket and stopwatch. Also, colour Doppler and spectral Doppler velocities located at the centre of the tube were recorded using the Toshiba ultrasound system.

Table 2.1: Flow parameters of 3 different laminar flows

Flow Condition	Q (ml/min)	V_{\max} (cm/s)	Re	L (cm)
Slow	85	10	300	7.2
Medium	325	38	1200	28.8
Fast	500	59	1768	42.5

2.2.4.2 Pulsatile Flow

Pulsatile flow was investigated with the same experimental setup. Pulsatile flow running at 80 strokes per minute, delivering 4ml/stroke of solution, was driven by a mechanical pulsatile pump (Harvard Apparatus 1405 pulsatile blood pump, Harvard Apparatus Ltd, Kent UK), The pump contain a positive piston actuator and ball check valves to simulate the ventricular action of the heart. Plane wave contrast images were obtained and post-processed using the UIV algorithm, while the tri-mode Doppler measurements were obtained using the Toshiba scanner.

2.2.5 *In-vitro* Carotid Bifurcation Model

An anatomically realistic carotid bifurcation model as described in [147] was used to further evaluate the system. In brief, the compliant vessel models were drafted using computer aided design software and fabricated using stereolithography. The thin wall vessel was constructed with the use of a compliant photopolymer (FullCure 930; Object Geometry), to mimic the physical and acoustic properties of human arteries. It has an average elastic modulus of 391 kPa, average speed of sound of 1801 m/s and attenuation coefficient of $1.58 \text{ dB mm}^{-1} \cdot \text{MHz}^{-1}$.

The phantom vessel contains three branches mimicking in turn the common carotid artery (CCA), the internal carotid artery (ICA) and the external carotid artery (ECA). The experimental setup and the normal carotid bifurcation model are shown in Figure 2.4. Instead of using water, microbubbles were diluted in a blood mimicking fluid (BMF), which comprised 90% pure water and 10% glycerol, to demonstrate a physiological relevant condition [148]. The inlet of the setup was connected to a pulsatile pump (Harvard Apparatus 1405 pulsatile blood pump, Harvard Apparatus Ltd, Kent UK), delivering 3ml of the diluted microbubble solution per stroke and running at 80 strokes per minute.

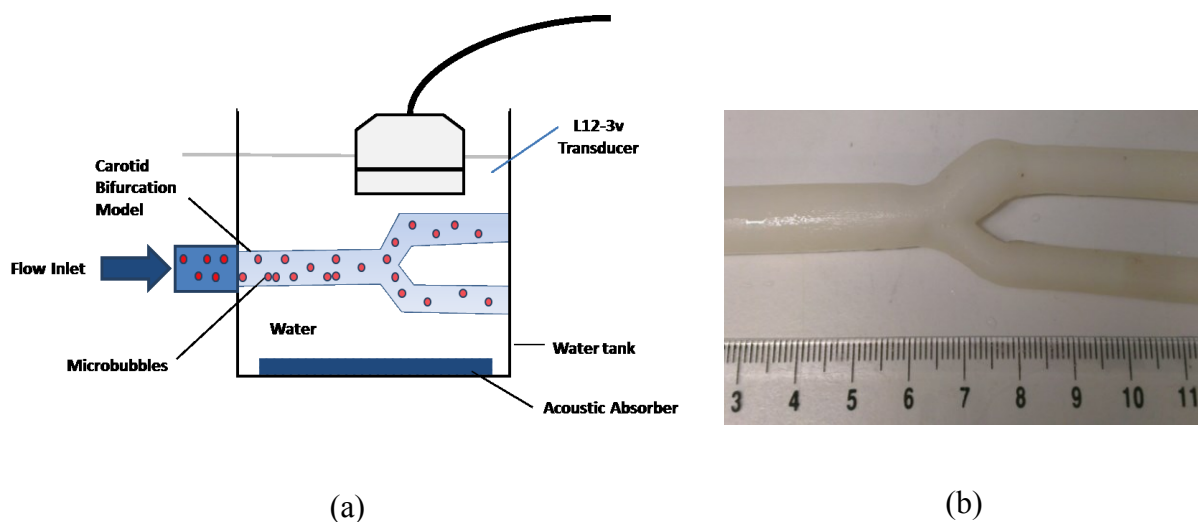


Figure 2.4: (a) Schematic of the carotid bifurcation experimental setup. (b) Carotid bifurcation tube without stenosis.

2.2.6 *In vivo* Rabbit Experiment

Experiments were conducted to measure blood flow velocities in the abdominal aorta of the rabbit *in vivo*, as shown in Figure 2.5. All procedures complied with the Animals (Scientific Procedures) Act 1986 and were approved by the Local Ethical Review Process Committee of Imperial College London. A male New Zealand White rabbit (1.5 years old) was anaesthetised with medetomidine (0.25ml/kg) and ketamine (0.15ml/kg) and its body temperature maintained at 37⁰C by a warming plate. With the fur around the scanning site removed, images of the rabbit's abdominal aorta were acquired non-invasively using the Verasonics system and an L12-3v probe while a bolus of 0.1ml Sonovue™ microbubbles was injected via the marginal ear vein. The ultrasound imaging settings were the same as in the *in vitro* studies.

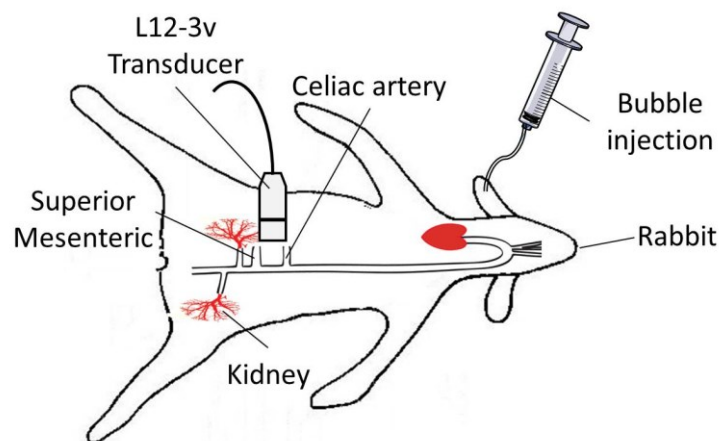


Figure 2.5: *In vivo* experimental set up. Contrast agents were injected through the anaesthetised rabbit's ear and the rabbit abdominal aorta was scanned using an L12-3 probe.

2.3 Results

2.3.1 Straight vessel phantom

2.3.1.1 Steady Laminar Flow

Figure 2.6 shows the comparison between flow measurements acquired using Doppler ultrasound and plane wave UIV. Figure 2.6(a)-(f) show the Doppler measurements while

Figure 2.6 (g)-(l) show the plane wave UIV measurement. The Doppler measurements were acquired in triplex-mode, where B-mode, colour and spectral Doppler were obtained at the same time. In each measurement, the colour Doppler images show the flow field across the tube while the centreline peak velocity was obtained using spectral Doppler with a 1mm x 1mm range gate as shown in Figure 2.6 (a)-(c). In Figure 2.6 (d)-(f), a red line is drawn in each spectral measurement to indicate the maximum velocity in the spectral Doppler measurements. The peak velocities were compared to the analytical solution derived from the measured flow rate obtained using a bucket and stopwatch as illustrated in Table 2.2. The Doppler measurements are slightly higher than thereference peak velocities. . The discrepancy is probably due to the geometrical spectral broadening[149], [150] and the broadening of the Doppler spectrum by microbubbles [151].

Table 2.2: Comparison of the peak velocity measurement estimated from spectral doppler and UIV with the analytical velocities

Flow Condition	Peak Velocity (cm/s)		
	Analytical solution	Spectral Doppler	UIV
Slow	10.0	12.5	9.9
Medium	38.0	46.0	36.5
Fast	59.0	68.0	58.6

Figure 2.6 (g)-(l) were obtained using plane wave UIV with a 1 kHz acquisition rate. Fully developed laminar flows of parabolic profile under the slow and fast flow conditions in the 6mm tubes can be clearly visualised. The parabolic flow vectors are consistent across the tube under all flow conditions. To provide a quantitative measurement, the velocity fields were also represented in a colour encoded vector plot overlaid on the contrast enhanced images. In all cases shown in Figure 2.6 (j)-(l), plane wave UIV measurements were found to

match the analytical flow profile with good accuracy: root mean square errors of 0.66cm/s (6.6%), 3.64cm/s (9.6%) and 3.63cm/s (6.2%) were obtained in slow, medium and fast flow.

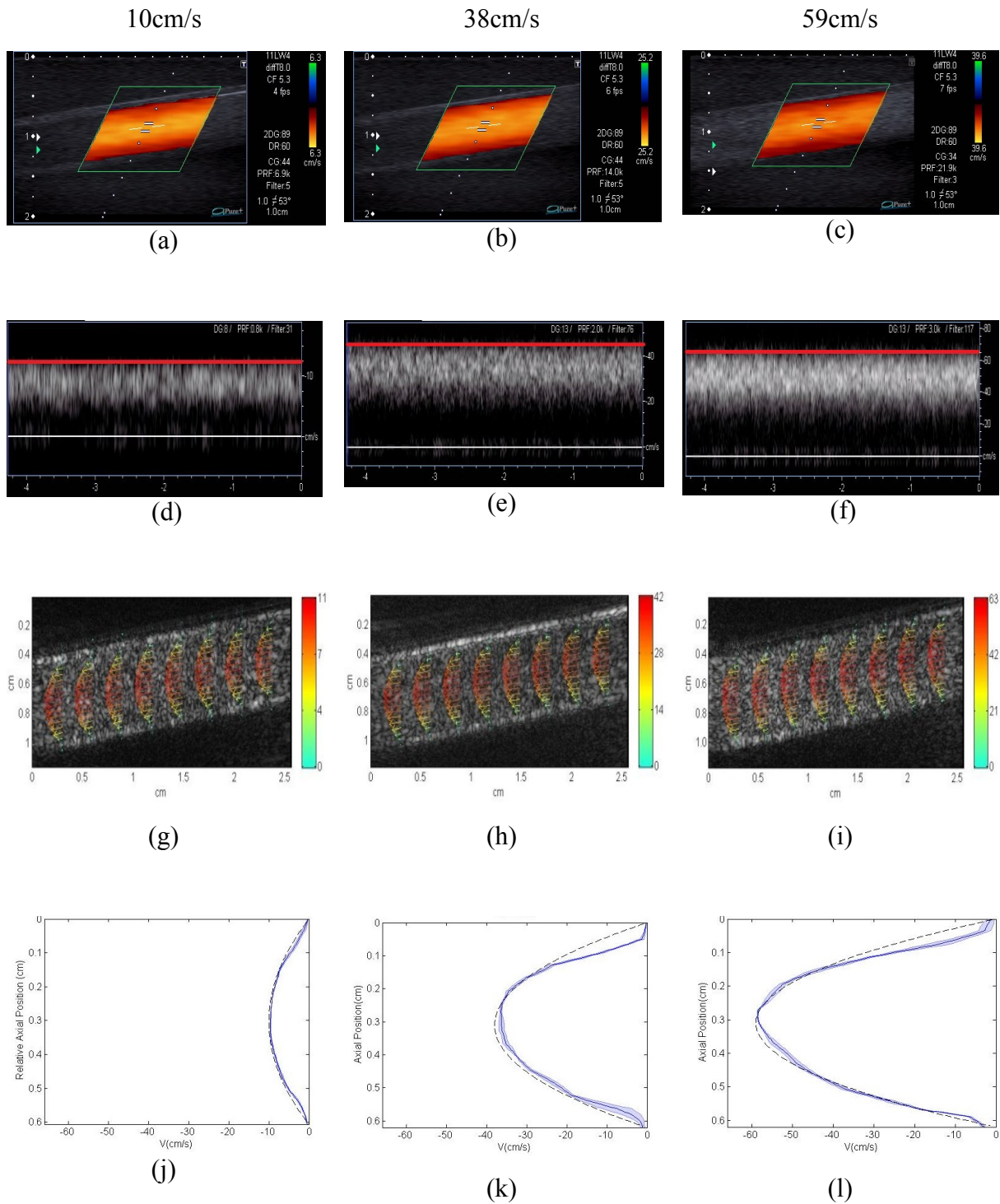


Figure 2.6: Comparison of Doppler ultrasound with plane wave UIV under 3 flow rates with peak velocities of 10cm/s, 38cm/s and 59cm/s. (a)-(c) Colour Doppler obtained using standard beam-formed colour Doppler processing. (d)-(f) Spectral Doppler measurements acquired from the corresponding window located in the colour images. The red line indicates the maximum velocity. (g)-(i) UIV derived quantitative vector visualization. Each measurement is averaged over 5 ms. (j)-(l) Measured flow profiles corresponding to the three flow conditions show a high correlation with the analytical derived flow profile (dashed line). Note: results in (j)-(l) were averaged over a 1mm lateral position where the solid line represents the mean value and the shading represents the standard deviation.

2.3.1.2 Pulsatile Flow

Pulsatile flow was generated using a mechanical pulsatile pump (Harvard Apparatus 1405 pulsatile blood pump, Harvard Apparatus Ltd, Kent UK). With plane wave UIV, the high spatio-temporal dynamics of the pulsatile flow were effectively tracked by the plane wave UIV at a 1 ms time resolution. Figure 2.7 shows the spatial velocity profile measured with Doppler and UIV at different phases of the dynamic flow, marked on a spectral measurement as indicated in Figure 2.7 (m). The colour vector images, Figure 2.7 (e)-(h), show a high correlation with the colour Doppler measurements, Figure 2.7 (a)-(d). Flow with a blunt velocity profile moving in the forward direction can be observed during the peak systolic phase in Figure 2.7 (e). This undeveloped flow profile is common in arteries under pulsatile flow conditions when the centreline velocity accelerates as the boundary layer retards velocity near the wall [152], [153]. After the peak systolic phase, a developed laminar flow can be observed (Figure 2.7f). Reversed flow is observed near the vessel wall in Figure 2.7 (g) and a non-uniform forward flow pattern can be seen in Figure 2.7 (h). All these velocity profiles are relevant to the *in-vivo* condition where pulsatile flow applies [153]. The velocity profiles across the tube at each reference time point are shown in Figure 2.7 (i)-(l). The temporal velocity profile within the same spatial window used by spectral Doppler was also extracted from the plane wave UIV results and overlaid on the spectral Doppler measurement as show in Figure 2.7 (m). There is a good agreement between the plane wave UIV measurement and the Doppler spectral measurement at the same spatial location.

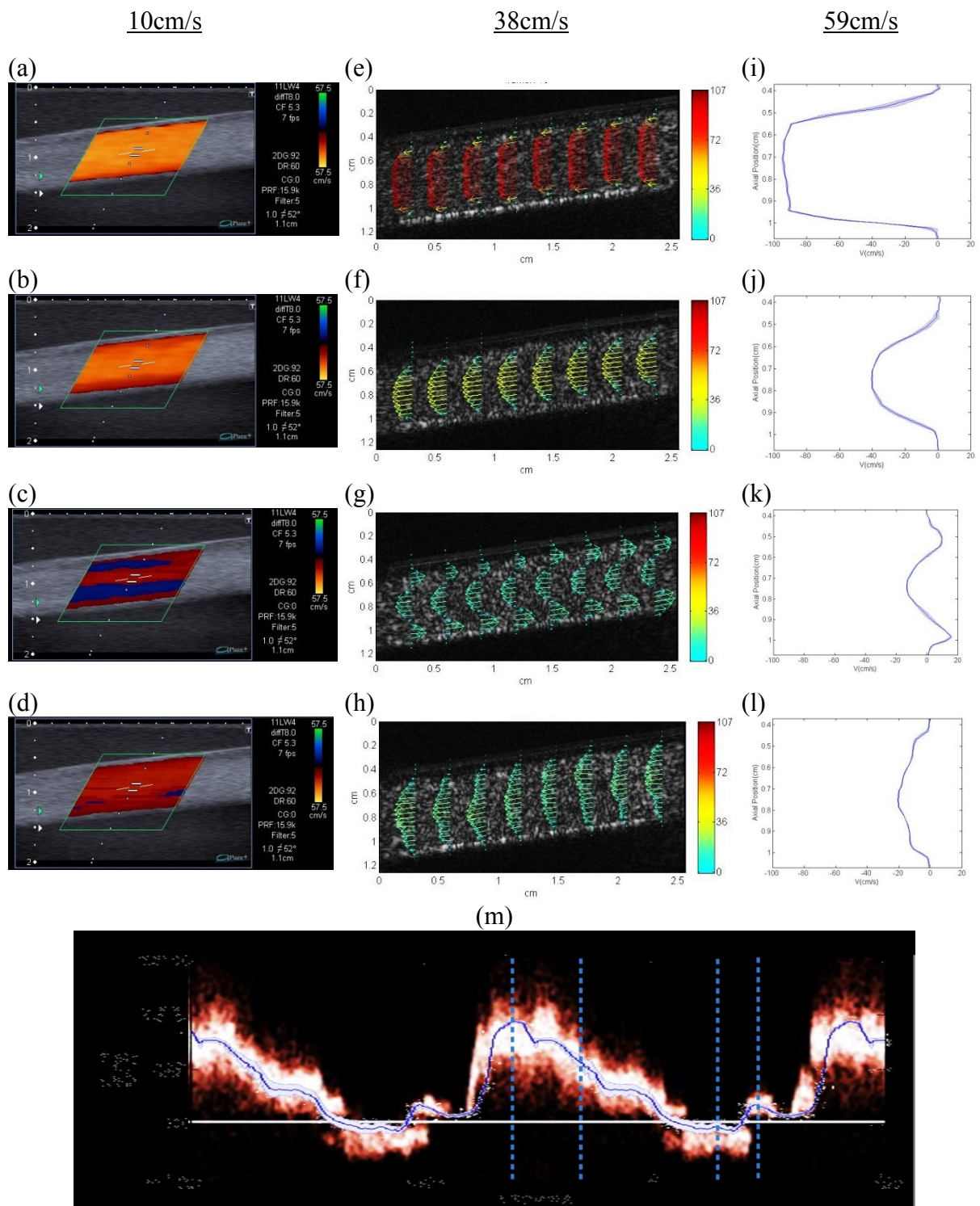


Figure 2.7: Visualization and quantification of pulsatile flow at the four phases indicated by dotted lines in (m). (a)-(d) Colour Doppler measurement acquired at the 4 different phases. (e)-(h) Colour vector of flow measurements obtained using plane wave UIV, and their corresponding flow profiles (i)-(l). (m) Comparison of centreline velocity obtained from plane wave UIV (blue line) with spectral Doppler. Note: results shown in (i)-(l) were averaged over a 1mm lateral position where the solid line represents the mean value and the shading represents the standard deviation. Spectral Doppler measurement and plane wave UIV results shown in (m) were averaged over a 1mm x 1mm window located at the centre of the vessel.

2.3.2 Carotid Bifurcation Model

In this study, instead of using 6 angled plane wave transmissions, contrast images were acquired with 3 angled transmissions within the same angle range. By reducing the compounding, the dynamic flow patterns were effectively tracked using the plane wave UIV system with an acquisition rate of 2000fps and played back at 50fps. To highlight the transitory behaviour of the flow, flow patterns at different time points indicated in Figure 2.8 (g) are illustrated in a collection of images in Figure 2.8 (a)-(f). Figure 2.8 (a)-(b) show the forward flow during the acceleration and the peak systolic phase. A separation is subsequently seen near the vessel wall at the carotid bulb during the post-systolic phase (Figure 2.8c) and persists during the deceleration phase as illustrated in (Figure 2.8d). The separation appears immediately after peak systole and slowly dissipates until it reaches the peak diastolic wave at which moment the flow resumes forward motion again (Figure 2.8e). Finally, at the end of the diastolic wave, the separation near the carotid bulb reappears (Figure 2.8f). This finding agrees with those observed in [73].

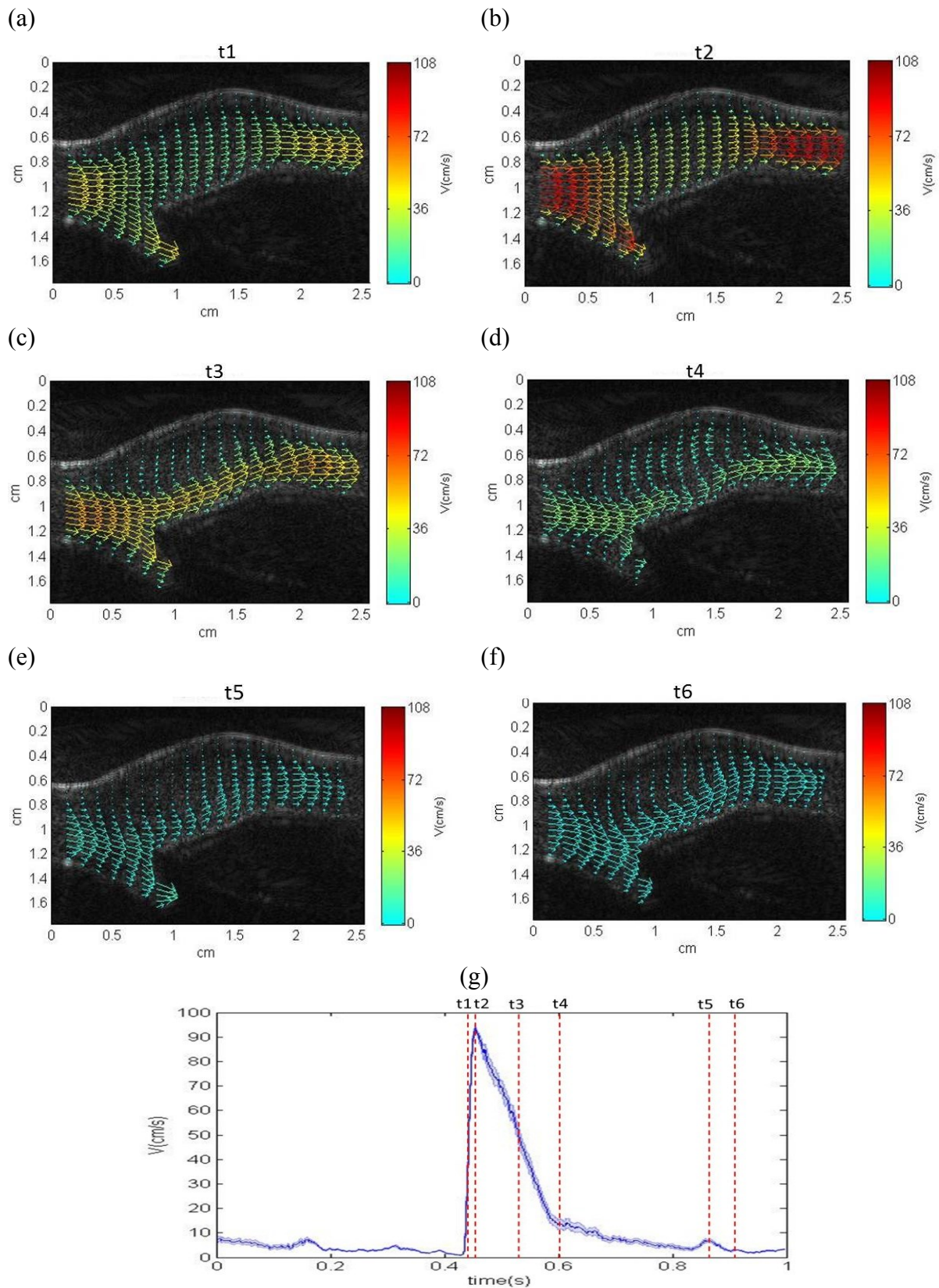


Figure 2.8: (a)-(f) Quantitative visualization of key flow patterns obtained at different phases under pulsatile conditions in a model of a healthy carotid bifurcation. (g) Centreline velocity obtained using UIV from a 1×1 mm range gate located within the CCA. The relative time positions of each flow pattern are marked in the velocity plot.

2.3.3 Rabbit

The flow patterns obtained in the rabbit abdominal aorta (between the celiac artery and superior mesenteric artery) during one pulse cycle with 3 angles plane wave compounding and a frame rate of 2.5kHz are illustrated in Figure 2.9. Forward flow can be observed in Figure 2.9 (a), (c) and (d) while reversed flow, and additionally a flow separation, can be seen in Figure 2.9 (b). This finding agrees with the results of [154], [155].

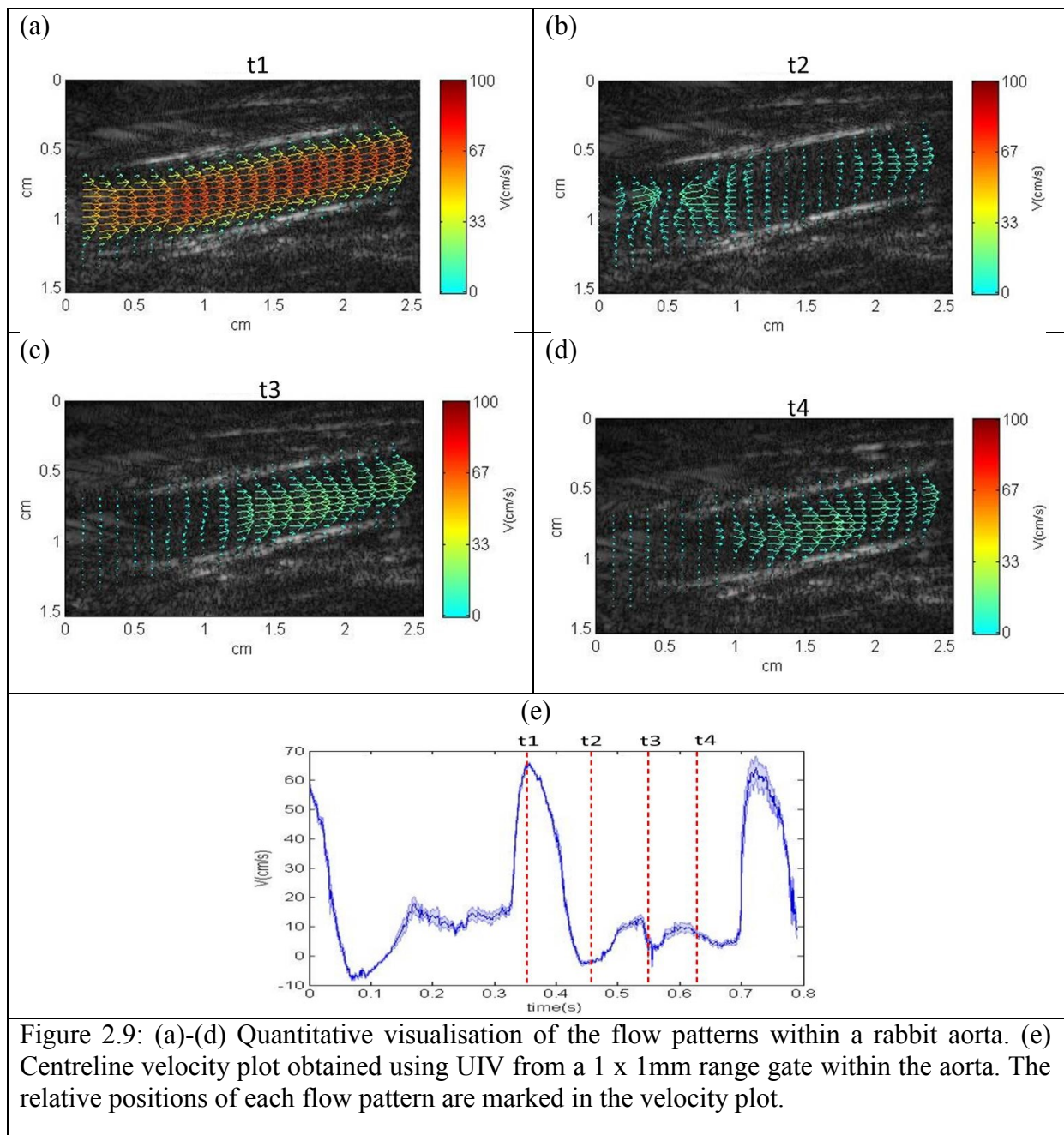


Figure 2.9: (a)-(d) Quantitative visualisation of the flow patterns within a rabbit aorta. (e) Centreline velocity plot obtained using UIV from a 1 x 1mm range gate within the aorta. The relative positions of each flow pattern are marked in the velocity plot.

In addition, an initial qualitative comparison of the result obtained from the developed system and the Doppler system is shown in Figure 2.10. With the 2 kHz acquisition rate, the spatio-temporal flow variations over a wide range of velocities were well tracked using the plane wave UIV and the estimations in Figure 2.10 (b) were found to match the Doppler measurement (Figure 2.10a). However, it should be noted that as a result of angle dependence of the Doppler measurement, the highest flow velocity in the aorta appears slower than that in the branch (renal artery).

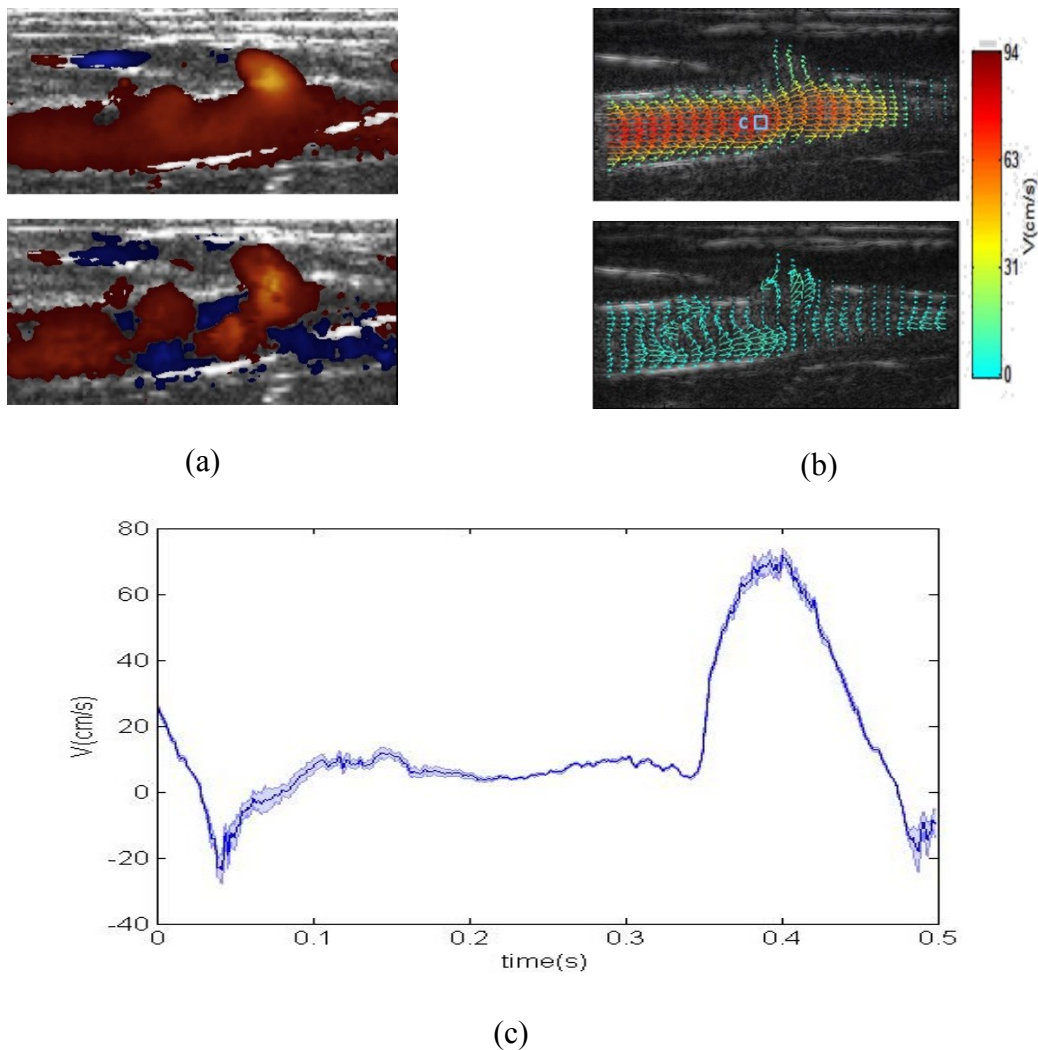


Figure 2.10: Comparison of (a) a colour Doppler image, (b) quantitative visualisation of flow patterns estimated using UIV analysis and (c) centreline velocity extracted from a 1 x 1mm range gate within the aorta shown in (b).

2.4 Discussion

In this chapter, a high-frame ultrasound UIV system and methodologies have been developed for quantifying dynamic arterial flow, using plane wave ultrasound, microbubble contrast agents, Pulse Inversion contrast imaging sequence, and UIV algorithms. Initial *in-vitro* evaluation on straight vessel and carotid mimicking phantoms in comparison with both theoretical calculations and reference Doppler techniques demonstrated the potential of the new system as an accurate, sensitive, angle-independent and full field-of-view velocity mapping tool capable of tracking fast and dynamic flows.

The high temporal resolution of plane wave UIV, compared with existing line-by-line scanning, enables a much wider range of velocities to be measured using the speckle tracking approach. For example, given an imaging depth of 6.4cm that enables a pulse repetition frequency (PRF) of 12 kHz, as used in this study, a maximum frame rate of 2000 fps can be achieved with three angle compounding and a pulse inversion sequence. This is a 40-fold increase in frame rate which enables the tracking of velocities up to 6m/s compared to the conventional approach, where the frame rate would be limited by the line-by-line scanning to a maximum of 50fps when 128 scanning lines are used. It should also be noted that while a maximum temporal resolution of 12 kHz can be achieved if a single plane wave imaging approach is used; there is a trade-off between temporal resolution, spatial resolution, and contrast image sensitivity.

Furthermore, plane wave imaging would allow a reduction in the errors that arise when determining flow velocity with line-by-line scanning as reported by Zhou and colleagues [120]; with the traditional approach, flow velocity is underestimated when the beam sweeping direction is opposite to the flow direction and overestimated when the beam sweeping direction is the same as the flow direction.

Microbubble contrast agents can enhance signals from within blood by 20-30dB compared with blood cells alone [156]. Hence the use of microbubble contrast agents significantly improves the sensitivity of ultrasound imaging and consequently the accuracy of velocity estimation. This is particularly essential for imaging deep vessels/heart chambers where low frequency ultrasound is required and blood cell scattering is much less than at high frequencies. The use of contrast specific imaging sequences such as Pulse Inversion also allows better identification of blood-tissue boundaries and facilitates the calculation of haemodynamic wall shear stress.

The capability of plane wave UIV to provide quantitative mapping of highly dynamic flows was illustrated in Figure 2.7. The signal to noise ratio in the lumen is high and the speckle patterns and their movement are clearly visible. With the acquisition rate (1000fps) beyond normal display frame rate, we demonstrated that plane wave UIV are capable of resolving fast, spatio-temporally changing pulsatile flow. The evolution of flow patterns in a complete pulse cycle was accurately tracked by this technique. An additional advantage of using the plane wave UIV system was that temporal velocity profiles could be extracted from any place in the field of view. As illustrated in Figure 2.7(m), the extracted centreline velocity profile shows a strong correlation with spectral Doppler measurements.

The advantage of using a plane wave UIV system in visualizing complex flow dynamics within a physiologically relevant geometry was illustrated both *in vitro* and *in vivo*. The tracking of fast changes of flow in both space and time can be seen in Figure 2.8-Figure 2.10. Complex flow patterns in a complete pulse cycle - specifically the forward streamline flow and vortical flow at the carotid bulb in the phantom study, or forward and reversed streamline flow in the rabbit abdominal aorta - were demonstrated. These transitory behaviours of the flow cannot be visualised with standard Doppler imaging but were visible using high frame-rate UIV.

In recent years, several flow measurement techniques which utilize high frame-rate ultrasound imaging have emerged including ultrafast Doppler, vector Doppler, or ultrafast speckle tracking. While these have shown improved performance over conventional ultrasound imaging systems, the use of a divergent or unfocussed beam and the weak scattering from the RBCs means that the signal to noise ratios and contrast of these high frame-rate ultrasound images are lower than conventional ultrasound images [50]. This problem gets worse when lower frequencies need to be used in deeper vessel imaging. In this study, we have used microbubbles contrast agents which can significantly increase signal to noise ratios from within blood. In comparison to conventional contrast imaging, the unfocussed beam of the plane wave imaging UIV system also reduces bubble disruption.

It should also be noted that the Doppler measurements, shown in Figure 2.6(d)-(f) and Figure 2.7(m), were overestimates, due to the geometrical aperture problem [149], [157] and the use of microbubbles which widen the spectral measurement. The former arises because the Doppler ultrasound is received by a finite size of aperture. The range of angle by which the aperture received the Doppler beam generated a range of Doppler frequencies. The highest frequency is received at one edge of the aperture where the angle between the beam and the target is smallest whereas the lowest frequency occurs on the other edge. The latter, on the other hand, is due to the secondary radiation force created when a high pulse repetition frequency is used. Such forces are capable of pushing and destroying microbubbles, causing Doppler spectral broadening; this has been investigated and discussed by Tortoli and his colleagues [151], [158].

In the rabbit experiment, out of plane motion was observed, especially during the deceleration phase as the aorta contracts; this caused part of the 2D image on the left-hand side to move from the lumen to the vessel wall, as shown in Figure 2.9(c) and (d). This is an

inherent limitation of 2D ultrasound in imaging 3D structures, and may well be resolved using 3D ultrasound.

Although the developed high frame-rate UIV system has shown great promise to provide accurate quantification of the flow field, it can still be further improved. Optimisation of the ultrasound system parameters such as the number of plane waves compounded, plane wave tilting angle, frequency, acoustic pressure and pulse length can enhance images and velocity estimation. For instance, the use of a small number of angles with large angle tilting to enhance spatial and temporal resolution in plane wave excitation, as used in this study, can cause high grating lobes that could impact on the accuracy of speckle tracking. Further investigation and optimisation of the imaging parameters needs to be conducted to balance the spatial and temporal resolution while optimise tracking accuracy. In addition, it should be noted that the compounding required in plane wave imaging could result in the very fast flow dynamics being missed; The motion artefacts generated as a result of incoherent compounding could also significantly degrade the image quality [159] which in turn impact the velocity estimation. A trade-off has to be made between temporal resolution and spatial resolution. However, the benefit of the proposed method - being able to track a wide range of flow velocities within the whole imaging plane with great sensitivity and good spatial resolution - make it an exciting addition to existing tools for flow imaging and quantification.

In addition to the technique refinement, another important aspect that can be improved is the phantom design. Physical properties of the flow phantom need to be considered carefully in comparison to the properties of tissue or vessel [160], [161]. In the present work, the fabricated carotid phantom has a speed of sound of 1801m/s, which is higher than that for the human arteries (1570m/s). This leads to total internal reflection at the interface between the vessel and the surrounding medium, and to refraction of the incident sound wave which distort the flow signals. The high attenuations of the compliant photopolymer

(1.58dB/mm/MHz) comparing to the nominal attenuation coefficient of 0.5dB/cm/MHz would significantly reduce the flow signal and further impact the velocity estimation. As a solution, polyvinyl alcohol cryogel [162], whose acoustic and mechanical properties can be optimised by adjusting the number of freeze-thaw cycles, can be used as an alternative tissue mimicking material.

The proposed technique is capable of producing a spatially resolved flow velocity map over time, containing a large amount of data. In this study, as an example of what can be extracted, a temporal velocity profile at a single location within the vessel is displayed for the carotid phantom (Figure 2.7m & Figure 2.8g) and the rabbit abdominal aorta *in vivo* (Figure 2.9e & Figure 2.10c). Further hemodynamic indices that could be derived from the data include not only the existing indices obtained by Doppler, such as peak and average velocities and flow pulsatility, but also quantities related to spatial variation of the flow velocity such as flow vorticity and local wall shear rate. Furthermore, real time processing using a graphics processing unit is also desirable to provide an immediate quantitative measurement for clinical applications. Finally, this study uses a 2D imaging system which is not capable of tracking out of plane flow. For future *in vivo* applications, a 3D imaging approach would need to be developed.

2.5 Conclusion

The developed quantitative flow mapping system, integrating high frame rate plane wave imaging, ultrasound imaging velocimetry and microbubble contrast agents, has shown great potential as an accurate, sensitive, angle-independent and full field-of-view velocity measuring tool capable of mapping fast and dynamic flows *in vivo*.

Chapter 3 - Toward a reliable and accurate flow velocity measurement using plane wave UIV

In this chapter, we have proposed a modified plane wave UIV analysis based on incoherent ensemble correlation, to avoid the motion artefacts that is attributed to the coherent compounding. A simulation model, which coupled the ultrasound simulator with the analytical flow solution, was implemented to demonstrate the effects of motion artefacts and to evaluate the accuracy of the UIV techniques in estimating flow velocity. The effects of motion artefacts on the normal UIV technique and the robustness of the modified UIV against the motion artefacts were demonstrated. Comparing with the ground truth, the modified UIV performed better than the normal UIV technique in the simulation studies to provide a robust, angle independent and accurate full FOV flow velocity measurement. *In-vitro* investigations on two carotid bifurcation phantoms (normal and diseased) were also conducted and their relative differences in terms of flow patterns were demonstrated. From the *in-vitro* results, the effect of the image artefacts which subsequently caused the failure of the normal UIV analysis to track highly accelerated jet flow was demonstrated. With the effective use of incoherent ensemble correlation, a more robust flow velocity estimation method was presented.

3.1 Introduction

The high frame rate capability of plane wave ultrasound imaging offers new possibilities in various clinical applications. By transmitting an unfocused pulse over the full aperture, a relatively low resolution image can be reconstructed using dynamic receive beamforming. To synthesise virtual dynamic transmit focussing, a coherent plane wave compounding technique in which several tilted plane waves are transmitted and the radio-frequency echoes are coherently summed in receive beamforming, has been implemented. This effectively

generates a high resolution image with SNR and contrast comparable to the conventional ultrasound while keeping the temporal resolution within a millisecond[49], [50].

The coherent plane wave compounding approach is capable of achieving very high frame rate imaging without compromising the image quality and penetration; however, it relies on the assumption that the imaged medium remains stationary during the compounded scan sequence, which is not the case in many *in-vivo* situations. This assumption is also applied to synthetic aperture imaging to produce B-mode images with the quality comparable to conventional ultrasound imaging. Motion between the transmit events may result in phase misalignment and prevent perfect coherent summation. The effects of tissue motion on image quality when using coherent plane wave compounding and synthetic aperture imaging have been investigated in [45], [162]–[164], indicating a potential severe degradation of spatial resolution, SNR and contrast.

While tissue motion may affect the image quality, flow motion between emissions may also impact the flow velocity estimation using existing UIV techniques. Unlike the conventional ultrasound system, the decorrelation of the RF signals not only depends on the spatial velocity gradient, but also the motion artefacts when the coherent compounding approach is employed. As a high resolution image is formed from multiple low resolution images, the phases of the beamformed line get distorted and the point spread function is smeared out when the target is moving between the two transmit events. Therefore, the flow velocity cannot be estimated using the traditional approaches [165]. To deal with the motion artefacts and restore the image quality, several techniques have been proposed which include limiting the transmit events, modifying the transmit sequence, applying autocorrelation motion compensation or cross-correlation motion and phase aberration corrections [162], [165]–[167]

A flow velocity mapping technique using plane wave UIV has been demonstrated in Chapter 3 [121]. However, directly applying the UIV algorithm to the coherently compounded speckle images would suffer from motion artefacts, which in turn would impact on the velocity estimation. Such errors are illustrated in Figure 3.1 where the normal UIV technique developed in Chapter 3 failed to estimate the high-speed jet flow in the presence of motion artefacts. In this chapter, a modified UIV analyses using an incoherent ensemble correlation approach has been proposed, to circumvent the motion artefacts and generate robust velocity estimations. Synthetic ultrasound images, consisting of a straight tube phantom driven by steady and pulsatile flow with known ground truth, were generated to evaluate our technique. To further highlight the performance of our technique, *in-vitro* studies on two anthropomorphic carotid bifurcation phantoms were also presented.

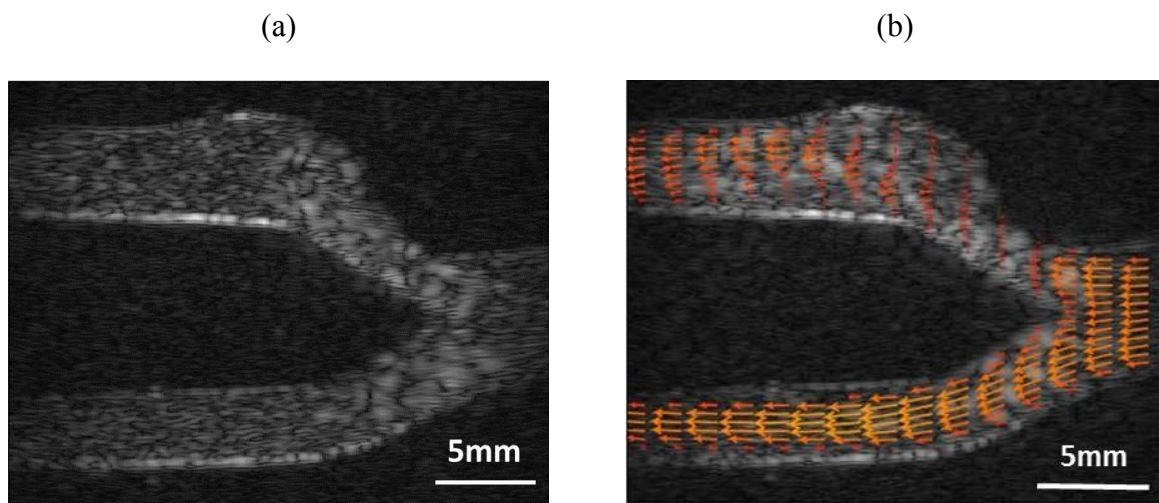


Figure 3.1: (a) Compounded plane wave image at the peak systole shows the motion artefacts at the stenosed bifurcations area due to high velocity flow. (b) Flow velocity vectors estimated using normal UIV shows significant underestimation of the jet flow due to the presence of motion artefacts in the compounded plane wave images.

3.2 Methods

3.2.1 Velocity Estimation using a modified UIV analysis

The workflow of the modified UIV analysis is shown in Figure 3.2a. Similar to the UIV analysis performed in Chapter 3, multi-grid windows deformation technique with 3-point Gaussian peak estimator were implemented to estimate the sub-pixel displacements. A simple 2D spatial medium filter was also applied to remove the spurious vectors. However as flow motion between emissions may affect the coherent compounded images, ensemble correlation was performed incoherently on the low-resolution images formed by a single transmission instead of the summed images.

We referred to this technique as incoherent ensemble-correlation approach (Figure 3.2b). Multiple low resolution images were cross-correlated and ensemble-averaged to estimate the flow velocity. This incoherent summation of the correlation planes was hypothesised to increase the SNR and peak detectability from the correlation plane, therefore making the algorithm more robust in estimating flow velocity from the speckle images. To validate this hypothesis, comparison between the modified UIV with the normal UIV analysis was demonstrated in simulation and *in-vitro* experiment.

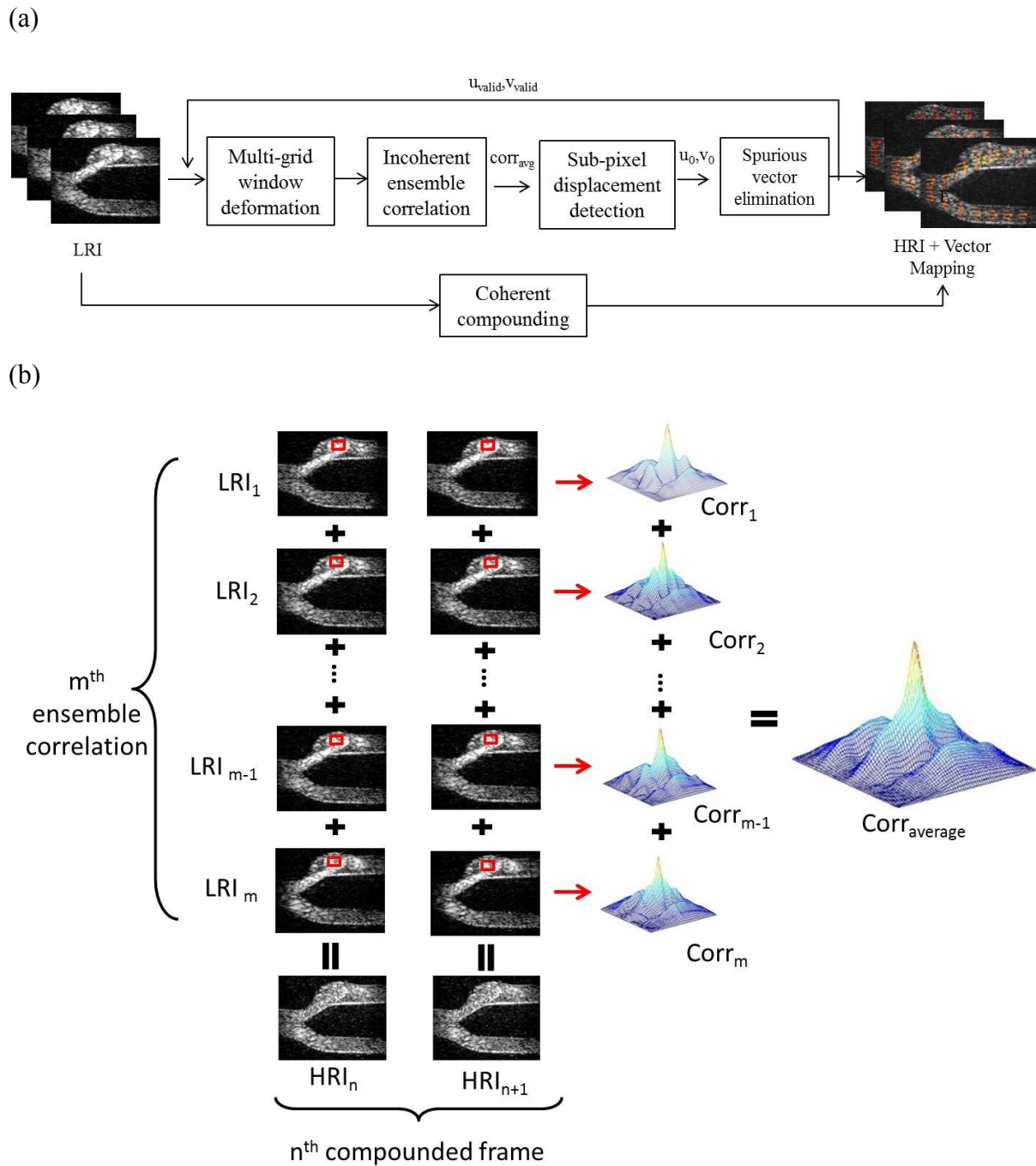


Figure 3.2: (a) Basic workflow of our modified UIV analysis to generate velocity mapping overlaid on the high resolution images (HRI) (b) Principle of incoherent ensemble-correlation approach where cross-correlation is applied to each pair of low resolution images (LRI) to generate an average correlation with higher signal to noise ratio and peak detectability.

3.2.2 Ultrasound Flow Simulation

3.2.2.1 Flow model generation

To evaluate our techniques, synthetic ultrasound images were generated from an ultrasound flow simulation which coupled the analytical flow solution with the ultrasound simulator. Such models are necessary to compare the outcome of our developed technique with the known ground truth computed from the analytical solution. Under such circumstance, a rigid model, consists of a straight cylindrical vessel phantom filled with Newtonian fluid driven by analytical solution was created.

Poiseuille Flow

A straight vessel phantom with inner diameter of 3mm was created. Steady laminar flow with parabolic flow profile was generated by moving the flow scatterers at radius r from the centre of the vessel with the velocity as follow:

$$v(r) = v_0 \left(1 - \frac{r^2}{R^2}\right) \quad 3-1$$

where v_0 is the centreline velocity and R is the radius of the vessel.

To investigate the accuracy of the flow estimation, flow simulations under three different flow rates (Table 3.1) were generated. The rigid tube was simulated with a beam-to-flow angle of 60° and the radial velocity errors are calculated. To further examine the error that maybe due to the flow direction, another two simulations with beam-flow angle of 75° and 90° were generated under the fast flow condition.

Table 3.1: Flow parameters of 3 simulated laminar flows

Flow Condition	v_0 (cm/s)	Reynold number ($Re_{\bar{v}}$)
Slow	20	300
Medium	50	700
Fast	80	1200

Womersley Flow

While arterial flow is pulsatile, Womersley flow was generated as described by Evan[168]. In brief, pulsatile flow is considered as the sum of both steady flow component and a series of oscillatory components. Poiseulle's equation can be reformulated to describe the relationship between pressure difference and volume flow rate [169]:

$$Q = \frac{M'_{10}}{\alpha^2} \frac{\pi R^4}{\mu L} \Delta P \sin(\omega t + \phi + \varepsilon'_{10}) \quad 3-2$$

where $\Delta P \sin(\omega t + \phi)$ is the pressure difference, $\alpha = R\sqrt{\omega/\nu}$ is the Womersley number, and M'_{10} and ε'_{10} are complex functions of the non-dimensional parameter α . From the volume flow rate, [170] has shown that it is possible to calculate the velocity profile for a sinusoidal flow given by:

$$V_m \left(\frac{r}{R}, t \right) = \frac{1}{\pi R^2} Q_n |\psi_n| \cos(\omega t - \phi_n + \chi_n) \quad 3-3$$

$$\psi_n \left(\frac{r}{R}, \tau_n \right) = \frac{\tau J_0(\tau_n) - \tau J_0\left(\frac{r}{R}\tau_n\right)}{\tau J_0(\tau_n) - 2 J_1(\tau_n)} \quad 3-4$$

Where J_m is the m^{th} order Bessel function of the first kind, $\tau = j^{3/2} \alpha$, $|\psi_n|$ and χ_n represent the amplitude and angle of the complex function ψ_n . Therefore, the whole velocity profile can be calculated from the volume flow rate when the entrance effects are neglected.

Following the Fourier decomposition theorem, the mean velocity waveform can be expressed in a series of sinusoidal waveform such that

$$\bar{V}(t) = V_0 + \sum_{n=1}^{\infty} V_n \cos(n\omega t - \phi_n) \quad 3-5$$

And the time evolution of the velocity profile can be determined by summing the velocity profile from each harmonic.

$$V\left(\frac{r}{R}, t\right) = 2V_0 \left(1 - \frac{r^2}{R^2}\right) + \sum_{n=1}^{\infty} V_n |\psi_n| \cos(n\omega t - \phi_n + \chi_n) \quad 3-6$$

In this study, velocity profile for the common carotid artery (CCA) and common femoral artery (CFA) were generated using the data given in Table 3.2.

Table 3.2: Fourier components for flow velocities in the common carotid artery and common femoral artery. (Data adapted from Evans[168]).

Common carotid					Common femoral				
Diameter		= 6.0 mm			Diameter		= 8.4mm		
Heart rate		= 60 bpm			Heart rate		= 60 bpm		
Viscosity		= 0.004 kgm ⁻¹ s ⁻¹			Viscosity		= 0.004 kgm ⁻¹ s ⁻¹		
<i>n</i>	<i>f</i>	<i>α</i>	<i>V_n</i>	<i>φ_n</i>	N	<i>f</i>	<i>α</i>	<i>V_n</i>	<i>φ_n</i>
0	-	-	1.00	-	0	-	-	1.00	-
1	1.03	3.9	0.33	74	1	1.03		1.89	32
2	2.05	5.5	0.24	79	2	2.05	7.7	2.49	85
3	3.08	6.8	0.24	121	3	3.08	9.5	1.28	156
4	4.10	7.8	0.12	146	4	4.10	10.9	0.32	193
5	5.13	8.7	0.11	147	5	5.13	12.2	0.27	133
6	6.15	9.6	0.13	197	6	6.15	13.4	0.32	155
7	7.18	10.3	0.06	233	7	7.18	14.5	0.28	195
8	8.21	12.4	0.04	218	8	8.21	15.5	0.01	310

3.2.2.2 Ultrasound Simulation

Field II [171], [172] was used to simulate a realistic ultrasound system. Arbitrary transducers and imaging pulse sequences can be created based on the spatial impulse responses estimation described by Tupholme and Stephnishen[173], [174]. Using the linear systems theory, the ultrasound field at any given point can be estimated by taking into account the transducer estimation function, spatial impulse response of the transmitting and receiving aperture, and the electro-mechanical transfer function of the transducer.

In Field II, tissue and bubble are modelled as a collection of point scatterers with different reflectivity as shown in Figure 3.3. The reflecting coefficient was adjusted to mimic strong signal generate from the contrast agents, producing a contrast to tissue ratio of about 15-20dB similar to our experimental data. To ensure a fully developed speckle with a Gaussian distributed radio frequency (RF) signal, a minimum of 10 scatterers per resolution cell were simulated[175].The rigid vessel wall was generated as multiple stationary scatterers with density of about $350/\text{cm}^3$ while the Newtonian fluid was represented as random distributed point scatterers with density of $200/\text{cm}^3$ to mimic the specular reflections at the lumen-wall. The positions of the fluid scatterers were updated for each transmitted ultrasound beam during the simulation using the displacement determined by the analytical solution in Eqn. 3-1and Eqn. 3-6.

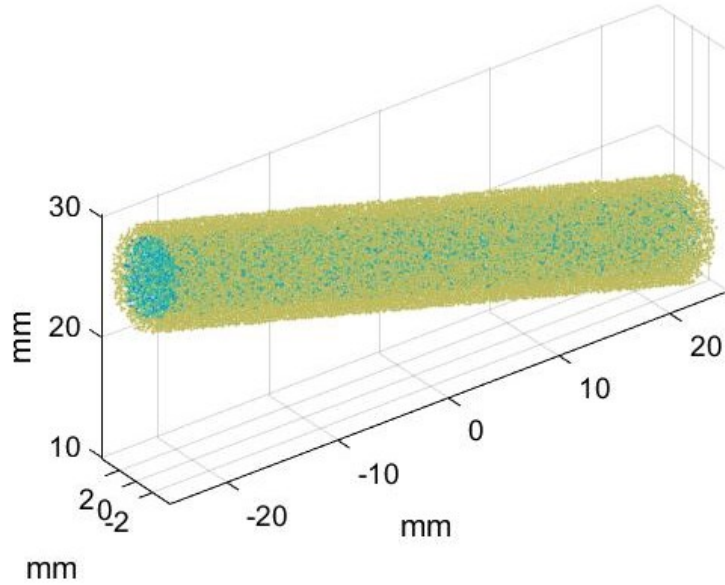


Figure 3.3: A scatterer model consisting of stationary vessel wall scatterers (yellow) and moving flow scatterers(blue).

To better represent our fast ultrasound system, the parameters of a L12-3v linear array transducer and compounded plane wave imaging sequence were used to simulate the RF-signal as illustrated in Table 3.3. A higher sampling frequency is necessary to reduce the side lobes and better represents the simulated spatial impulse response. The transducer elements were also divided into smaller sub-apertures such that every scatterer is in the far field of each sub-element [172]. In our case, the element was further divided into 4 sub-elements in the elevational direction to ensure the far field of each sub-element is at an axial distance of 1.3mm while keeping the simulation time short. A software GPU-beamformer [44], in which delay and sum operations were applied to the RF-data, was used to generate synthetic ultrasound images for further analysis. Also in an effort to simulate realistic ultrasound images, random Gaussian noise was included in individual post-beamformed RF-data yielding a signal-to-noise ratio of 20dB

Table 3.3: Field II simulation setup

Probe parameter		Imaging Parameter	
Centre Frequency	8MHz	Imaging mode	Plane wave

Number of Element	128	Transmit Frequency	8MHz
Element Pitch	0.2mm	Excitation pulse	1 cycle sinusoidal
Element Height	5mm	PRF	10kHz
Sampling frequency	100MHz	Compounding angle	5
Elevational Focus	20mm	Angle Range	20 ⁰
Number of Sub-aperture	4		

3.2.3 In vitro flow experiment

3.2.3.1 Ultrafast plane wave imaging system

A Vantage 128 research platform (Verasonics, Redmond, WA, USA) was configured to acquire high frame rate plane wave ultrasound images. With a L12-3v linear array transducer mounted to image the flow phantom, real time rf-data were recorded in the local memory and later transfer to a computer through a high-speed PCI-Express and beamformed using the GPU-beamformer for further analysis. This system has been used in our flow velocity mapping studies in the previous chapter.

3.2.3.2 Microbubble contrast agents and contrast imaging mode

Microbubble contrast agents were used in this study to enhance the ultrasound signal within the flow stream. It was prepared using the recipe described by Sheeran[140] resulting in a solution containing 5×10^9 micobubbles/mL with an average size of 1 μ m [141]. In this study, microbubbles were diluted in the blood mimicking fluid (BMF), which comprised 90% pure water and 10% glycerol, to a concentration of 2×10^5 micobubbles/mL. The concentration used is clinically relevant and has been used in our previous study [121], [144].

To acquire ultrasound contrast images, pulse inversion (PI) imaging sequences were implemented. Coupled with high frame rate imaging, the developed system is capable of enhancing the contrast and signal to noise ratio (SNR) of the generated image while keeping

the temporal resolution in the kHz range. And since microbubbles behave non-linearly generating harmonic signals, pulse inversion imaging is capable of suppressing tissue signals which mainly oscillate at the fundamental frequency, while maintaining harmonic signals generated from microbubbles. The PI images have been found to be superior to B-mode and second harmonic imaging in terms of better specificity in imaging microbubbles[176].

In this study, compounded plane wave PI imaging sequences were implemented using the Verasonics and a L12-3v probe such that 6 plane waves, interleaving 3 positive and 3 negative 4MHz 1-cycle pulse with angle spanning between -10^0 and 10^0 (10^0 angle step), were transmitted to acquire pre-beamformed rf-data at the pulse repetition frequency (PRF) of 10kHz. Typical settings for the data acquisition are given in Table 3.4.

Table 3.4: Ultrafast imaging data acquisition configurations

Probe Parameter		Imaging Parameter	
Probe	L12-3v	Imaging Mode	Plane wave PI
Centre Frequency	8MHz	Transmit Frequency	4MHz
Number of Elements	128	Excitation Pulse	1 cycle
Element Pitch	0.2mm	PRF	10kHz
Element Height	5mm	Compounding Plane Wave	6
Sampling Frequency	32MHz	Angle range	20^0 (10^0 step)
Elevational Focus	20mm	Imaging depth	5cm

3.2.3.3 Anthropomorphic flow phantoms

To evaluate our developed techniques for accurate flow estimation, two anatomically realistic flow phantoms[162], one of normal bifurcation geometry and one of diseased bifurcation geometry with 50% eccentric stenosis, were used. The phantoms are wall-less phantom fabricated with polyvinyl alcohol (PVA) cryogel as the tissue-mimicking material. In brief, a mould which mimics an idealised carotid bifurcation junction of the common carotid artery

(CCA), internal carotid artery (ICA) and external carotid artery (ECA) was first designed using computer-aided design tools and fabricated using 3D printing technology. Note that the inner diameter of the CCA, ICA and ECA are 6mm, 4.2mm and 3.2mm. The vessel mould was then mounted onto a phantom box and the PVA mixture was cast around the vessel tube and subjected to three freeze-thaw cycles. Once the elastic phantom was formed, the wall-less phantom was withdrawn from the mould and connected to a pump for operation. .

The flow phantom has an average acoustic speed of 1535 ms^{-1} and an attenuation coefficient of $0.229 \text{ dB}/(\text{cm MHz})$. The elastic modulus was found to be 106.1 kPa . To emulate a physiological condition, the inlet of the carotid model was connected to a pulsatile pump (Havard Apparatus 1405 pulsatile blood pump), circulating fluid comprised of BMF solution and diluted microbubbles at 60 pulses/min pulse rate, delivering flow at 2mL/s average flow rate and 4mL/s systolic flow rate.

3.2.4 Error Quantification

To evaluate the performance of the developed technique, the measured centreline velocity was compared to the reference centreline velocity and the corresponding mean error was calculated as follow:

$$ME = \frac{\int_0^t v_c(t)dt - \int_0^t v_{cgt}(t)dt}{\int_0^t v_{cgt}(t)dt} \times 100\% \quad 3-7$$

where v_c is the measured centreline velocity vector at a single spatial location, v_{cgt} is the reference centreline velocity extracted from the ground truth, and t is the sampling time. While the mean error only compared the centreline velocity, normalised root mean square error (NRMSE) was also performed to compare the spatial velocity profile within the FOV as follows:

$$NRMSE(t) = \frac{1}{v_{cgt(\max)}} \sqrt{\frac{1}{n} \sum_{x=1}^n (v(x, t) - v_{gT}(x, t))^2} \times 100\% \quad 3-8$$

where v and v_{gT} are the estimated and reference velocity profile, $v_{cgt(\max)}$ is the maximum reference centreline velocity, and n is the number of spatial sampling point.

3.3 Results

3.3.1 Poiseuille Flow Simulation

3.3.1.1 Effect of flow velocity on the accuracy of UIV flow tracking

The effects of flow velocity on the compounded plane wave image quality are shown in Figure 3.4. With the increasing of flow rate, the contrast, resolution and signal intensity of the imaged flow reduced due to the loss in focussing capability of the coherent plane wave compounding imaging.

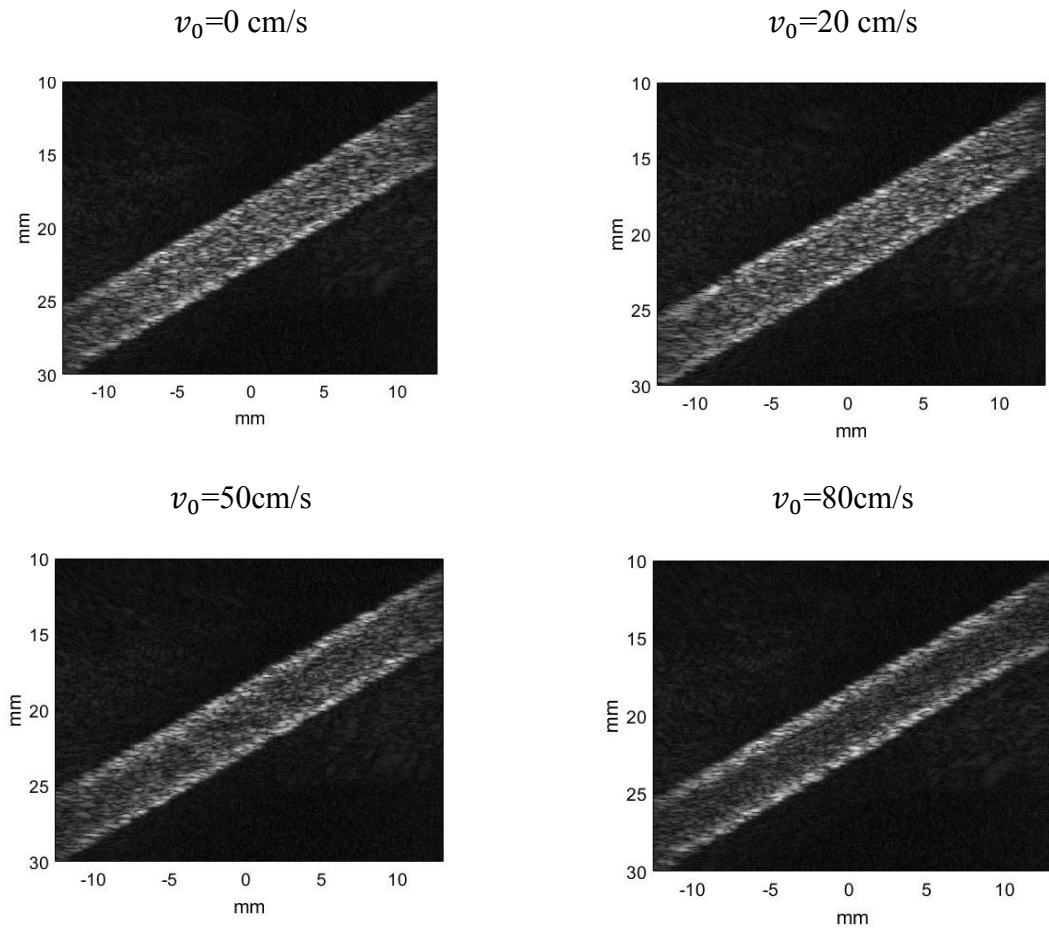


Figure 3.4: The effects of flow velocity on the compounded plane wave image quality.

To evaluate the effects of motion artefacts on the flow estimation, the normal UIV technique and the modified UIV technique were performed to estimate the 2D flow velocities as shown in Figure 3.5. With velocity estimated under different flow rate, the accuracy of both methods is summarised in Table 3.5 . It is clearly seen that the modified UIV performs better than the normal UIV method. Highly accurate measurements with less error and variance were produced when using the modified UIV method, and more importantly the estimations were not affected by the motion artefacts even under the fast flow condition.

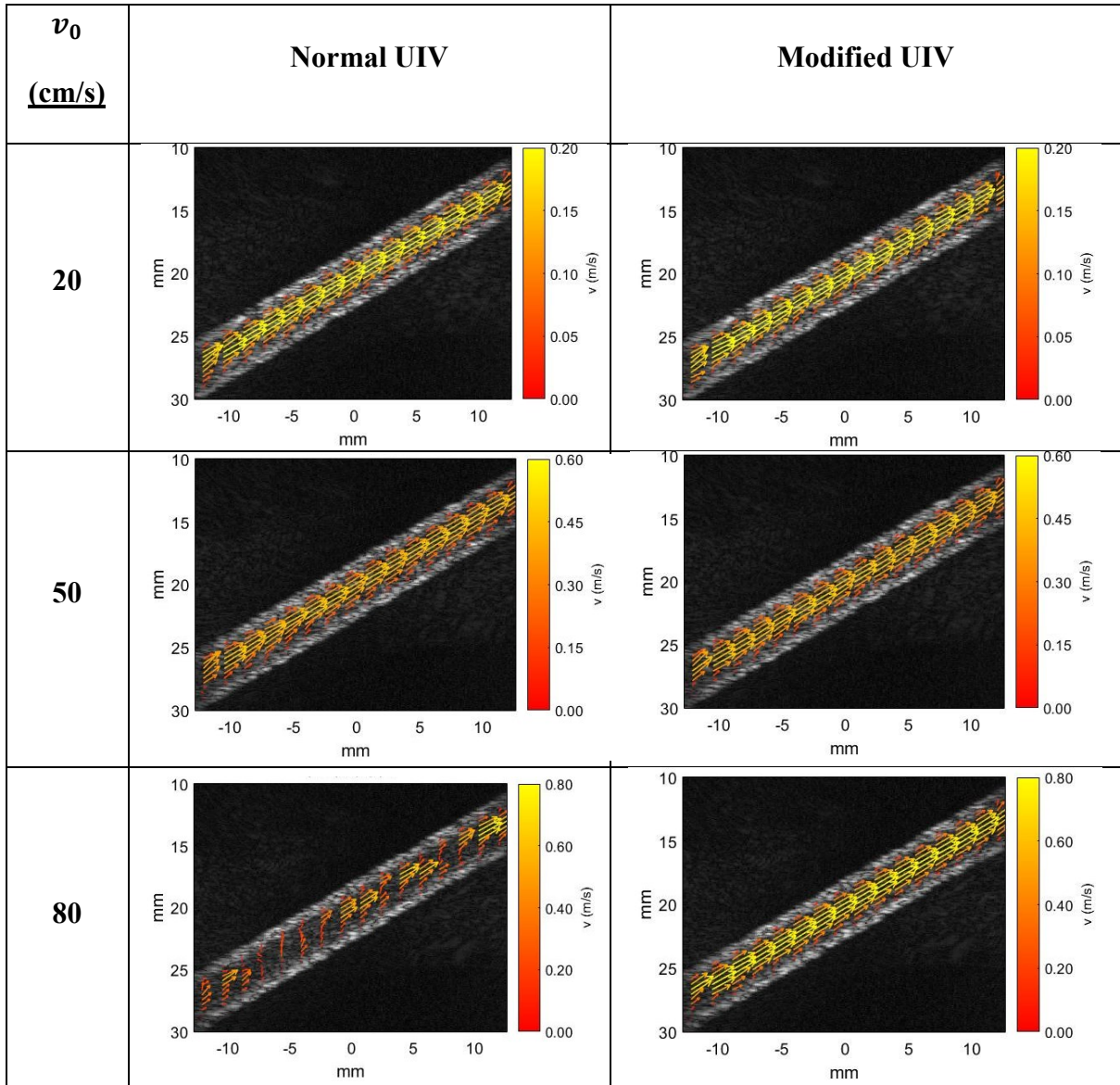


Figure 3.5: Flow velocity vectors estimated using normal (left) and modified UIV(right) under slow, medium and fast flow. The tube is tilted in an angle of 60° to the ultrasound beam.

Table 3.5: Accuracy of the normal UIV and the modified-UIV approach a under different flow rates. Note that the error is calculated based on the radial velocity profile.

V_0 (cm/s)	<u>Normal UIV</u>		Modified-UIV	
	ME (%)	NRMSE (%)	ME (%)	NRMSE (%)
20	-6.08 ± 4.81	1.11 ± 0.03	-6.01 ± 3.24	1.10 ± 0.04
50	-13.78 ± 3.75	3.35 ± 0.09	-8.13 ± 2.45	2.68 ± 0.06
80	-69.16 ± 27.74	12.96 ± 2.09	-6.57 ± 1.54	5.55 ± 0.19
Average Error (%)	-44.50 ± 12.10	5.81 ± 0.74	6.90 ± 2.41	3.11 ± 0.10

3.3.1.2 Effects of flow direction on the accuracy of UIV flow tracking

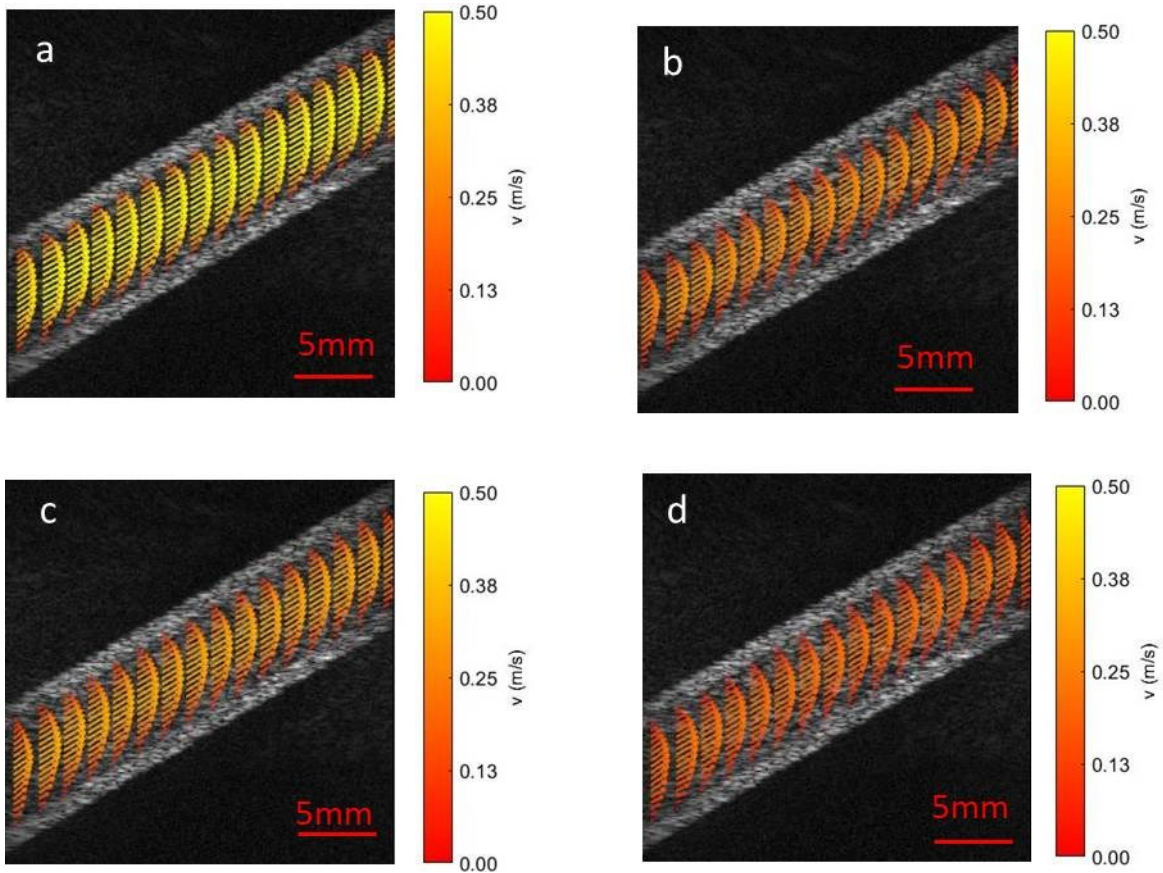
The accuracy of both UIV estimations under different beam-to-flow angles is presented in Table 3.6. Overall, the modified UIV outperforms the normal UIV to provide more accurate velocity estimations. The results also suggest that the flow direction has substantial influence on the normal UIV estimation. The fast flow which cannot be well measured using the normal UIV method at the beam-to-flow angle of 60° , were better estimated at the beam-to-flow angle of 75° and 90° . Such results are expected as a lateral displacement will generate less artefacts than an axial displacement [164]. This is mainly due to the spatial frequency in the axial direction is much higher than the lateral direction and a higher phase coherence is required to avoid motion artefacts in the axial direction.

Table 3.6: Accuracy of the normal UIV and the modified-UIV approach under different beam-to-flow angle. Note that the error is calculated based on the radial velocity profile

Angle (⁰)	<u>Normal UIV</u>		Modified-UIV	
	ME (%)	NRMSE (%)	ME (%)	NRMSE (%)
90	-4.33 ± 0.44	1.06 ± 0.02	4.32 ± 0.41	1.07 ± 0.02
75	-7.38 ± 1.68	2.66 ± 0.09	5.04 ± 1.13	2.18 ± 0.07
60	-69.16 ± 27.75	12.96 ± 2.09	6.57 ± 1.54	4.62 ± 0.19
Average Error (%)	26.96 ± 9.96	5.56 ± 0.73	5.31 ± 1.03	2.62 ± 0.09

3.3.2 Pulsatile Flow Simulation

Temporal snapshots of the flow velocity vectors estimated using the modified UIV analyses are illustrated in Figure 3.6 and Figure 3.7 to highlight the flow structures in the CCA and CFA. Unidirectional flows, mainly parabolic, were observed throughout a pulse cycle in the CCA (Figure 3.6a-d) while more complex flow structures including non-parabolic flow and reverse flow were observed in the CFA. The transitory behaviour from an undeveloped flow with blunt profile (Figure 3.7a) to a parabolic flow (Figure 3.7b) was seen during the systole phase while a flow reversal (Figure 3.7c) and a non-uniform flow profile (Figure 3.7d) were observed during the end systole and diastolic phase of the cardiac cycle. Note that such flow profiles were observed in the *in-vitro* experiment in Chapter 3.



(e)

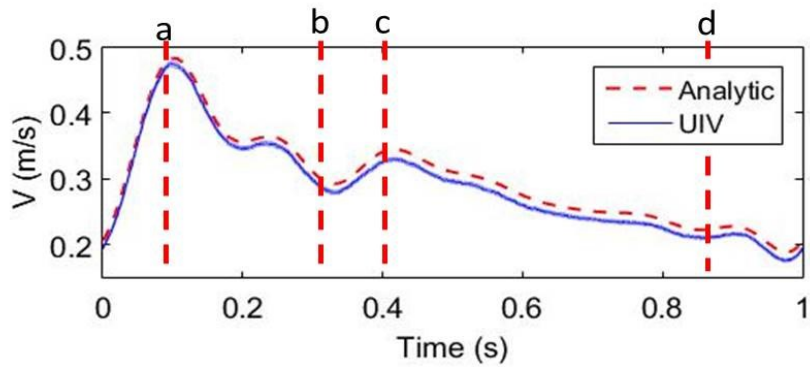
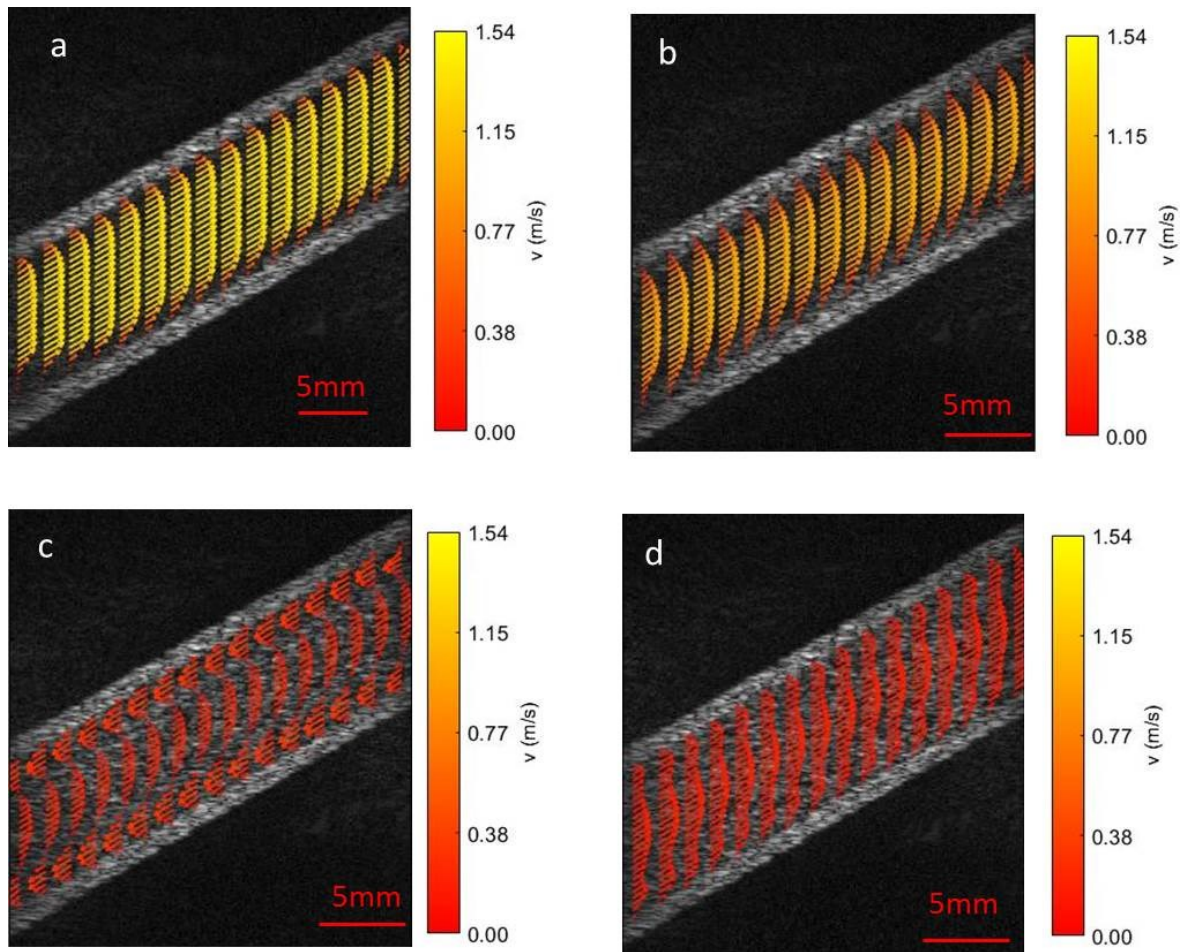


Figure 3.6: (a-d) Snapshots of the flow velocity vectors derived using the modified ultrasound imaging velocimetry (UIV) method obtained at different phases in a simulated common carotid artery. (e) Comparison of the centreline velocity estimated using the UIV method and the analytical ground truth. The relative time of each flow pattern is marked in the centreline velocity plot and the shading in the UIV measurement represents the standard deviation.



(e)

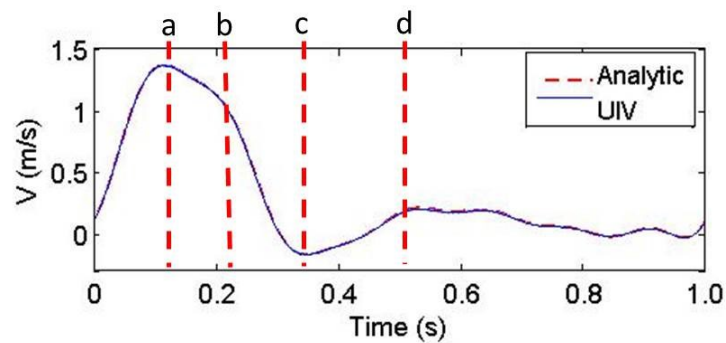


Figure 3.7: (a-d) Quantitative flow measurements of the modified ultrasound imaging velocimetry (UIV) obtained at four phases in a simulated common femoral artery (e) Estimated centreline velocity overlaid on the ground truth solution to show the accuracy of UIV. The relative time of each flow pattern is marked in the centreline velocity plot and the shading in UIV measurement represents the standard deviation.

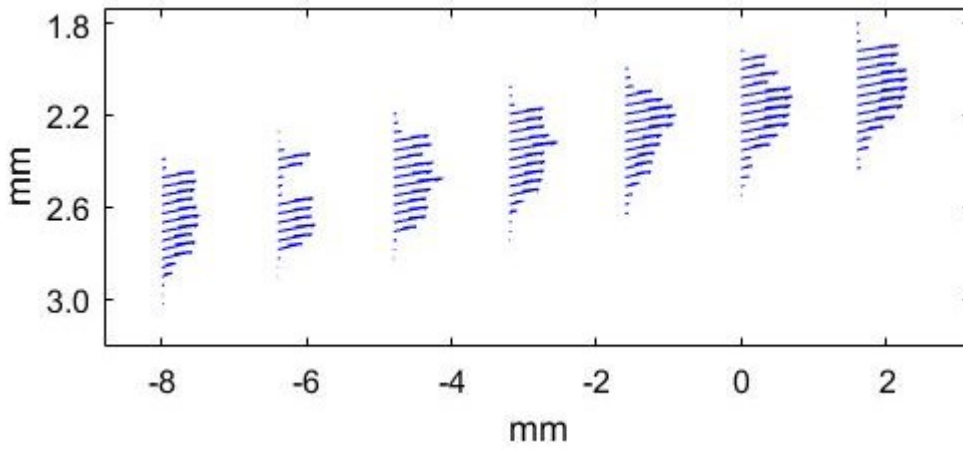
To evaluate the performance of the normal and modified UIV, the measured centreline velocities and spatial-temporal velocity profiles were compared to the analytical solution and their accuracy is summarised in Table 3.7. Both methods performed well to track the pulsatile flow within the CCA and CFA with errors less than 5%. The modified UIV performed slightly better than the normal UIV. Although the high velocity and acceleration flow affected the compounded plane wave images, normal UIV estimation was still capable of measuring the flow up to a very high accuracy. This can be explained by the smaller spatial velocity gradient and the spatial filtering of the spurious vector eliminations algorithm which reduce the estimation errors as shown in Figure 3.8.

Table 3.7: Accuracy of the normal UIV and the modified UIV approach under different simulated artery

Vessel	<u>Normal UIV</u>		Modified-UIV	
	ME (%)	NRMSE (%)	ME (%)	NRMSE (%)
CCA	-3.99 ± 0.60	2.41 ± 0.98	3.89 ± 0.72	2.04 ± 0.72
CFA	-1.03 ± 0.49	2.05 ± 2.86	1.00 ± 0.18	1.49 ± 1.61
Average Error (%)	2.51 ± 0.55	2.23 ± 1.92	2.45 ± 0.45	1.77 ± 1.17

While the calculated NRMSE in Table 3.7 were averaged within a pulse cycle, the temporal variation of the NRMSE is shown in Figure 3.9. From the temporal plot, it is clearly seen that although the error was flow dependent, modified UIV performed better than the normal UIV with smaller error produced in both the CCA and CFA cases.

Before Spurious Vector Elimination



After Spurious Vector Elimination

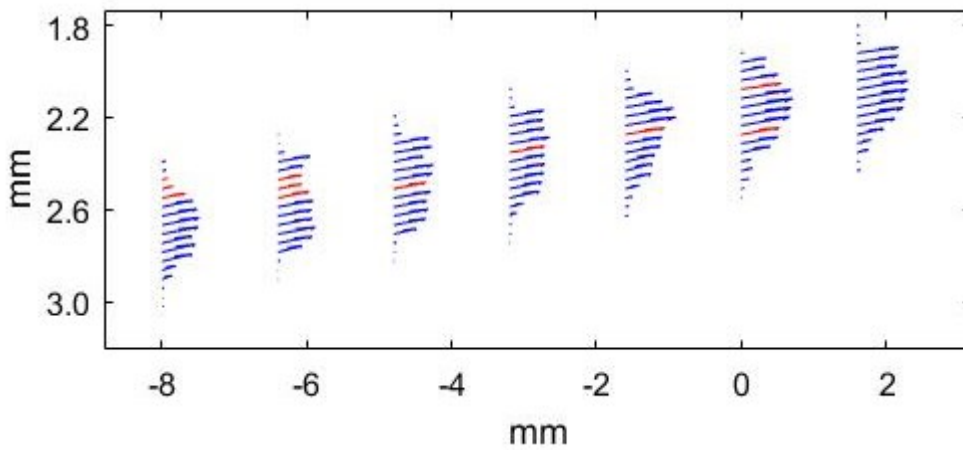
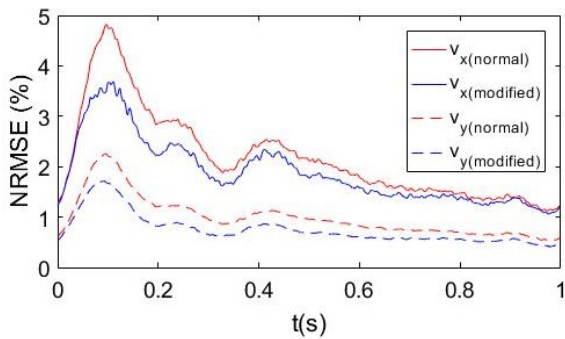


Figure 3.8: Flow velocity vectors before and after the spurious vectors elimination process. Note that the red vectors are the velocity estimations replaced after the spatial filtering.

CCA



CFA

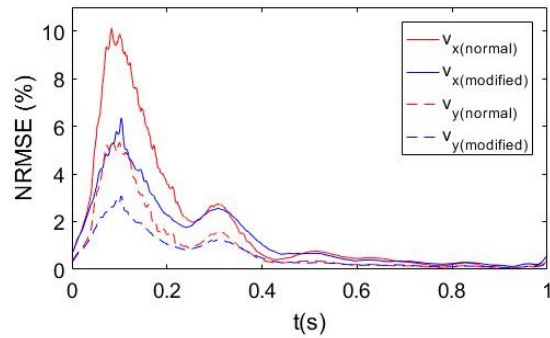


Figure 3.9: Temporal variation of the normalised root mean square error (NRMSE) calculated using the normal UIV and modified UIV in a simulated common carotid artery

(CCA) and a common femoral artery (CFA).

3.3.3 In-vitro flow experiments

Figure 3.10 illustrates the time-resolved quantitative visualisation of a highly dynamic flow in a healthy and a diseased carotid bifurcation phantom under the same pulsatile flow condition. For the healthy carotid phantom, a uni-directional forward flow was observed during the systolic upstroke and peak systole (Figure 3.10a). A separation subsequently emerges near the ICA sinus immediately after the peak systole and slowly dissipates during the post-systolic phase (Figure 3.10b), causing a flow reversal near the carotid bulb. When the diastolic pulse produced a secondary upstroke, the flow moves forward again (Figure 3.10c) and followed by the reappearing of the separation near the carotid bulb during the post-diastolic phase (Figure 3.10d). Similar flow behaviour has been observed in Chapter 3.

With similar inlet flow, flow patterns appearing in a diseased carotid phantom are also presented in Figure 3.10 (f-i). Due to the 50% eccentric stenosis at the ICA branch, the formation of a high-velocity flow jet at the ICA stenosis throat can be clearly seen during the systolic upstroke. It follows a path from the inner wall at the proximal ICA to the straight outer wall region at the distal ICA. The reorientation of the jet flow tangential to the wall and the bouncing of the jet stream upon hitting the outer wall can be visualised. In addition to the jet formation, the formation of the two flow separations, one at the carotid bulb and another along the inner wall of ICA can also be observed. The separation at the carotid bulb appears near the peak systole and persists almost the entire cardiac cycle while the separation at the inner wall of distal ICA emerges and dissipates twice within a pulse cycle. The recirculation at the inner wall only occurs after the jet stream becomes narrower and completely crosses over from the inner wall to the distal ICA, forming a flow divider between two recirculation zones during the post-systole and post-diastolic (Figure 3.10g,i), but not during the peak systole and peak diastolic wave (Figure 3.10f,h) as the jet is more dispersed after travelling through the

inner wall at the proximal ICA. To clearly depict the separation, streamline images plotted using matlab function to show the separationslocation and the temporal velocity profile extracted from several locations are illustrated in Figure 3.11. It should be noted that these findings agree with those observed in [73], [177]

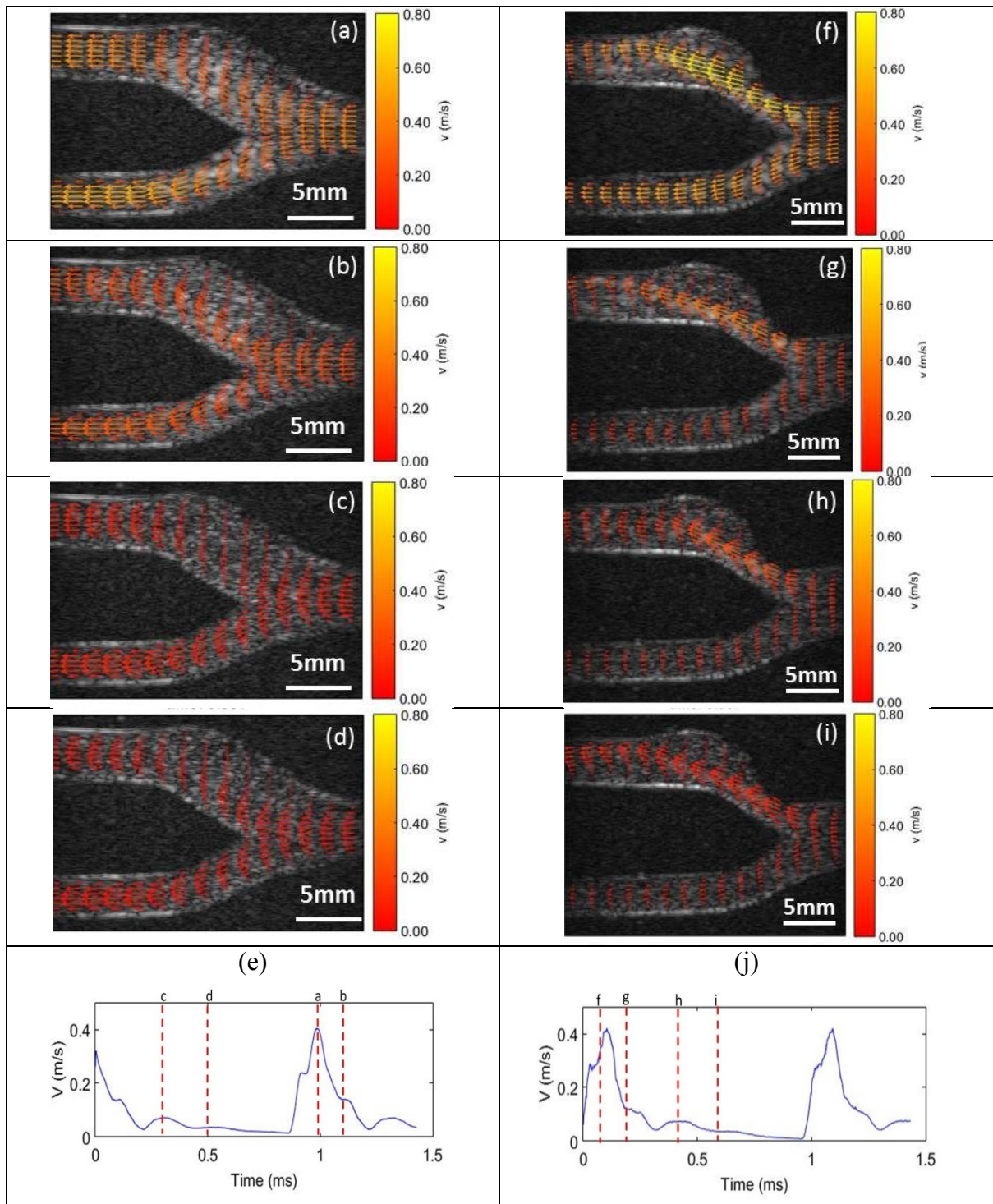


Figure 3.10: Key quantitative velocity measurements derived from modified ultrasound imaging velocimetry (UIV) to highlight the spatio-temporal varying flow profile in (a-d) a healthy carotid bifurcation phantom; (f-i) a diseased carotid bifurcation phantom. (e,j) Centreline velocity extracted from the common carotid artery. The relative position of each flow velocity is marked in the velocity plot.

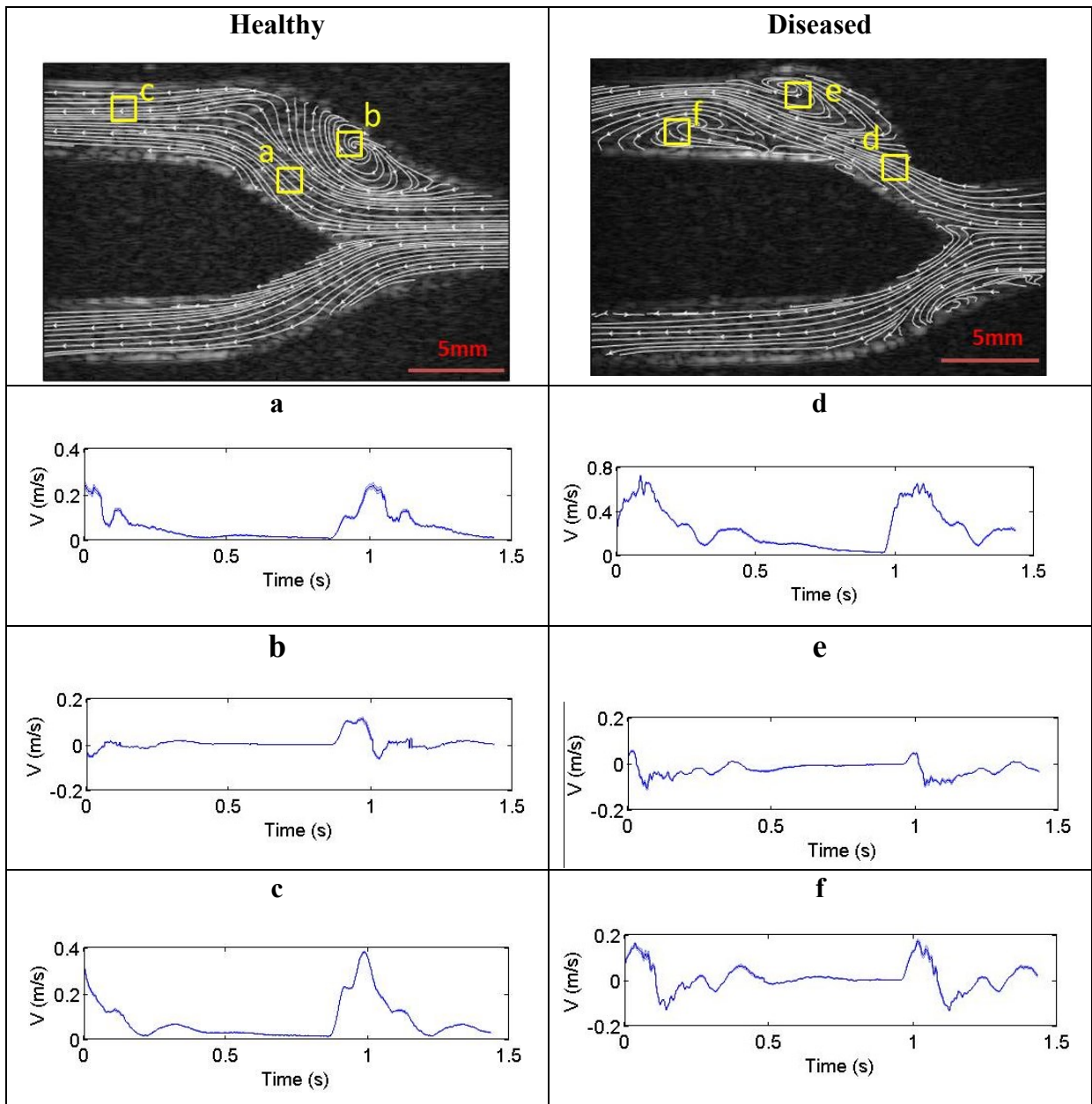


Figure 3.11: Quantitative flow velocity extracted from the yellow boxes depicted in the streamline images on a healthy and diseased carotid phantom. Note that the streamline images are generated from velocity estimation during diastole.

While the effectiveness of the modified UIV to track highly dynamic flow has been demonstrated, the comparison of our new approach with the normal UIV method was performed and is illustrated in Figure 3.12. It can be clearly seen that motion artefacts had affected the estimation of the highly-accelerated jet flow when normal UIV was applied to measure the flow. This error can be avoided when the modified UIV analysis was performed on the low-resolution images. The highly-accelerated jet flow at the ICA throat which cannot

be tracked with the normal UIV method can now be effectively estimated using our proposed method. It is evident that the modified UIV is robust against motion artefacts and a more accurate estimation can be achieved.

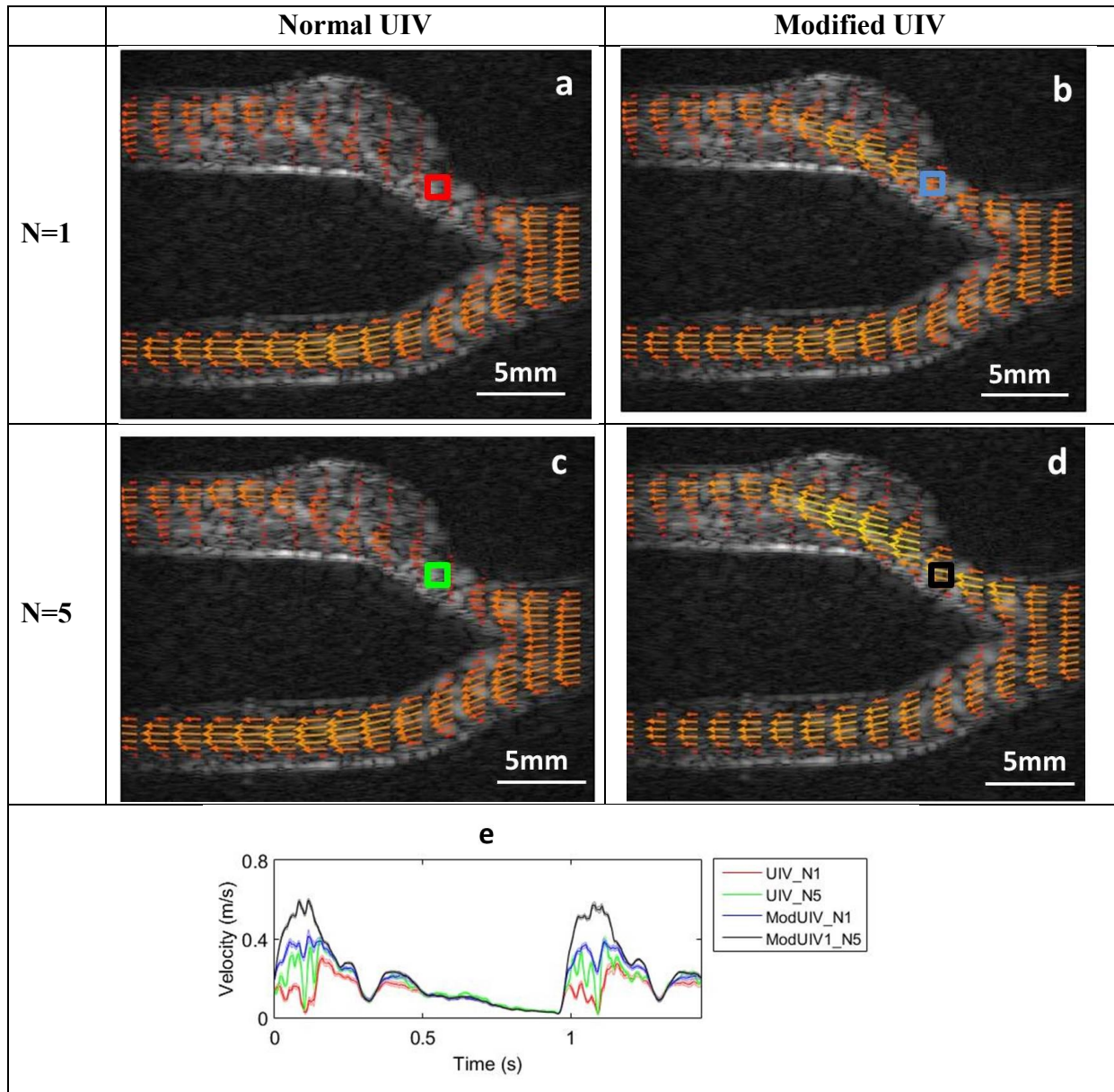


Figure 3.12: (a-d) Comparison of the flow velocity mapping at peak systole demonstrate the robustness of modified UIV approach to track highly-accelerated flow when similar amount of high resolution images (N) are used to estimate the flow velocity. (e) Velocity plot extracted at the stenosed throat marked in (a)-(d). It should be noted that normal UIV approach estimate the flow using the final compounded images (N) but modified UIV analysis is performed on the multiple low resolution images ($M \times N$, and $M=3$) used to construct the same compounded image.

3.4 Discussion

In this study, a new modified-UIV technique based on an incoherent ensemble correlation approach has been developed to circumvent the effects of motion artefacts when a plane wave coherent compounded technique is used to image flow. The performance of the modified analysis was compared to the normal UIV analysis in simulations and experiments, indicating the robustness of the new approach against motion artefacts while demonstrating the potential of the system to provide angle-independent, accurate, full FOV velocity estimation.

The coherent plane wave compounding technique has been introduced as a method to improve the image quality of plane wave imaging while retaining a very high frame rate. However, this is not the case when the technique is used to image flow. Noticeable image artefacts in terms of loss of image resolution (the speckle image is blurred), loss of speckle intensity and lower contrast are presented in Figure 3.4. With significant motion artefacts generated in the fast flow condition, normal UIV cannot correctly estimate the flow velocity from the compounded plane wave images (Figure 3.5).

The motion artefacts are flow dependent and direction dependent as illustrated in Figure 3.5, Figure 3.9, Table 3.5, and Table 3.6. Although the motion artefacts have less effect on the velocity estimation in a straight and large vessel as shown in the pulsatile flow cases, it should be noted that *in-vivo* conditions are complex where the vessel geometry and the induced flow is unlikely to be uniform. In this condition, the spatial filtering process included in the existing UIV techniques may not be able to reduce the estimation errors as illustrated in Figure 3.5 and Figure 3.12.

Although the motion artefact may only affect normal UIV technique under a fast flow condition with high spatial velocity gradient, a more robust modified UIV technique is proposed and evaluated. It is evident that modified UIV outperforms the normal UIV to

provide more accurate velocity measurements and is robust against motion artefacts as shown in both steady and pulsatile flow simulations. Even though the incoherent ensemble correlation was performed on the low-resolution images, the flow estimation accuracy is not compromised.

The capabilities of the modified UIV to visualise and quantify the complex flow dynamics within a physiologically relevant geometry were illustrated in Figure 3.10 and Figure 3.11. Specifically, the streamline and the transient behaviour of the separation at the carotid bulb in the normal carotid bifurcation geometry, the formation of flow jet at the stenosed region, and the appearance of the two separations (each at the opposite site of the jet trajectories) in a diseased carotid bifurcation phantom, can be clearly visualised in the vector images or streamline images. The quantitative temporal velocity profile could also be extracted. Although there exists the out-of-plane motion due to the secondary flow, the in-plane motion can be well estimated with our technique. The visualisation of such fast changing flow dynamic, which is not possible when using the conventional UIV or standard Doppler, were demonstrated using our high-frame rate UIV technique.

The advantage of the modified UIV algorithm to circumvent the motion artefact was also shown in Figure 3.12. High frame rate imaging is believed to increase the maximum velocity that can be measured, however highly accelerated jet flow motion between emissions results in significant image artefacts produced at the stenosed region when coherent plane wave compounding is no longer achieved. Such an image artefact leads to a rapid change of the speckle pattern between consecutive compounded images and limits the normal UIV method in tracking the highly accelerated jet flow (Figure 3.12a-b). Our new technique, on the other hand, overcomes the effects of motion artefacts and produces better velocity estimations (Figure 3.12c-d). Velocity estimated from 3 low resolution images ($N=1$, $M=3$) may well retrieve the high-speed jet flow that cannot be estimated from the normal UIV; however, the

in-plane velocity estimation may still be affected by the out-of-plane motion at the jet flow region. By increasing the low-resolution images used to perform the incoherent ensemble correlation ($N=5$, $M=3$), we demonstrated that our new technique reduced the estimation error caused by out-of-plane motion. It is also worth mentioning that our modified UIV method is similar to Doppler techniques that velocity estimation is performed on individual pulses instead of the summed signal. When the estimation is performed on the image reconstructed from a single pulse echo sequence, it may not directly suffer from the intensity or phase variations due to motion artefacts.

While the capability of the modified UIV to overcome the problem of motion artefacts has been found in simulation and *in-vitro* studies, further refinement and evaluation of this technique is required. The straight tube flow simulation model used in this study may not be adequate to fully evaluate the performance of our technique as the flow generated is spatially uniform. A more realistic and complex simulation flow model that incorporates out-of-plane motion and spatially varying flow is necessary to fully evaluate our approach against known ground truth. Such a simulation which combines computational fluid dynamics and ultrasound simulator has been demonstrated by Swillen[178] and can be adapted. Another aspect that can be improved in the simulation is the generation of ultrasound images. As the Field II ultrasound simulator is a linear wave simulator, this has restricted us from modelling the non-linear response of microbubbles to generate contrast images similar to our *in-vitro* experiment. However, it should be noted that the simulation of contrast pulse sequence and non-linear response are possible and can be done by adapting the Creanuis simulator developed by Varray [179]. Finally, as a large amount of data is generated from the high frame rate imaging, real-time processing of the UIV analysis is desirable from a clinical application perspective. With the recent advancement of parallel processing using Graphics

Processing Unit (GPU), the UIV algorithm can potentially deliver real-time velocity estimation.

3.5 Conclusion

A modified plane wave UIV based on the incoherent ensemble correlation approach was developed to avoid the motion artefacts when incoherent compounding occurs. Simulation and *in-vitro* studies demonstrated the circumstances where significant motion artefacts were generated and impact on the normal UIV estimation. The enhanced robustness against the motion artefacts and the accuracy of the modified UIV to provide 2D velocity measurement were demonstrated. Comparing to the ground truth, errors less than 10% under steady flow and 5% under pulsatile flow conditions were found in the simulation studies. The capabilities of the modified UIV algorithm to track fast and spatio-temporally changing flow were demonstrated *in-vitro* on two carotid mimicking phantoms and the effectiveness of the modified UIV to overcome the motion artefact due to coherent plane wave compounding was demonstrated.

Chapter 4 - Accuracy of Plane wave UIV for Wall Shear Stress measurement

Further to the work reported in Chapter 4 where the ability of the plane wave UIV system to provide robust, accurate, angle independent and full FOV velocity mapping has been demonstrated, we extend our technique to provide the spatio-temporal wall shear stress (WSS) distribution in this chapter. Synthetic images generated from the simulation study were used to evaluate the performance of our system to estimate wall shear rate (WSR). As WSR is a differential quantity and sensitive to noise, sensible filter parameters were selected to smooth the velocity profiles prior to WSR estimations yielding a mean error of 8.56% under steady flow condition and 13.97% under pulsatile flow condition. The sensitivity of WSR measurement to the estimation of wall positions was also quantified under a controlled environment. Initial *in vitro* investigations on two carotid bifurcation phantoms (normal and diseased) indicated the potential of the system to simultaneously estimate flow velocity and WSS distribution.

4.1 Introduction

Blood flow patterns, flow velocity or volume flowrate have been widely used to describe the spatio-temporal hemodynamics within a vessel or a lesion. Although there exists several techniques of measuring the flow velocities clinically, a standard technical basis for fluid shear estimation *in-vivo* has not been established [180], [181]. The easiest and most straightforward way to estimate WSS is based on the Hagen-Poiseuille formula where the shear stress in a relatively straight vessel is computed in terms of either average or maximum velocity and the radius of the vessel lumen [182]. However, the accuracy of this expression depends on the validity of the assumptions that the flow is steady and parabolic, the blood

behaves as a Newtonian fluid with constant viscosity, the vessel is axisymmetric and the vessel wall is rigid. These conditions are barely met under physiological conditions where the flow is mainly pulsatile, the vessel is distensible and its diameter is never constant. This therefore limits the application of this technique to estimate the WSS. Another technique to estimate the WSS is based on the determination of the wall shear rate (WSR), which is the flow velocity gradient near the vessel wall, directly from the estimated velocity profile [100], [183]. This produces a more reliable WSR measurement with no assumption of the geometry and flow required; however, the accuracy of this technique depends on the temporal and spatial resolution of the modality used to obtain the flow velocity profile and to track the wall position, and the interpolation or extrapolation algorithm. Due to such constraints, *in-vivo* WSS measurement is limited and the majority of the community is relying on computational fluid dynamics (CFD) where numerical simulation is employed to investigate WSS distribution of a given geometry measured by means of modalities such as computed tomography (CT), Magnetic Resonance (MR), or ultrasound. However, the accuracy of the simulation can be affected by the underlying assumptions on the geometry, wall properties, fluid properties, and most importantly the initial and boundary conditions.

In order to compute the WSS *in vivo*, flow velocity information can be assessed using existing non-invasive imaging modalities such as phase contrast magnetic resonance (PC-MR) [184], [185] and ultrasound [99], [100]. However, it has been a challenge clinically to provide a reliable wall shear stress distribution with the existing medical imaging techniques.

We have developed and evaluated a high frame-rate ultrasound imaging velocimetry (UIV) system for generating flow velocity maps with high spatial and temporal resolution. This technique benefits from the combination of three key elements; ultrasound imaging with high temporal resolution (up to tens of thousands of frames per second) to track fast and time-variant flow within the full field of view, microbubble contrast agents together with pulse

inversion imaging sequence to enhance the signal-to-noise ratio (SNR) and differentiate between the wall-fluid boundary, and finally an advanced UIV algorithm to accurately estimate the flow velocities.

In this work, we extend our previous study to provide spatio-temporal WSS estimations using high frame rate (HFR) UIV, and subsequently evaluate the accuracy of the developed system. Ultrasound flow simulation, implemented in the previous chapter, was used to evaluate our technique. To demonstrate the feasibility of our developed system to provide WSS distribution in addition to the flow velocity vectors, *in-vitro* studies on two anthropomorphic carotid bifurcation phantoms were presented.

4.2 Methods

4.2.1 Wall shear rate estimation

WSR can be measured directly from the time velocity profile acquired near the vessel wall. Not only does this allow us to quantify the wall shear rate in a simple straight tube geometry, but also in any complex configurations such as curved vessels and bifurcations. In this study, WSR distribution was assessed by estimating the velocity gradient from the velocity profile tangential to the wall. It should be noted that as shear rate is a differential quantity, it can be easily affected by UIV estimation errors and noises. To mitigate such effects, a Savitzky-golay (SG-) filter was introduced to locally smooth the velocity profile prior to shear rate estimation. This digital filter smooths the velocity profile by fitting the near wall velocity data with a low degree polynomial using the method of linear least-squares [186]. Prudent steps needs to be taken to avoid under or over-fitting the flow profile, and hence the effects of the filter parameters on the WSR estimation accuracy were investigated, in terms of the polynomial order and the window size.

Because non-slip boundary condition was applied to estimate the velocity gradient, accurate identification of the vessel wall is essential. In the experimental study, a localised region-based active contour segmentation algorithm [187] was implemented to dynamically track the vessel wall prior to the velocity estimation. It is a robust and accurate technique which uses local image statistics to evolve a contour for object segmentation. However, such segmentation is not applied in our steady flow simulation study as a more controlled way to evaluate the sensitivity of the developed technique with respect to the possible errors due to inaccurate wall tracking. The wall positions were deliberately deviated from the ground truth positions in the steady flow simulation study

By assuming the working fluid is a Newtonian fluid, WSS can be determined from the shear rate tensor as follows:

$$\tau_w = \mu \varepsilon'_{12} \quad 4-1$$

where μ is the dynamic viscosity and ε'_{12} is the tangential component of the shear rate tensor defined in Eq 4-3. To account for any misalignment between the image coordinate and the coordinate along the wall, the shear rate tensor was computed by transforming the original strain rate tensor in the 2-dimensional Cartesian coordinate to the wall-oriented coordinate system [188], [189], written as

$$\varepsilon'_{mn} = \sum_{i=1}^2 \sum_{j=1}^2 C_{im} C_{jn} \varepsilon_{ij} \quad 4-2$$

where ε_{ij} is the original strain tensor in the image Cartesian coordinate defined as

$$\varepsilon_{ij} = \left[\frac{\partial u_i}{\partial x_j} + \frac{\partial u_j}{\partial x_i} \right] \quad 4-3$$

And C_{ij} is the 2D rotation transformation matrix, defined for each point along the wall in terms of the rotation angle θ between the original and wall-oriented coordinate, as follows

$$C_{ij} = \begin{bmatrix} \cos \theta & -\sin \theta \\ \sin \theta & \cos \theta \end{bmatrix} \quad 4-4$$

4.2.2 Ultrasound flow simulation

To evaluate the accuracy of WSR estimation, synthetic ultrasound images for a 6mm in diameter tube were generated using the analytical solution and the Field II ultrasound simulator as described in Chapter 4. Poiseuille flow with centreline velocity of 50cm/s, $Re=1500$ and WSR of $333s^{-1}$ was generated to investigate the effects of the SG-filter parameters on WSR estimation. The same set of data was also used to evaluate the sensitivity of the WSR estimation with respect to the possible errors in wall tracking.

In addition to the steady flow simulations, Womersley flows were also generated to evaluate the performance of our system to provide accurate WSR measurement in pulsatile flow. The reference WSR profile was derived from the ground truth velocity profile and compared to the estimated WSR.

4.2.3 In-vitro flow experiments

To illustrate the capability of our system to estimate WSS in a physiologically relevant environment, WSRs were measured on two anthropomorphic bifurcation phantoms. These data have been collected in Chapter 4 and reanalysed in this section. To recap, the phantoms are fabricated with polyvinyl alcohol cryogel as the tissue-mimicking material, containing three vessel branches, mimicking a carotid bifurcation junction of the common carotid artery (CCA), internal carotid artery (ICA) and external carotid artery (ECA). The design protocol and the phantom properties can be found in [147], [162].

A realistic pulsatile flow with 2mL/s average flow rate and 4mL/s systolic flow rate was generated using a pulsatile pump (Harvard Apparatus 1405 pulsatile blood pump), circulating fluid comprised BMF solution[148] (90% pure water and 10% glycerol, density $\rho=1037 \text{ kgm}^{-3}$, dynamic viscosity $\mu= 4.1 \text{ mPa s}$) and diluted homemade microbubbles (5×10^9 micobubbles/mL) at 60pulses/min pulse rate.

4.2.4 WSR Assessment

To evaluate the estimated WSR accuracy, mean error (ME) and the normalised root mean square error (NRMSE) were computed from a single spatial location x on the wall as follow.

$$ME = \frac{\int_0^t WSR(t) dt - \int_0^t WSR_t(t) dt}{\int_0^\infty WSR_t(t) dt} \times 100\% \quad 4-5$$

$$NRMSE = \frac{1}{WSR_{t(\max)}} \sqrt{\frac{\sum_{t=1}^n (WSR - WSR_t)^2}{n}} \times 100\% \quad 4-6$$

Where WSR and WSR_t are the measured and the reference WSR waveform, $WSR_{t(\max)}$ is the maximum referenced WSR value, and n is the number of time samples. Note that the errors are calculated over a cycle period for the pulsatile flow condition and over 20 frames for the steady flow condition.

4.3 Results

4.3.1 Ultrasound flow simulation

4.3.1.1 Sensible filter parameters

With the known vessel wall location, simulated images were segmented and subsequently estimated using the UIV algorithm. The 2D velocity mapping, averaged velocity profile and shear rate profile are illustrated in Figure 4.1. Consistent parabolic profiles represented by colour-coded velocity vectors can be seen across the straight vessel. From the quantification, ME of $-1.61 \pm 0.92\%$ or NRMSE of $2.37 \pm 0.02\%$ was found when comparing the estimated velocity profile to the analytical velocity profile. Despite the highly accurate velocity measurement, a small fluctuation in the velocity profile may affect the WSR estimation (Figure 4.1b-c) as shear rate was estimated from the velocity gradient. To alleviate such errors, a SG filter which fit a sub-set of the near wall velocity profile with a low degree polynomial by methods of linear least squares method, was used to spatially smooth the velocity profile prior to the shear rate estimation to attain a more robust WSR measurement.

However, the selection of the polynomial order and filter length may affect the filtering results.

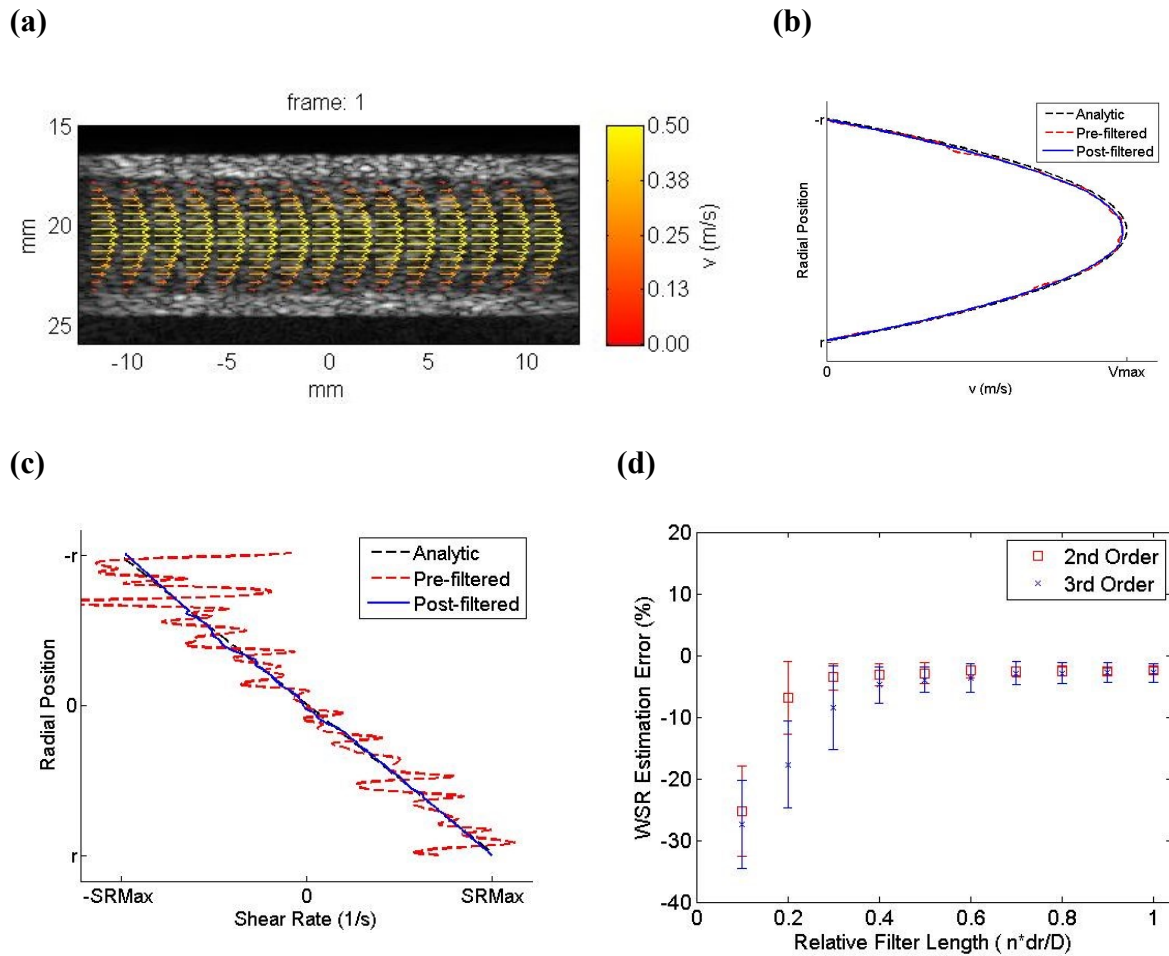


Figure 4.1: (a) Vector velocity mapping derived from the simulated steady flow. (b-c) Comparison of the analytical ground truth with the pre- and post- Sovitzky-golay (SV) filter velocity profile and shear rate estimation. (d) Effects of filter length relative to the diameter of the tube and the filter order toward the WSR estimation error. n =filter length, dr =image resolution, D =vessel radial diameter

To optimise the filter settings, the effects of the filter length and the polynomial order were investigated (Figure 4.1d). It should be noted that only 2nd and 3rd order filter were investigated as higher order polynomials are generally less robust and sensitive to small-amplitude and random distributed error[190]. The findings in Figure 4.1(d) suggest that increasing the filter length relative to the diameter of the vessel produced less error with

smaller variance; however, it may intrinsically restrict the flow profile to certain polynomial shape depending on the polynomial order selected and forces the velocity profile to comply more to the velocity profile in the region further away from the wall than to the profile near the wall. Hence, filter parameters were chosen such that the mean estimation error and variance are less than 10%, and in the later study, a 2nd order 0.2D filter resulting in 6.87 +5.83% error (D=vessel radial diameter) and a 3rd order 0.3D filter which yields 8.56 +6.75% error were implemented.

4.3.1.2 Sensitivity to the wall positions

Using the optimised filter parameters, the WSR estimation error as a function of estimated wall position relative to the ground truth wall position is illustrated in Figure 4.2(a). Regardless of the filter order, wall shear rates were overestimated when the wall positions were incorrectly localized within the vessel and underestimated when the wall positions were incorrectly localized outside the vessel away from the ground truth wall position. Figure 4.2(b) plots the shear rate profile corresponding to the different wall locations identified. The wall shear rate, estimated at both end of the shear rate profile, deviated from ground truth profile by up to 60% when an inaccurate wall position of 200um was identified. Such errors can be explained by the low-pass spatial filtering effect of the correlation technique[95] and the non-slip boundary condition which impose a zero velocity at the identified boundary.

(a)

(b)

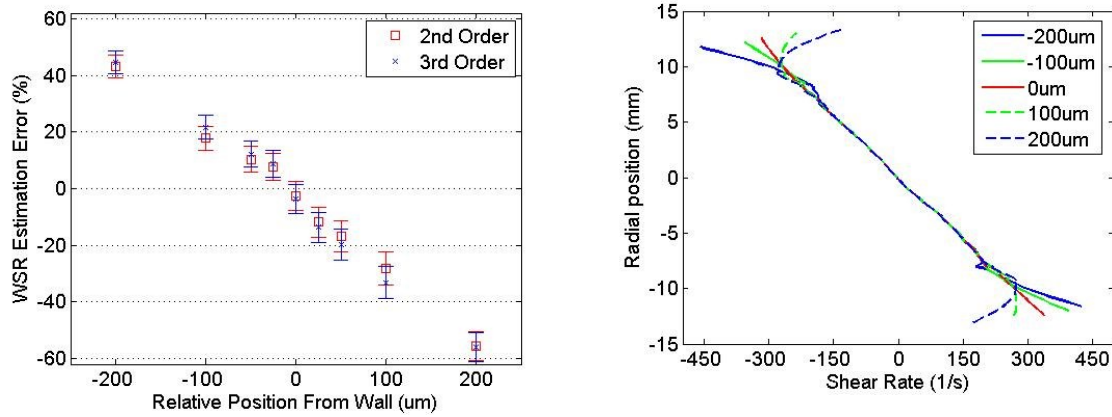


Figure 4.2: (a) Effect of estimated wall location error toward the WSR estimation error. (b) Shear rate profile corresponding to different wall locations which deviate from the ground truth location.

4.3.1.3 WSR measurement on the realistic flow simulation

With our developed technique, the wall shear rates were estimated from the velocity profile acquired from the simulated CCA and CFA. Temporal snapshots of the WSR mapping overlaid on the velocity vector images at different phase of a cardiac cycle are presented in Figure 4.3. The magnitude of the WSR varied according to the near wall flow velocity while the direction of the near wall flow velocity determined the direction in the WSR. Although consistent WSR distributions were expected along the inner wall of the straight tube, slight discrepancies can be observed near the left and right edges of the vessel. This is likely due to two reasons: first, the decreased spatial resolution there in a compounded plane wave imaging; second, the over smoothing of the flow field when in-plane motion moves out of the field of view occurs.

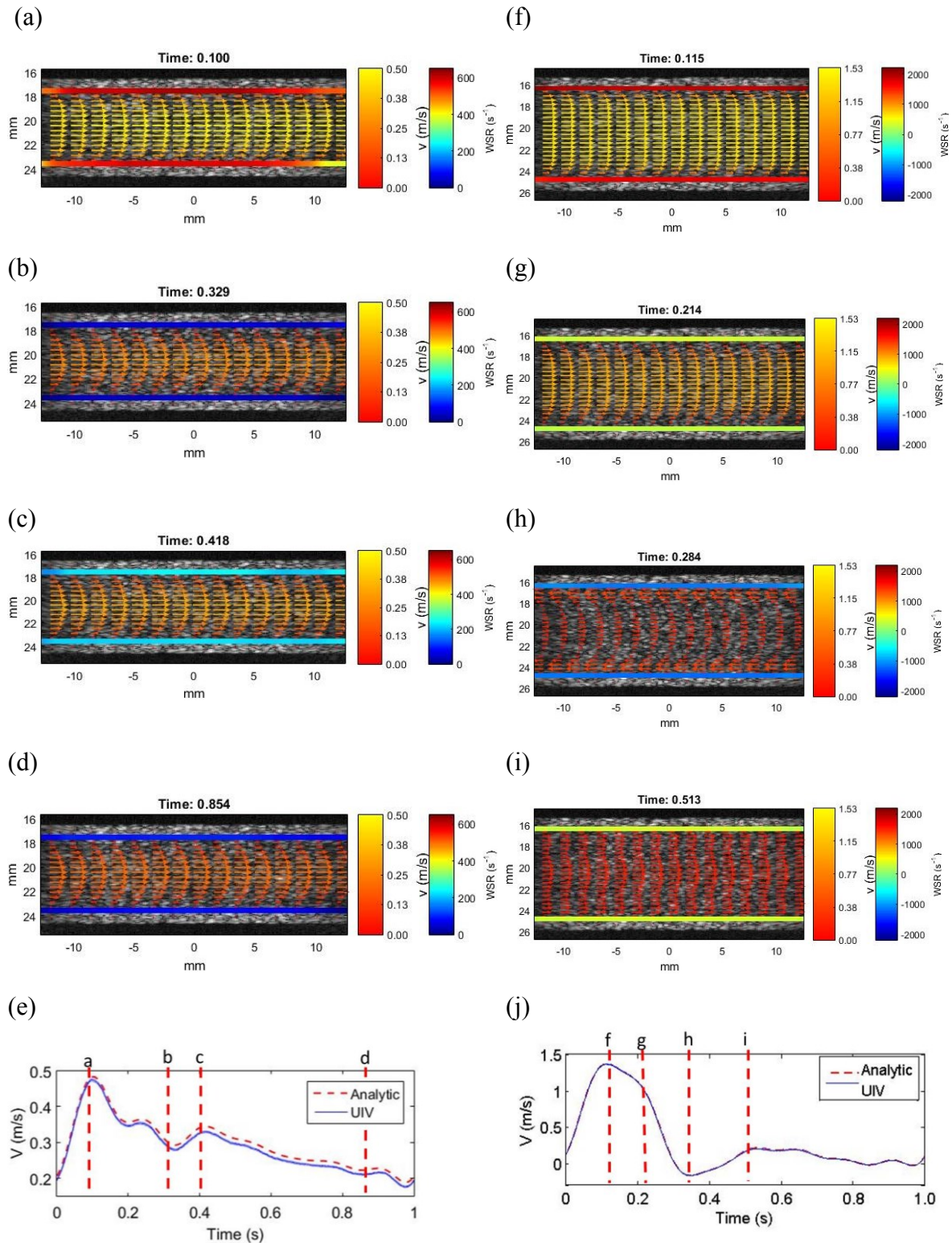


Figure 4.3: Quantitative measurements of the ultrasound imaging velocimetry (UIV) obtained at four different cardiac phases highlight the key flow patterns and wall shear rate distributions in (a-d) common carotid artery (CCA), (f-i) a common femoral artery (CFA). The centreline velocity of the (e) CCA and CFA are overlaid on the ground truth solution and the relative time of each flow pattern is marked in the centreline velocity plot. Note that the shading in UIV measurement in (e)&(j) represents the standard deviation.

To quantify the WSR estimation error, the spatial-average WSR in the CCA and CFA are illustrated in Figure 4.4. Only the upper WSR was demonstrated as the shear rate profile is axisymmetric. The estimated spatial average WSR showed good agreement with the analytical WSR with minor shift, and the estimation errors were summarised in Table 4.1.

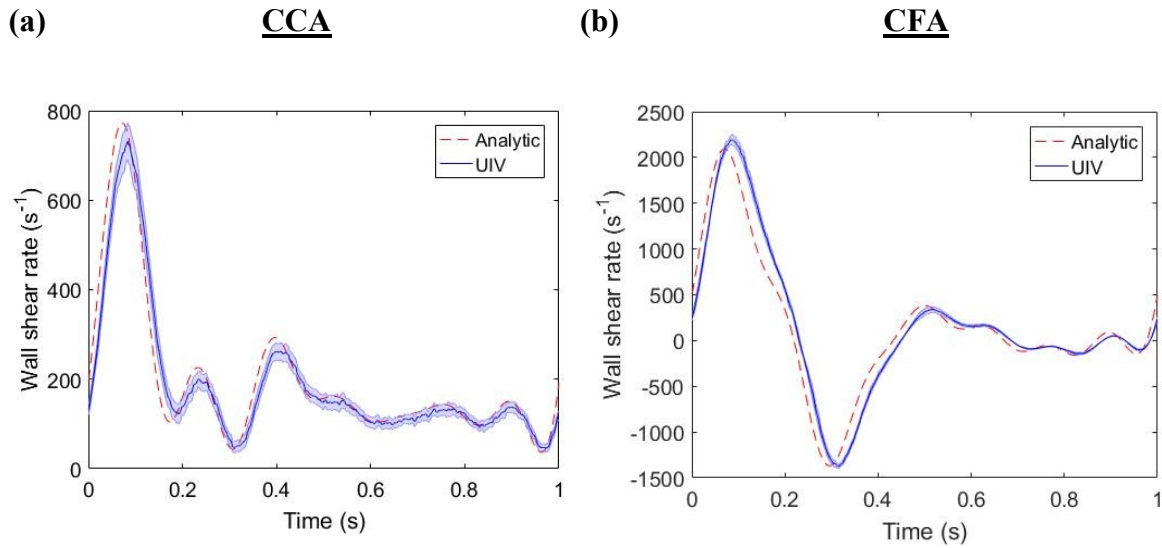


Figure 4.4: Spatial-averaged WSR estimation overlay on the analytical solution derived from the ground truth in (a) common carotid artery (CCA); (b) common femoral artery (CFA).

Table 4.1: Error analysis on the estimated wall shear rate

Error measures	CCA		CFA	
	Upper wall	Lower Wall	Upper wall	Lower Wall
ME (%)	-4.78±7.96	-13.97±8.45	5.71±2.12	0.64±3.05
NRMSE (%)	1.62±1.74	3.73±2.47	0.92±0.31	0.39±0.36

4.3.2 In-vitro WSR measurements

To highlight the spatiotemporally varying WSS distribution induced by the two different carotid models, temporal snapshots of the WSS distribution overlaid on the vector flow images acquired at 4 different phases are shown in Figure 4.5. In the healthy carotid phantom, high WSS, up to 10 Pa, was observed throughout the carotid bifurcation phantom except at the ICA bulb where a relatively low velocity and WSR was observed (Figure 4.5a). This low WSS area was clearly seen immediately after the peak systole when flow separated near the ICA sinus causing a flow reversal and a negative WSS near the carotid bulb (Figure 4.5). In addition, it was also noted that at the inner wall of the proximal ICA and ECA (where the branching is located), a relatively high WSS was observed due to the forward streamline flow during the systole phase. However, during the diastole phase, the flow moved relatively slowly within the vessel and a lower WSR was expected (Figure 4.5c-d).

Because flow velocity and WSS are inter-related, elevated WSS appeared at the stenosis throat in a diseased carotid phantom and continues along the inner wall of ICA where the jet flow forms (Figure 4.5f-g). Such elevated WSS was also observed further downstream in the ICA where the jet impinges on the outer wall. In contrast to the wall areas where the jet travelled, the wall regions where the separations are located were constantly exhibited a low WSS. Such findings agree with those observed in [191], [192].

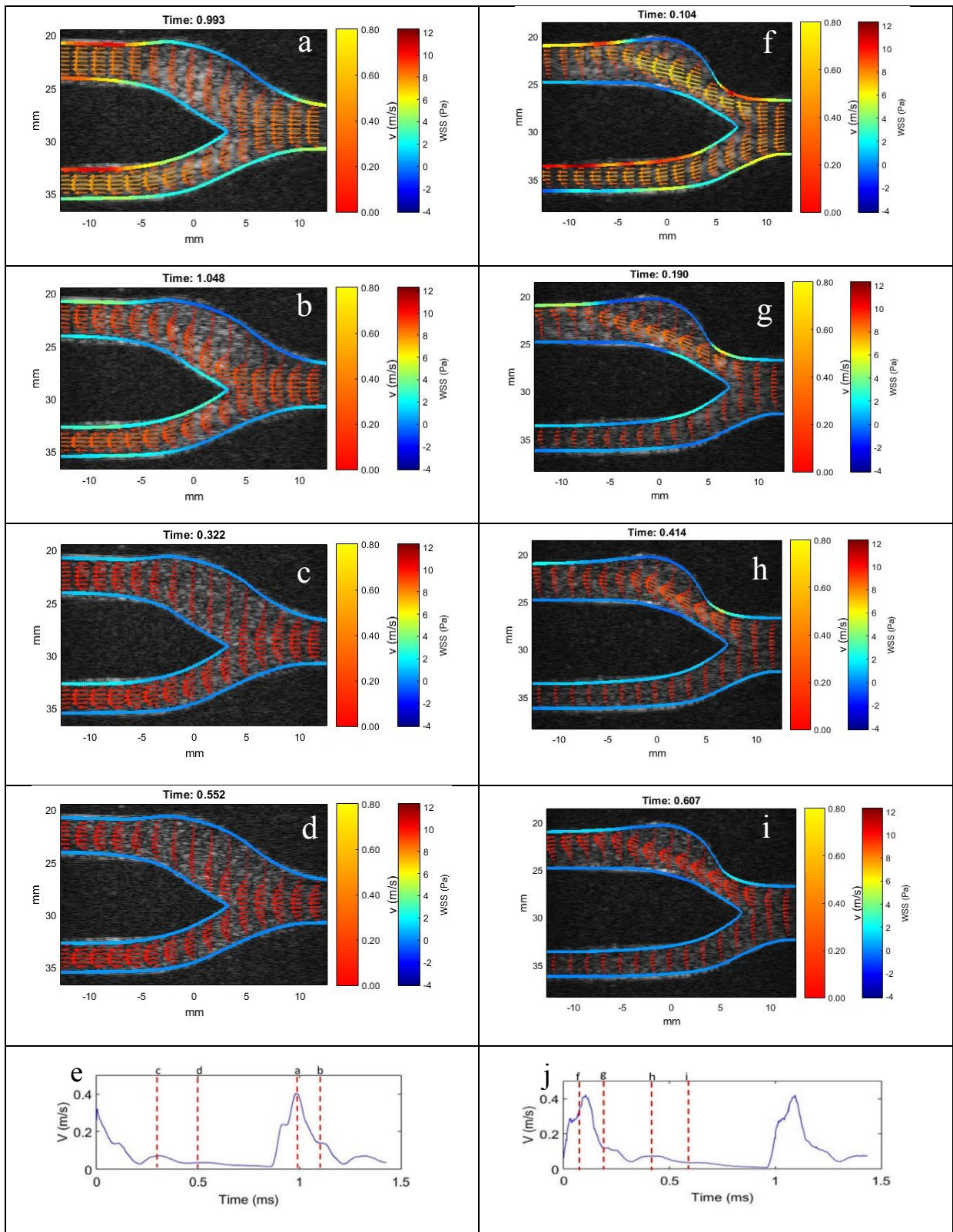


Figure 4.5: Key quantitative measurements derived from ultrasound imaging velocimetry (UIV) to highlight the spatio-temporal varying wall shear stress (WSS) distribution in (a-d) a healthy carotid bifurcation phantom; (f-i) a diseased carotid bifurcation phantom with 50% eccentric stenosis. (e,j) Inlet centreline velocity extracted from the common carotid artery in both carotid models. The relative times when the images are acquired is marked in the velocity plot.

4.4 Discussion

In this study, we have presented a methodology to quantify spatio-temporal WSS based on the high frame rate UIV system we have developed for quantifying arterial flow. Initial evaluations on the synthetic ultrasound images with ground truth known and the in vitro studies on healthy and diseased carotid phantoms have demonstrated the feasibility of the developed system to provide WSS distribution in addition to 2D flow velocity measurements.

Despite the high accuracy of the velocity mapping, accurate measurement of the wall shear rate is not an easy task. WSR is derived from the velocity gradient near the wall; therefore slight changes in the velocity gradient or the wall position will affect the estimation. To mitigate the former problem, a SG-filter has been applied to smooth the velocity profile before estimating the WSR. This filter has been shown to effectively reduce the uncertainties in WSR measurement (Figure 4.1). Note that a careful selection of the filter's order and window size is needed to avoid the under or over-fitting estimation similar to those where interpolation or extrapolation methods were used to approximate WSR [193]. From Figure 4.3 and Figure 4.4, it can be clearly seen that the selected filter parameters were able to produce accurate and robust WSR measurements across the full FOV both spatially and temporally.

While consistent measurement can be realised with the filtering, a more stringent identification of the wall position is needed to accurately estimate the WSR. Significant impact to the WSR estimation can occur due to the errors in wall tracking as illustrated in Figure 4.2. An error within a spatial resolution (200 μ m) may yield a WSR estimation error up to 60%. To ensure accurate WSR measurements, sub-pixel wall segmentation up to 50 μ m is required. However, it should be noted that such sensitivity is not a specific weakness of our proposed technique, but is inherent from the direct WSR measurement technique and also affects others imaging modalities with limited spatial resolution[184], [194]. Our technique

which combined the plane wave ultrasound imaging with contrast imaging may well help to maximise the accuracy in locating the wall up to sub-wavelength limit. The microbubble contrast agents not only enhance the signal within the blood pool and increase the ultrasound imaging sensitivity, but they also enable a higher specificity between vessel wall and flow region when coupled with a contrast specific imaging sequence. This therefore allows a better wall segmentation while plane wave imaging retains a high temporal resolution for wall tracking and velocity measurement.

The capabilities of our system to quantitatively visualise the WSS distribution and complex flow patterns within two physiologically relevant carotid phantoms were demonstrated *in-vitro*. The post-processing steps including as the automatic wall segmentation, velocity estimation, and regulating velocity using SG-filter before WSR filtering, were kept the same for the investigation of synthetic images (pulsatile cases) and in-vitro imaging data. Our results match qualitatively with those optical PIV measurements demonstrated by Kefayati [191] on a transparent and rigid carotid bifurcation model. However, a lower WSS magnitude was quantified. This discrepancy can be attributed to several factors such as the difference in the flow rates or fluid viscosity, uncertainties in the wall location, out-of-plane motion, as well as the compliance of the model. Despite this, the relative differences between the WSS distribution of a healthy and disease carotid geometry were clearly observed in Figure 4.5.

As with our previous study, a potential limitation in evaluating the accuracy of the WSS is the usage of the rigid tube simulation and the linear wave ultrasound simulator (Field II). However, it should be noted that the simulation of contrast pulse sequence and response are not impossible and can be done by adapting the Creanuis nonlinear wave simulator [179]. A more complex geometry such as the carotid bifurcation model simulated by Swillen [178] can also be adapted to provide a more realistic simulation that includes the wall deformation, out of plane motion, and high dynamic flow patterns which have not been taken into account in

our current simulation. Such a simulation has been shown in [195] to generate synthetic data which mimic the physical properties of a human carotid bifurcation. The realistic blood flow and wall movement can be obtained through a fluid structure interaction (FSI) modelling, and the specular reflections signal at the lumen wall can be simulated by altering the scatterer density at the vessel wall and the wall surrounding tissue transition regions.

Apart from the refinement that can be done in simulation, limitations of using 2D imaging to estimate velocity and WSR also need to be addressed. With 2D imaging, only the in-plane motion was tracked and considered when determining the accuracy of our system. However, the out-of-plane motion may also affect the accuracy of wall velocity and shear rate measurement and therefore needs to be further investigated. For example, although a controlled flow rate was applied in the experiment, secondary flow and turbulence may arise due to the local tortuosity of the bifurcation model and cause an error in the WSS estimation. In spite of this, the plane wave UIV is still capable of capturing the in-plane velocity and WSS distribution to show the relative difference between a healthy and diseased carotid geometry.

High frame rate plane wave UIV is a non-invasive technique capable of evaluating both velocity and WSS simultaneously. This can be potentially used in a wide range of clinical applications. For instances, the technique could help to predict atherosclerotic lesions, assess risk of thrombosis and provide insight into the pathogenesis of various vascular diseases to guide clinical decision. It can also be used to predict the risk of angiographic restenosis after coronary and peripheral angioplasty and improve surgical technique related to coronary artery bypass graft.

4.5 Conclusion

In this study, plane wave UIV system which provides both flow velocity vectors and wall shear stress mapping simultaneously has been developed and evaluated. Initial simulation studies have demonstrated the capabilities of our technique to provide accurate spatio-temporally varying velocity and WSS estimation. *In-vitro* experiments have demonstrated the potential of this technique for vascular application *in-vivo*.

Chapter 5 - Microbubbles void imaging

In this study, preliminary work is reported on a novel non-invasive technique, microbubble void imaging, which is based on ultrasound and controlled destruction of microbubble contrast agents, permitting flow visualisation and quantification of flow-induced mixing in large vessels. The generation of microbubble voids can be controlled both spatially and temporally using ultrasound parameters within the safety limits. Three different model vessel geometries, straight, planar-curved and helical, with known effects on the flow field and mixing were chosen to evaluate the technique. A high frame-rate ultrasound system with plane wave transmission was used to acquire the contrast enhanced ultrasound images and an entropy measure was calculated to quantify mixing. The experimental results were cross-compared between the different geometries and with Computational Fluid Dynamics (CFD). The results show that the technique is able to quantify the degree of mixing within the different configurations, with a helical geometry generating the greatest mixing, and a straight geometry the lowest. There is a high level of concordance between the CFD and experimental results. The technique could also serve as a flow visualisation tool.

This work was in collaboration with a group of people from Department of Bioengineering, Department of Aeronautics and Imperial College Renal and Transplant Centre, and resulted in a publication [196]. Mr Francesco Iori has contributed to the CFD simulation and implementation of the analysis algorithm, Mr Richard Corbett helped in the implementation of the experimental setup, and I was responsible for the experimental data acquisition and data processing. The method was devised by Dr Meng-Xing Tang, Professor Colin Caro and Dr. Peter Vincent, and this part of the results is reproduced here with permission.

5.1 Introduction

Cardiovascular disease is strongly correlated with blood flow dynamics. There is increasing recognition of the influence of the flow field on the normal functioning of vessels and their development of pathology [4], [8], [122], [197], [198]. Moreover, the flow field can be expected to play a role in the management of vascular pathology [199], [200]. Several groups have characterised arterial geometry and attempted to infer its influence on the flow [6], [12], [205]–[207]. Non-planar curvature, in-plane swirling and intraluminal mixing appear commonly in normal arteries [204] and may be of importance in interventions, including bypass grafts and arterial stents [5], [205], [210]–[212]. However, readily applicable methods have been lacking for imaging the flow and quantifying mixing. A novel method is proposed – void imaging - based on the controlled destruction of ultrasound microbubbles.

Existing imaging techniques can be used for flow visualisation in vivo. These techniques, including Magnetic Resonance Imaging (MRI), Computed Tomography (CT) and Digital Subtraction Angiography (DSA), typically require local injection of a contrast agent or indicator, which is subsequently tracked over space and time. While these techniques can provide high anatomical and geometric resolution, they still have limitations in terms of rapid and contemporaneous assessment of three-dimensional geometry and flow. The injection site must be upstream of the vessel of interest. The procedure can be highly invasive and the injection of contrast medium can be difficult to control, precluding quantitative assessment of mixing. Furthermore there is local disturbance of the flow field arising from the injection, while the physical properties of the contrast agent may render it an unfaithful flow indicator. In addition, CT and DSA involve the use of ionising radiation. Although some MRI techniques such as arterial spin labelling can track flow without contrast injection, they suffer from poor signal to noise ratio [208] and currently are used predominantly to assess tissue perfusion.

An alternative approach is to image vascular geometries, using modalities which are then combined with computational fluid dynamics to achieve flow visualisation and quantification[209]. This approach depends highly on the fidelity of the geometry obtained from the imaging data and also on the accuracy of boundary conditions.

Various ultrasound imaging techniques, including B-flow imaging [210], [211] can provide both the vascular geometry and flow visualisation [212]. However, the signal to noise ratio of B-flow imaging is limited by the weak ultrasound scattering of blood cells and can become even less reliable in imaging deeper structures, where a lower ultrasound frequency is required.

Contrast enhanced ultrasound (CEUS) with microbubble contrast agents, consisting of a gas core encapsulated within a lipid or albumin shell and with typical sizes between 1 and 7 microns, have been widely used in clinical applications for improved imaging of flow and assessment of perfusion [217]–[219]. They have also shown great potential for molecular imaging and therapy [55], [216], including enhancement of mass transport across endothelium. Under low acoustic pressure, microbubble contrast agents are able to significantly enhance the ultrasound signal from within blood vessels without disturbing the flow. This has been combined with particle/speckle tracking algorithms (known as Ultrasound Imaging Velocimetry (UIV) or echo-Particle Image Velocimetry (e-PIV)), to quantitatively map the flow field in vessels where light cannot penetrate [100], [120].

While the above techniques are capable of visualising flow and quantifying the velocity derived parameters, experimental quantification of intraluminal mixing in vivo has not yet been reported; existing studies of mixing have mainly been undertaken using numerical models[217]. Quantification of intraluminal mixing remains nevertheless desirable given its

relationship to conduit geometry, the flow field (including its stability and pulsatility), wall shear and fluid-wall mass transport [5], [200], [218].

Secondary motion can markedly influence intraluminal mixing in larger vessels and their normal or disturbed physiology. It is important therefore to distinguish the contributions of advection (bulk flow) and diffusion. In determining the contribution of advection, it is desirable that a contrast agent should have a low diffusivity, so that mixing results predominantly from advection. This situation is represented by a high Peclet (Pe) number (a dimensionless quantity representing the relative rates of advection and diffusion).

Microbubbles, because of their micrometre size relative to water molecules (nanometre size scale) will have a very low diffusivity in water and blood. In a dilute suspension, as in this work, and from the Stokes-Einstein law, a typical bubble with a radius of $3.0 \times 10^{-6} \text{ m}$ has a diffusion coefficient $D = 7.6 \times 10^{-14} \text{ m}^2 \text{ s}^{-1}$ and a Peclet number $Pe = 3.5 \times 10^9$ at physiological flow rates and scales involved in this study. Consequently, any mixing will dominantly be as the result of advection rather than diffusion and any further discussion of mixing in relation to microbubbles will relate to advective mixing. The low diffusivity of microbubbles renders them highly suited for use as contrast agents for assessing advective mixing.

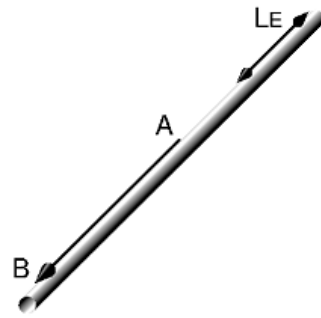
A unique property of microbubble contrast agents is that at higher acoustic pressures they can be disrupted in a highly controlled way both spatially and temporally, i.e. bubbles can be “switched off” at will. In clinical practice this property is widely employed in the so called “destruction-replenishment” mode to quantify tissue perfusion [59], [219], using ultrasound amplitudes within clinical safety limits. This offers the opportunity to “inject” a volume void of microbubbles non-invasively and essentially instantaneously, by increasing ultrasound amplitude in the region of interest and observing the evolution of such a bubble void in vascular space over time.

In this study we investigate a novel method to visualise flow and quantify mixing in large vessels, making use of controlled microbubble destruction and high frame-rate ultrasound. An in vitro experiment has been performed on three different vascular geometries and results are compared with numerical CFD solutions.

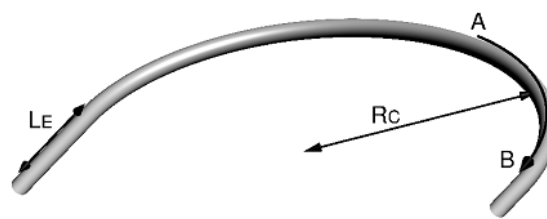
5.2 Methods

5.2.1 Experimental flow set up

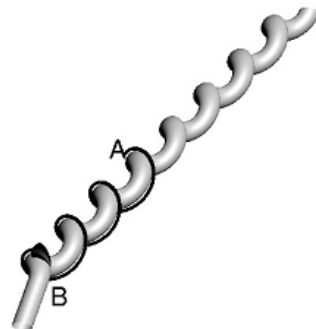
Vessel mimicking phantoms of three geometries, straight, planar-curved and helical, were constructed from rubber latex tubing (Primeline Industries, Ohio, USA) with an internal diameter (D_i) of 0.006m. Figure 5.1 shows diagrammatically the three vessel geometries. Location A in Figure 1 refers to the location of a single element transducer 3.5×10^{-2} m in diameter used for microbubble destruction, i.e. the location of the void indicator “injection”. 0.2m downstream is the imaging plane (location B), with the respective location markers representing the central lines of the two transducers.



(a) Straight



(b) Planar curve



(c) Helix

Figure 5.1: Three geometries used as phantoms: L_E - entrance length, R_C – radius of curvature, A- location of microbubble destruction transducer, B- location of detection transducer, AB- path taken by microbubble void prior to detection and direction of flow

All phantoms were submerged (approximately 0.03m) in a water tank filled with degassed water. The surfaces of the transducers were submerged (approximately 0.01m) in the water bath directly above the tubing at locations A and B. The straight phantom (Figure 5.1a), consisted of a straight tube of 0.4m length with an entrance section of length 0.09m (L_E) to ensure established Poiseuille flow[220]. A void was created in the tubing directly underneath

the upstream transducer (A) and after the distance travelled by the void (AB), images were acquired with the detection transducer downstream (B). The curved phantom (Figure 5.1b) consisted of a straight entrance section of length 0.09m, before the flow entered a planar curve of arc length π rad, with a radius (R_c) of 0.16m. The detection transducer was located at B, on the straight tube after the exit of the curve and parallel to the entrance length while the void creation occurred 0.2m upstream at A. For the helical phantom (Figure 5.1c), a helix with radius (R_h) $0.5D_i$ and pitch (P_h) of $7D_i$ was used with a total of 10 complete revolutions preceded by a straight entrance section of length 0.09m (not shown in figure). B lay at the straight tube immediate after the exit of the helix to allow placement of the transducer.

Steady flow was generated by an elevated reservoir tank upstream of the phantom. Microbubbles (detailed below) were added to the header tank (0.1ml into 5 litres of gas saturated water). Bulk flow was measured and controlled by a rotational flow meter on the outflow arm of the circuit. The phantoms were submerged in a large tank of water to facilitate ultrasound imaging. The straight and curved phantoms were placed in a plane orthogonal to gravity along with the centreline of the helical phantom. The conformation of the phantoms was maintained for the curved phantom by the use of a supporting large diameter external rigid polyvinyl chloride tube, with apertures cut for the transducers and thermoset to the appropriate geometry. In the helical case a custom-made steel mandrel was used. All work was performed at a constant room temperature (22°C).

For all experiments mean velocity (u_i) was set at 0.044m s^{-1} . The dynamic viscosity of water μ and the density of water ρ were respectively taken to be $9.55 \times 10^{-4} \text{ Pa s}$ and 997.86 kg m^{-3} .

The inflow Reynolds number (Re) defined as:

$$Re = \frac{u_i D_i \rho}{\mu} \quad 5-1$$

was 275, a physiologically relevant value for a peripheral artery. Furthermore, for the curved vessel the Dean number (De) defined as,

$$De = Re \sqrt{\frac{D_i}{2 R_c}} \quad 5-2$$

was 37, which is also physiologically relevant.

5.2.2 Microbubble contrast agent

Using the formulation outlined by Sheeran[140] decafluorobutane microbubbles were prepared by the dissolution of 1,2-dipalmitoyl-sn-glycero 3-phosphatidylcholine(DPPC), 1,2-dipalmitoyl-sn-glycero-3-phosphatidylethanolamine-polyethyleneglycol-2000(DPPE-PEG-2000), and 1,2-dipalmitoyl-3-trimethylammonium propanoate (chloride salt; 16:0 TAP) in a molar ratio of 65:5:30 and a total lipid concentration of 0.75mg/mL, 1.5mg/mL, and 3mg/mL. The excipient solution comprised propylene 15% glycol, 5 % glycerol and 80% normal saline. Microbubbles were then generated via agitation of a 2mL seal vial containing 1.5mL of the resulting solution using a shaker for 60 seconds.

The microbubble solution generated was sized and counted according to [141] and had a concentration of about 5×10^9 microbubbles/mL with the average size at 1 micron. In this study, microbubbles were diluted in out-gassed water [142] to a concentration of 2×10^5 microbubbles/mL.

5.2.3 Void creation by bubble destruction

In the present study, microbubbles disruption at high ultrasound pressure was harnessed as a technique for injecting a negative indicator by creating a microbubble void within a microbubble filled vessel.. A long burst of 5000 cycles at 2MHz and a peak-negative pressure of 1.3MPa was transmitted from the single element unfocussed transducer to destroy the

microbubbles within the intersection volume between the ultrasound field and the vessel lumen. This level of ultrasound transmission is well within the FDA safety limit [221].

5.2.4 Ultrasound imaging

A L12-5 50mm linear array transducer mounted on a Verasonics Vantage 128 research platform (Verasonics Inc, Redmond, WA, United State) was placed perpendicular to the local centreline of the phantom to image the cross-sectional flow field. The Verasonics system was programmed to send out plane waves of inverted phase which are capable of specifically detecting microbubbles with high frame rate [62] and avoiding potential issues with traditional line-by-line scanning [120].

16 plane waves with angles spanning -18 to 18 degrees were transmitted at 100Hz to form an image after coherent compounding. For each pulse sequence, the broadband transducer was driven to transmit repetitively a 5MHz 1 cycle imaging pulse followed by its phase inverted counterpart while the radio frequency (RF) echoes were received at a centre frequency of 7.8MHz and accumulated in the local memory. The RF data collected were then transferred back to a computer through a high speed PCI-Express connection, software beam formed into a series of CEUS images and further analysed using Matlab.

5.2.5 Ultrasound image enhancement

Before quantifying the mixing, CEUS images were processed as shown in Figure 5.2 to enhance the image quality. The region of interest containing the cross-section of the tube was first selected from temporal snapshots and cropped using a circular mask. The regions of interest were then processed using proper orthogonal decomposition (POD) to enhance the visibility of the coherent structures that vary in space and time depending on flow geometry [222], [223]. In summary, the images were decomposed into a finite number of proper orthogonal modes by determination of eigenfunctions using Methods of Snapshots [224] and

reconstructed with the first N most energetic modes to capture the dominant structure. In this process, incoherent speckle and noise were removed and the coherent bubble response and microbubble void were emphasized. To further enhance the image, the contrast of the reconstructed images were enhanced by transforming the grayscale intensity using a sigmoid function.

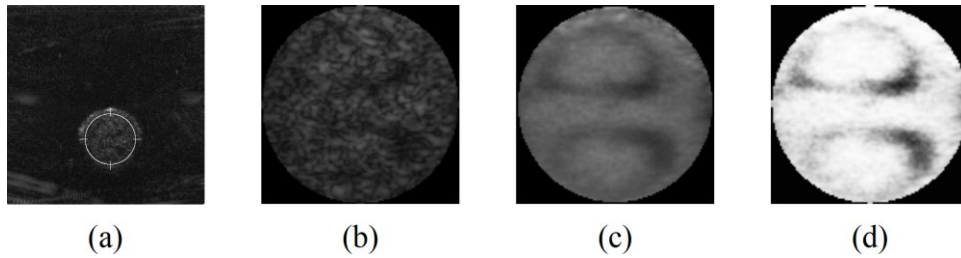


Figure 5.2: Illustration of the contrast enhancing filter used on data from a planar bend (a) raw data; (b) region of interest cropped from raw data; (c) Snapshot POD is calculated and the image is reconstructed using the first n modes; (d) Contrast is enhanced using a sigmoid function

5.2.6 Computational fluid dynamics

5.2.6.1 Geometries

Geometries matching the experimental setup shown in Figure 5.1 were used in all the CFD simulations. In all cases, $Re = 275$ and for the curved configuration $De = 37$ was used, indicating that the flow is fully laminar. A 0.006m diameter void (zero bubble concentration) was inserted 0.02m away from the flow outlet and the cross-sectional flow patterns were observed at the flow outlet.

5.2.6.2 Governing Equations

Flow

Water was treated as an incompressible Newtonian fluid. Specifically, flow was modelled using the steady incompressible Navier-Stokes equations for a fluid with a constant viscosity, which can be written as:

$$\nabla \cdot \mathbf{u} = 0 \quad 5-3$$

$$(\mathbf{u} \cdot \nabla)\mathbf{u} = -\frac{1}{\rho} \nabla p + \frac{\mu}{\rho} \nabla^2 \mathbf{u} \quad 5-4$$

here μ is the viscosity of water, ρ is the density of water, \mathbf{u} is the three-dimensional velocity (vector) field, and p is the pressure field. The values of μ and ρ were chosen to match the *in-vitro* experiment, resulting in identical Re and De numbers as above.

Microbubbles

Microbubbles were treated as a continuum species dissolved in water rather than a discrete phase. Specifically, microbubble transport was modelled using the time-dependent advection equation for a passive scalar, which can be written as:

$$\frac{dc}{dt} = -\mathbf{u} \cdot \nabla c \quad 5-5$$

where \mathbf{u} is the three-dimensional velocity (vector) field, and c is the non-dimensional microbubble concentration. Use of the advection equation to model microbubble transport is justified in this instance given the very large Peclet number.

5.2.6.3 Boundary Condition

Flow

A steady-state constant boundary-normal parabolic flow profile with a spatially averaged velocity $u_i = 0.044 \text{ m s}^{-1}$ (equivalent to 1.3 ml.s^{-1}) was applied at the inlet in all models. A

constant (and arbitrary) pressure was applied at each outlet. A no-slip condition was applied at the walls, which were assumed to be rigid.

Microbubbles

For each configuration, a steady state constant concentration of 1.0 was applied at the inlet, and a no-stress boundary condition was applied at the outlet. A zero-flux boundary condition was applied at the walls, modelling the walls as impermeable to microbubbles.

5.2.6.4 Initial Condition

Flow

For each configuration the flow solver was initialised with a zero-velocity and zero-pressure field.

Microbubbles

The initial microbubble concentration field had a value of 1.0 everywhere, except for the region of microbubble destruction where a value of 0 was imposed. A smooth transition between the two regions was applied to take into account the ultrasound beam pressure profile. Specifically, the measured beam pressure profile was fitted to a double logistic step function $\hat{\sigma}(x)$ using a Least-Square Method to minimize error between the fit and the measured values. The generic logistic function $\sigma(x)$ is defined as:

$$\sigma(x) = \frac{1}{1 + e^{-bx}} \quad 5-6$$

while the double logistic step function:

$$\hat{\sigma}(x) = a[\sigma(x - x_s) - \sigma(x - x_e)] \quad 5-7$$

where a , x_s , x_e , and b parameterise $\hat{\sigma}(x)$. Table 5.1 shows the values of these parameters estimated using a Least-Square method.

Table 5.1: Estimated set of parameters for $\hat{\sigma}(x)$

a	x_s	x_e	b
2.3565M Pa	0.000576m	0.03049m	926.121m^{-1}

Figure 5.3 shows $\hat{\sigma}(x)$ fitted to the measured ultrasound beam profile and the microbubble-void transition, defined as $1 - \hat{\sigma}(x)$, having the same x_s , x_e , and c, and $a = 1.0$.

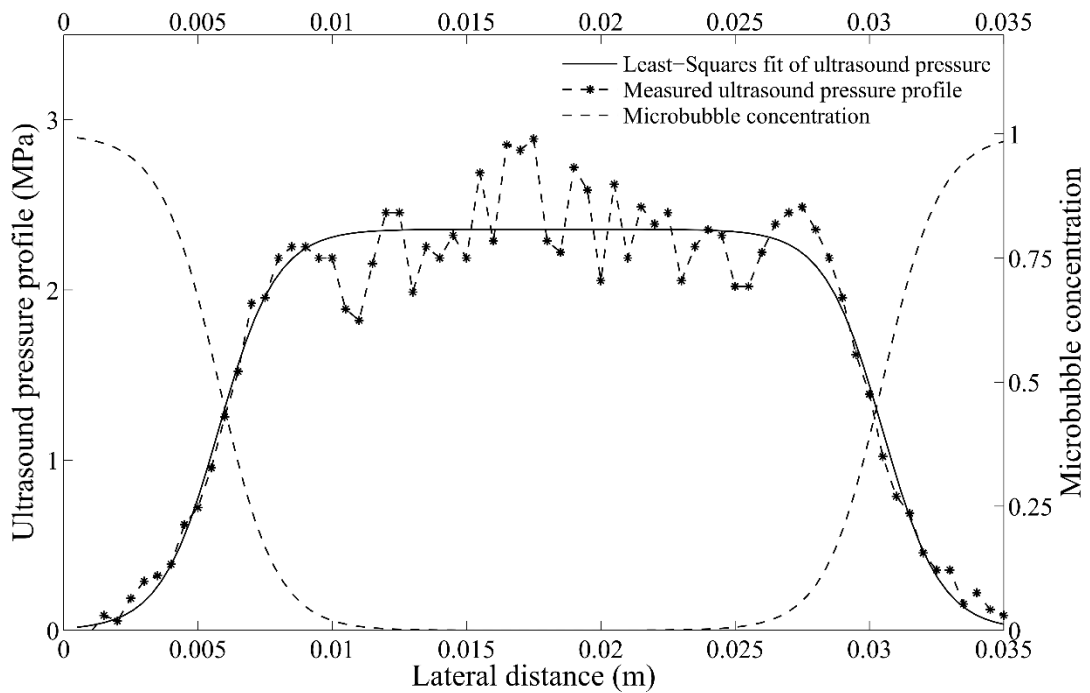


Figure 5.3: Ultrasound peak-to-peak pressure profile (dashed line) and the microbubble-void transition profile (dot-dash line) reconstructed from the fitted ultrasound beam profile function (solid line). Note that the left y-axis corresponds to the measured peak-to-peak ultrasound pressures and the fit function $\hat{\sigma}(x)$ while right y-axis corresponds to the microbubble-void transition profile

5.2.6.5 Computational Method

Hexahedral meshes were produced for each of the three geometries using Star-CCM+ v9.02.005 (CD-Adapco, Melville, NY USA) as shown in Figure 5.4. The grids contained

approximately 8.3M, 12.7M and 16.1M cells in the straight, curved and helical configurations respectively.

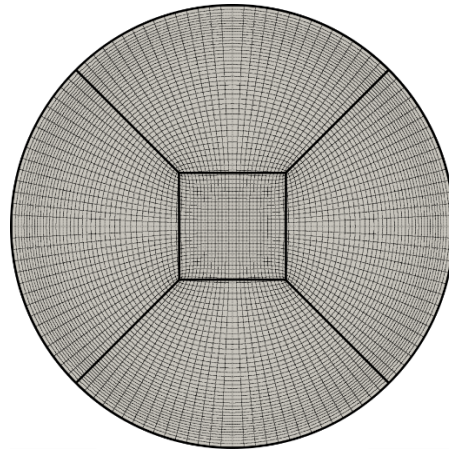


Figure 5.4: A cross-sectional view of the O-grid used. The section was swept along the centrelines of each vessel to produce hexahedral cells

Solutions for the velocity field and the microbubble concentration were obtained via the following procedure:

- Each simulation was initialized with zero velocity and pressure and run until convergence with the segregated steady-state solver
- Each steady-state flow solution (velocity and pressure field) was then used as the initial condition for the implicit unsteady solver, which advanced each simulation 15 seconds. During this time, the segregated solver was kept frozen and only microbubble advective transport was solved for. The time step was 0.01s and each step was solved until residual convergence.

5.3 Results

5.3.1 Microbubble void concentration

Figure 5.5 shows the arrival of the microbubble void observed by high-frame CEUS with two different views. In the image plane along the vessel axis, it can be seen that the initial (flat) wavefront at the site of void creation has developed into an elliptic wave front and travels from left to right whereas the cross-sectional view show the evolution of a circular ring from the centre of the tube toward the tube wall.


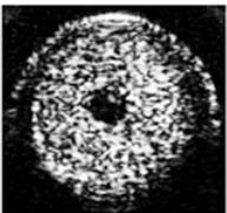

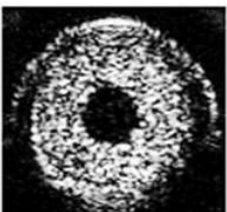
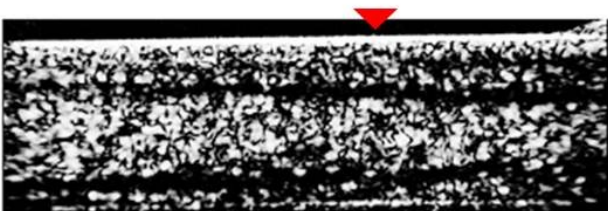

Time (s)	Longitudinal View	Cross-sectional view
2.0		
2.3		
3.0		

Figure 5.5: The arrival of the microbubble void observed by high frame-rate contrast enhanced ultrasound at different time points within an image plane along the vessel axis

(left) and cross-sectional view (right). The elliptical dark wave front is the front of the evolved void (absence of bubbles) travelling along the vessel.

Figure 5.6 shows the qualitative comparison of the temporal analysis of microbubble concentration acquired from CFD solution and ultrasound experiment. It is clear that the structures of the microbubble void acquired from ultrasound images are very similar to the CFD solutions in all cases. These include a circular ring growing progressively from the centre of the tube observed in a straight tube, two symmetrical vortices which progressively increase in size were detected in a curved structure, and two asymmetrical vortices captured in a helical structure. However, it should be noticed that the void structures obtained from ultrasound images in the helical case are not as distinctive as those from the CFD solutions. This may be due to the high degree of mixing in a helical structure and the sensitivity of void detection being beyond ultrasound resolution.

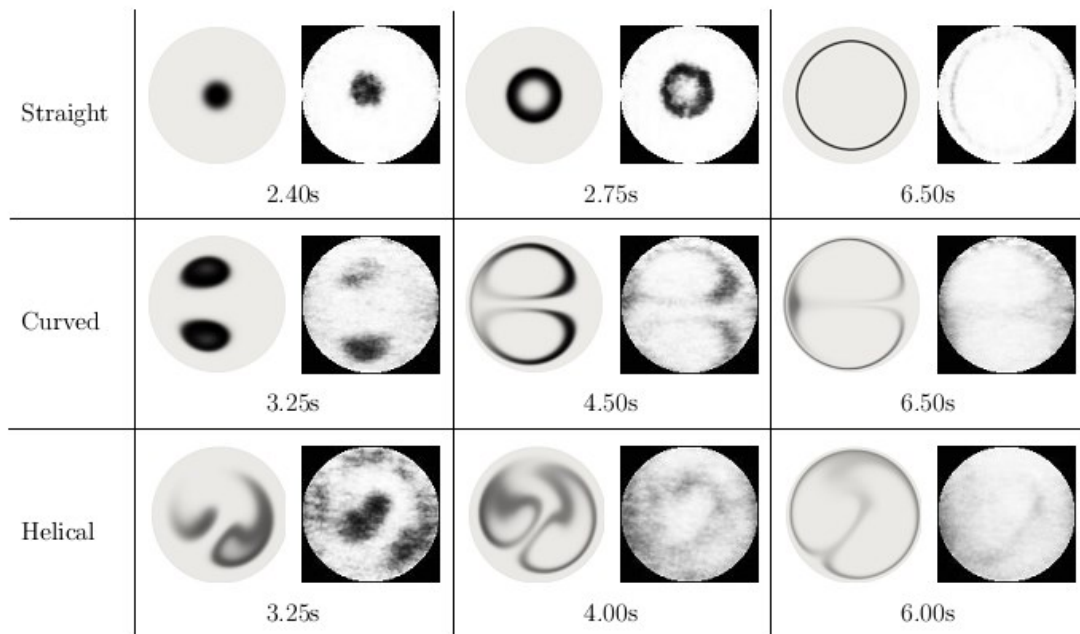


Figure 5.6: Temporal snapshots of microbubble concentration in a plane orthogonal to the vessel centreline at different times. Images on the left are CFD solutions, whereas images on

the right are ultrasound images after contrast enhancement. Note that the outer wall for the curved and helical tubes are on the left hand side,

5.3.2 Mixing evaluation

An entropic measure can be used to quantify the degree of mixing. Specifically, following Cookson et al. [217] the degree of mixing in the case where there are two species (here microbubble and microbubble void) can be quantified as:

$$S = \frac{\sum_{j=1}^{N_b} c_j \ln(c_j) + (1 - c_j) \ln(1 - c_j)}{S_{max}} \quad 5-8$$

where N_b is the number of bins into which the domain is divided, c_j is the microbubble concentration in each bin and $S_{max}=N_b \ln(1/2)$ which corresponds to the case where $c_j=1/2$ in every bin.

Time-entropy curves as illustrated in Figure 5.7 are computed to evaluate the mixing properties. In all cases, results from two independent ultrasound experiments are compared to the CFD solution. As the mixed void region passes through the analysis plane, S increases to a maximum before decaying as the mixed void region leaves the analysis plane. Similar trends are observed in both ultrasound experiments and CFD solutions, but it should be noted that the entropic measure S decreases at a much faster rate in the experimental cases. This disagreement is due to resolution limits on the experimental technique compared to those with the CFD approach.

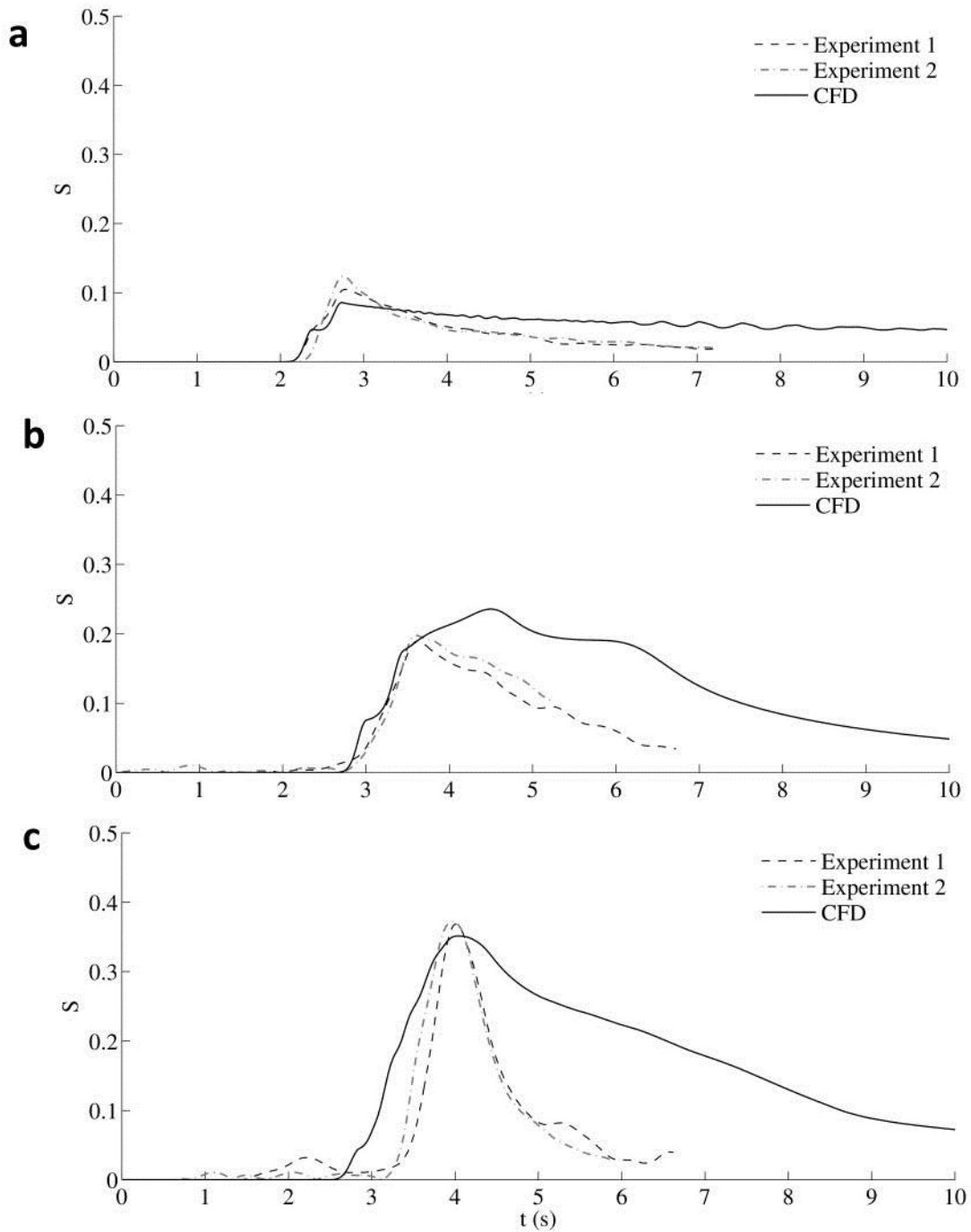


Figure 5.7: Time evolution of entropy measure (S) calculated from CFD (solid line) and two experiments (dashed and dashed-dot lines) obtained using ultrasound imaging in different geometries: (a) straight, (b) curved and (c) helix

The time-entropy curves provide useful information to help quantify the degree of mixing. Here we elect to use the peak entropy obtained over each time series (S_p) to quantify the

degree of mixing induced by each geometry. Figure 5.8 shows values of S_p for each geometry. It can be observed that there is good agreement between the computational and experimental results. It can also be observed that the level of mixing S_p increases from the straight, to the curved, to the helical geometries in line with expectations.

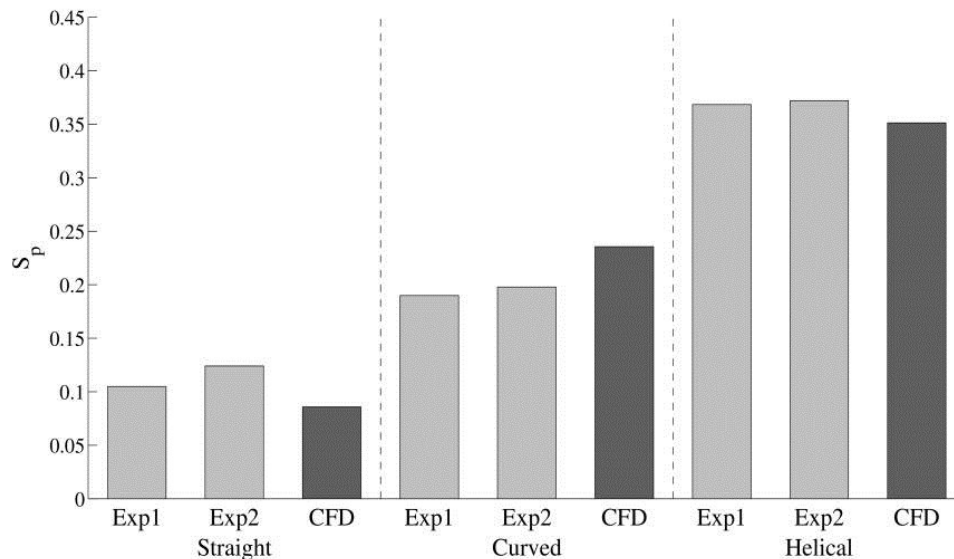


Figure 5.8: Peak entropy obtained over each time series (S_p) obtained using the experimental approach (twice) and the computational results for each geometry.

5.4 Discussion

A new ultrasound imaging technique for non-invasively visualising and quantifying flow mixing in optically opaque media has been developed, using high frame rate ultrasound imaging and controlled microbubble destruction. Initial *in-vitro* evaluation of the system with three different geometries compared with reference CFD solutions has shown the potential of this technique.

Significant advantages of the proposed technique include abolition of the need for local-injection of an indicator (which can be highly invasive and may disturb the flow) and the properties of which may differ from those of the medium into which it is injected. Furthermore, the technique has the potential to allow repeated measurements at various

ultrasound accessible sites following a single injection of indicator and offers a high degree of control of the “indicator injection” in both time and space. Microbubbles can be introduced into the circulation through distant peripheral intravenous injection and then destroyed essentially instantaneously at will with precise spatial and temporal control. The microbubbles are small (1 to 7×10^{-6} m), with negligible mass compared to the surrounding fluid, occupy a very small percentage of volume (volume fraction typically $\leq 0.01\%$ [143], [225]) and have very high Peclet number. Therefore they do not significantly disturb the flow or diffuse far enough within the flow to affect the assessment of flow mixing. Compared with other modalities such as MRI, DSA and CT, which often involve invasive procedures, the proposed method offers a non-ionizing, rapid, real-time and affordable system that can visualise qualitatively the flow field and quantify mixing both *in-vitro* and potentially *in-vivo*. The ultrasound output parameters used in this study for the destruction of microbubbles are within the FDA safety limit[226].

Particles in blood are subject to forces which cause lateral motion of the particle. Based on the Fahraeus-Linquist effect [227], red blood cells (RBCs) migrates toward the centre of vessel leaving a near wall cell-depleted layer where others particles such as platelets and white blood cells (WBCs) tend to concentrate. The margination of particles depends on number of conditions including the concentration, flow rate, particles size and their deformability [228]. Hydrodynamic forces between particles may also lead to complicated radial dispersion[229]. Despite being subjected to the forces, the migration of microbubbles was not observed in Figure 5.6. This is mainly because the boundary layer phenomenon relative to the size of the microbubbles is less effective than that in the micro-circulation. In additions, microbubbles occupies a very small volume fraction ($<0.01\%$) compared to the RBCs and other particles in the bloods. This therefore does not significant alter the flow characteristics and affects the mixing quantification.

Although the proposed method has shown its feasibility in an *in-vitro* study, it can be further refined. The spatial resolution and signal to noise ratio can be further improved by optimisation of the ultrasound system parameters such as frequency and acoustic pressure. In this work the system acquired images at 100fps which is sufficient for the relatively low flow velocity in this study. To deal with the high flow rate in vivo[230] the frame rate can be significantly increased as the imaging system is capable of acquiring at thousands of frames per second[230], which will create much larger amount of data than traditional ultrasound scanners. From a clinical application standpoint, real-time processing would be desirable to provide immediate qualitative and quantitative assessment. This is made possible with recent advances in GPU processing that can provide parallel processing of ultrasound data and can deliver real-time measurements.

Assessment of mixing is valuable in studying fluid-wall mass transport which may play a major role in the initiation and development of vascular pathology such as atherosclerosis and intimal hyperplasia[6], [218]. Using a non-invasive ultrasound method and the technique proposed, not only can we qualitatively observe the mixing and flow field, but also quantitatively evaluate the degree of mixing using a scalar measure. This is attractive since real-time clinical application of the technique could allow correlation of mixing with cardiovascular geometry, flow features and clinical outcome. This leads on to the possibility of designing vascular interventions, such as bypass grafts, arterial stents or arteriovenous fistulae, to optimise outcomes. Equally, the technique presented here may assist in the early diagnosis and management of vascular disease, incorporating indicators of flow into the assessment of lesions.

Future studies with the technique, besides further optimisation of the ultrasound parameters, include assessment of non-steady flow and with different Reynolds numbers and imaging at

different sites relative to bubble destruction site. Given promising results, the study will be extended to pre-clinical *in-vivo* measurements.

5.5 Conclusion

In this study, visualisation and quantification of flow mixing in optically opaque media using plane wave ultrasound imaging and controlled microbubble destruction was demonstrated. Initial experiments on different flow geometries agree well with independent CFD simulations and demonstrate the potential of this technique for cardiovascular applications *in-vivo*.

Chapter 6 - Graphics Processing Unit (GPU) accelerated ultrasound image beamforming and UIV tracking

The plane wave UIV system has shown great potential for visualising and quantifying flow *in-vivo*. However, a large amount of data is generated as a result of the high frame rate image acquisition. Together with the computationally demanding image formation and UIV processing, real time implementation of such a system is known to be a great challenge. In this study, we have developed a graphics processing unit (GPU) based implementation of the coherent compounded plane wave image beamforming and UIV algorithm to accelerate the image formation by leveraging the parallel processing of a GPU. Initial evaluation of the GPU-based implementation with the central processing unit (CPU)-based implementation revealed a relative speedup over 66x for plane wave image formation and 12x for UIV analysis. The processing capability can be further refined by optimizing the GPU implementation and real time processing is possible with the use of more advanced GPU models or multi-GPUs implementations.

6.1 Introduction

The emergence of plane wave ultrasound imaging offers new possibilities in various applications which have been previously limited by the temporal resolution of the conventional ultrasound system [33]. Different from the line-by-line imaging paradigm of a conventional imaging system, a low-resolution image (LRI) covering the whole FOV can be reconstructed by performing delay-and-sum beamforming at every pixel positions from the radio frequency (RF) data acquired from a single pulse echo sequence, and a high-resolution image (HRI) can be computed by employing the coherent plane wave compounding technique to improve the image quality.

While high frame rate ultrasound imaging can be achieved using the plane wave imaging technique, image reconstruction of a plane wave image is far more complicated than a fixed delay-and-sum which works on a line-by-line basis. The computational workload increases not only because of the significant amount of data acquired, but also due to the computation intensive image formation. Each channel data requires a different set of focussing delays to form a LRI, and multiple LRIs need to be reconstructed to form a HRI [231]. Real-time hardware beamformers on existing ultrasound scanners were designed to handle conventional image formation, therefore they are not sufficient to accommodate the computational demand of a plane wave imaging.

The UIV algorithm is an image processing technique which performs cross-correlation analysis to estimate the local flow displacement. Although cross-correlation is widely accepted as a reliable and robust similarity measure, it is also known to be computationally intensive. Fourier cross-correlation is reported to shorten the computation time to some extent [232], but the computational load of cross-correlation analysis in UIV remains high as the iterative image deformation process is implemented to improve the estimation accuracy. The processing workload also increases tremendously as thousands of images are generated from plane wave ultrasound imaging. Real-time application of the UIV analysis is therefore not possible with the current CPU processing and the computing is normally done as a post-processing step in existing studies.

Recent development of general purpose computing on graphic processing units (GPGPU) offers new opportunities for parallel processing in high performance computing. Compared to the central processing units (CPU), GPUs are very efficient parallel processing units. It is cost-effective and the computational power available on modern graphic cards can be easily exploited using the GPU programming environment provided by the graphic card companies. One such platform known as Compute Unified Device Architecture (CUDA), created by

Nvidia to work with programming language such as C and C++, can be easily used to achieve high performance parallel computing.

In this study, our aim is to develop a real-time processing of a plane wave UIV system by leveraging the computational power of GPUs. Initial development of the GPU implementation of plane wave image formation and the UIV processing were demonstrated. The performance of both GPU implementations was evaluated by comparing the GPU implementations to the CPU implementations written in Matlab script to investigate the speedup that can be expected when moving from research work (Matlab) to clinical translation (CUDA).

6.2 Methods

6.2.1 Overview

In this section, the beamforming principle for coherent plane wave compounding and the overview of the UIV algorithm for flow estimation are briefly described.

6.2.1.1 Coherent Plane wave compounding image reconstruction

The major steps of the image reconstruction are illustrated in Figure 6.1. With the channel RF data acquired from a high frame rate ultrasound system, the analytic signal is first computed using the Hilbert transform. This analytic signal conversion step is required to extract the local phase and amplitude signal from the modulated carrier wave [233]. For instance, the local phase is essential for Doppler estimation while the local amplitude is necessary for envelope detection. To perform the Hilbert transform on the discrete RF signal, one technique is to create a one-sided periodic spectrum using frequency domain approach described in [234]. A forward Fast Fourier Transform (FFT) is first performed to convert the time-domain RF signal $r[n]$ to frequency domain spectrum $R[m]$. Next, the one-sided discrete spectrum $S[m]$ can be computed as follow:

$$S[m] = f(x) = \begin{cases} R[0], & m = 0 \\ 2R[m], & 1 \leq m \leq \frac{N}{2} - 1 \\ R[\frac{N}{2}], & m = \frac{N}{2} \\ 0, & \frac{N}{2} + 1 \leq m \leq N - 1 \end{cases} \quad 6-1$$

And finally the complex discrete-time analytic signal $s[n]$ can be computed by performing an inverse FFT on the one-sided discrete analytic signal $S[m]$.

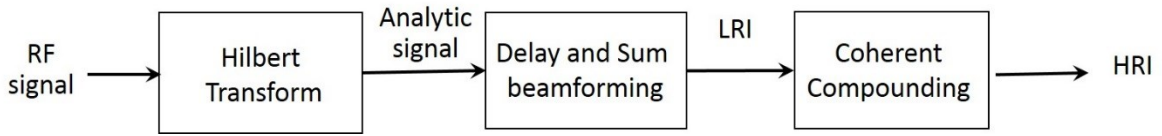


Figure 6.1: Principle workflow of image formation for coherent plane wave compounding technique.

Given the analytic signals, dynamic receive beamforming is performed to compute the LRI from each pulse echo sequence as shown in Figure 6.2. Assuming the plane wave is transmitted in an inclination angle θ during the m^{th} transmission, the backscatter signal at any point in the image can be reconstructed as

$$L_m(x, z) = \sum_{n=1}^N a_n \cdot s_{m,n}(t - \tau(x, z)) \quad 6-2$$

where $s_{m,n}$ is the interpolated signal from the analytic signal, a_n is the receive apodization which corresponding to the element directivity, N is the number of transducer elements, and τ is the round-trip time-of-flight. Element directivity can be seen as a sensitivity map where a transducer element can receive the echo from the field-of-view. The directivity function can be approximated by means of Rayleigh-Sommerfield formula in the far field region denoted as [235], [236].

$$a(\theta) = \text{sinc}\left(\frac{\pi d}{\lambda} \sin \theta\right) \cos \theta \quad 6-3$$

where d is the element width, λ is the wavelength, and θ is the receive observation angle. The round-trip time-of-flight τ can be calculated as

$$\tau = \frac{1}{c} (\{z \cos \theta + x \sin \theta\} + \{\sqrt{z^2 + (x - x_n)^2}\}) \quad 6-4$$

To form a HRI image, M frames of LRIs, each reconstructed from a plane wave pulse-echo sequence transmitted at a different angle, were coherently summed as

$$H_i(x, z) = \sum_{m=1}^M L_m(x, z) \quad 6-5$$

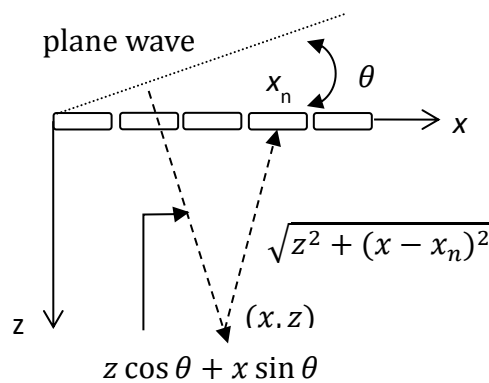


Figure 6.2: Geometry associated with the delay calculation of the coherent plane wave compounding imaging technique.

6.2.1.2 UIV analyses

To facilitate the discussion of our developed algorithm, the principal workflow of the UIV algorithm is illustrated in Figure 6.3. Generally, the algorithm consists of four sub-steps: local displacement estimation, sub-pixel displacement estimation, spurious vector elimination and image deformation. The process is performed over multiple grids, starting on a coarse grid to estimate the large global displacement and moving on to finer grid to estimate smaller local deformations.

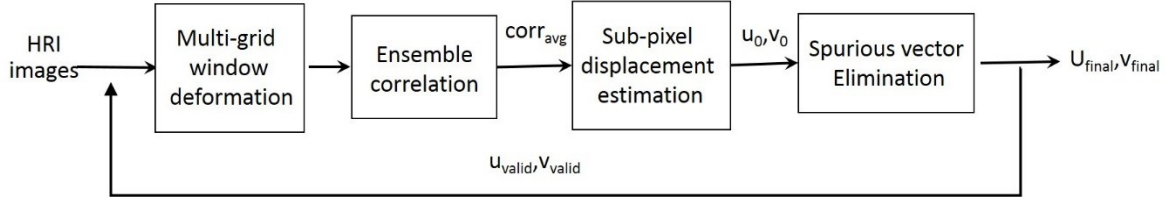


Figure 6.3: (b) Principle workflow of an advanced UIV analysis which incorporates the multigrid window deformation algorithm, the ensemble correlation approach and spurious vector elimination.

To estimate the local displacement, consecutive ultrasound images (I_1, I_2, \dots, I_N) are initially sub-divided into smaller interrogation windows and the corresponding window pairs are cross-correlated using a FFT-based cross-correlation function defined as:

$$R^{n,k}(x, y) = \mathcal{F}^{-1}\{\mathcal{F}(w_1^{n,k}) \mathcal{F}^*(w_2^{n,k})\} \quad 6-6$$

where $w_1(i, j)$ and $w_2(i + u, j + v)$ denote the image intensity distribution of the sub-image pair k , n is the frame number, u and v represent the pixel displacement between the two images, \mathcal{F} and \mathcal{F}^{-1} denote the forward and inverse Fourier transform, and $*$ denotes the complex conjugate. Once the instantaneous correlation function is computed, the ensemble-correlation is calculated by time-averaging N instantaneous correlation planes as follow:

$$R_{avg}^k(x, y) = \sum_{n=1}^N R^{n,k}(x, y) \quad 6-7$$

From the averaged correlation plane, the displacement (in pixels) between two windows is given by the peak location as

$$(u_0^k, v_0^k) = \arg \max_{x,y} R_{avg}^k \quad 6-8$$

and a 3-point Gaussian peak estimator is implemented to estimate the subpixel displacement from the correlation plane[102] as

$$u = u_0 + \frac{\ln R_{(i-1,j)} - \ln R_{(i+1,j)}}{2 \ln R_{(i-1,j)} - 4 \ln R_{(i,j)} + 2 \ln R_{(i+1,j)}} \quad 6-9$$

$$v = v_0 + \frac{\ln R_{(i,j-1)} - \ln R_{(i,j+1)}}{2 \ln R_{(i,j-1)} - 4 \ln R_{(i,j)} + 2 \ln R_{(i,j+1)}} \quad 6-10$$

As the displacement is directly estimated from the peak location in the correlation plane, spurious vectors may emerge if the displacement-correlation peak does not exceed the random correlation peak caused by image noises, loss of correlation due to in-plane and out-of-plane motion and local variations of the velocity field. A 3X3 median filter is used to eliminate spurious vectors with the assumption that the measured displacement field is spatially smooth and certain coherence can be expected in the velocity field.

Finally to deform the images, a predictor for the displacement field is generated from the displacement field estimated in the previous iteration and the images are interpolated using bilinear interpolation.

6.2.2 Computation Platform

A HP workstation (HP Z440; Hewlett-Packard, CA) was used to implement both CPU and GPU algorithm. It has a 8-cores, 2.4GHz processor (Xeon E5-2630 v3; Intel CORPORATION, Santa Clara, CA) and 32GB DDR4 RAM. A NVIDIA GeForce GTX 980 GPU with 2048 cores, 1.126 GHz clock speed and 4GB global memory, was connected as an extension board through PCI-Express 3.0 slot available on the motherboard.

6.2.3 CPU implementation

The CPU algorithm was implemented in Matlab 2013b (MathWorks Inc, Natick, MA, US). To optimize CPU implementation, a built-in profiling tool was used to track down the inefficient steps. Built-in multithreading functions and the parallel computing toolbox were used to accelerate the CPU implementation. Note that although the Matlab implementation may not be the fastest CPU processing, the performance is still relevant to investigate the speedup that would be expected when moving from CPU to GPU processing.

6.2.4 GPU implementation

In this section, the GPU implementation of the image formation and the UIV algorithm using CUDA are presented. The basics of CUDA are briefly described to introduce the GPU programming architecture before the implementation strategies to accelerate the programme are presented.

6.2.4.1 CUDA

CUDA (Compute Unified Device Architecture) is a parallel computing model developed by NVIDIA to work with a GPU for general purpose computing. It can be seen as an extension library of C/C++ which can be incorporated in a C/C++ program and compiled to run simultaneously on GPU processors. More specifically, it consists of kernels (C function) that are launched by host (CPU) but executed on the device (GPU).

In contrast to a regular C function which runs on a single thread, each kernel is executed N times in parallel by N different CUDA threads and the computing threads on a GPU are organized into blocks and grids. Each thread has a limited amount of local memory but threads belonging to the same block can communicate with each other via the shared memory. To synchronise the data among blocks, there exists the large capacity global memory which can be accessed by all threads. Texture and constant memory are additional read-only memory accessible by all threads. The important aspect for choosing different memory is that they have different read and write latencies, as well as different sizes. In general, it is desirable to use shared memory rather than global memory for fast and repeated access if the data are small enough to fit in the shared memory. The threads and memory hierarchy are shown in Figure 6.4.

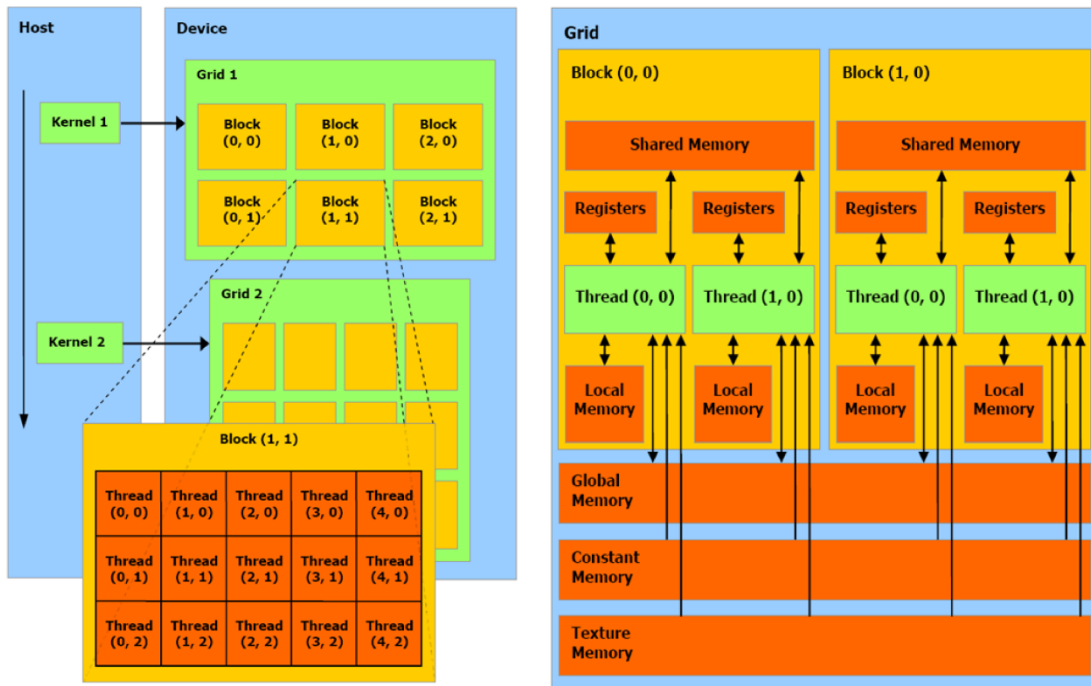


Figure 6.4: Schematic representation of CUDA threads and memory hierarchy [237]

6.2.4.2 CUDA Implementation Strategies

The image reconstruction and UIV algorithms were coded in C. Various CUDA syntaxes and functions were invoked to realize parallel processing on GPU. To achieve highly parallelised implementation, we developed the accelerating kernels respectively according to their computational characteristics and memory access patterns. This is because sufficient threads running simultaneously are needed to keep the GPU occupancy and efficient memory access is required to hide the memory access latency.

To ensure high GPU occupancy, arithmetic operations such as the delay calculations and coherent compounding in the beamforming operation, or the ensemble correlation in UIV algorithm were parallelised such that each thread is processing one pixel data. Highly optimized functions were also used to achieve high processing efficiency. For example, CUFFT library [238], which contains highly optimized parallel FFT functions, was invoked to perform the forward and reverse FFT in the Hilbert transform operation and cross-

correlation function. This allows us to accelerate our implementation without having to develop a custom GPU-based FFT function.

Efficient management of memory access is also crucial to optimize the parallel processing. For example, an optimized peak searching algorithm was developed using the general CUDA reduction method [239] with the entire correlation map stored in the shared memory for fast memory access. However, not all data can be stored in the limited shared memory space. Global memory was used to store large input and output data. Texture memory was also exploited due to its caching behaviour and optimised spatial locality which benefits the data interpolation. Input RF data in the image reconstruction algorithm and the input images in the UIV algorithm were mapped to the texture memory. Linear interpolation in the delay-and-sum operation and bilinear interpolation in the UIV image deformation operation become simple texture lookup where GPU automatically performs the interpolation and saves significant time compared to the global memory access.

To simplify our performance analysis, the GPU-based image reconstruction algorithm and the UIV algorithm were compiled and linked to the MEX-file library to be executed in MATLAB.

6.3 Results

6.3.1 Plane wave image reconstruction

To assess the performance of the CPU and GPU based image reconstruction, RF data, consisting of backscattered signals from multiple point scatterers, were synthesised using a typical data acquisition parameters for coherent plane wave compounding as illustrated in Table 6.1. The CPU and GPU implementations are similar, apart from the fact that GPU computation is in single precision whereas CPU computation is in double precision. This configuration was used because GPU is optimized for single-precision floating-point computation in contrast to Matlab implementation where computation is optimized for double

precision. The reconstructed images using the CPU and GPU implementations are shown in Figure 6.5. It is evident that single-precision GPU implementation did not affect the image quality.

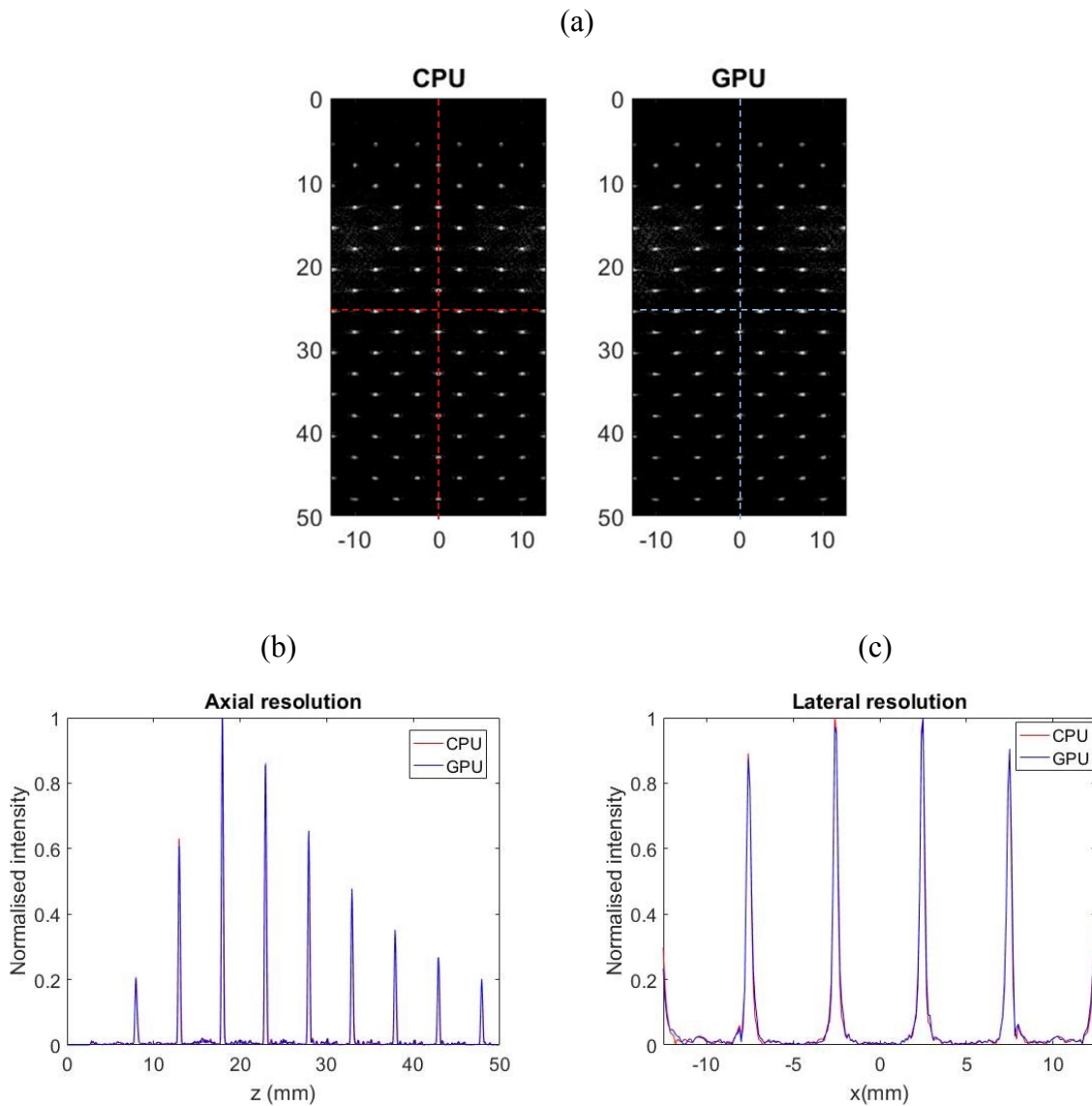


Figure 6.5: (a) Images generated using the CPU and GPU implemented image reconstruction. (b-c) Axial plot and lateral plot of normalised signal intensity to compare the image resolution and signal to noise ratio.

Similar images were reconstructed in two different grids (512x128 pixels and 1024x256 pixels) to compare the reconstruction time of a standard and a fine resolution image. In total

500 LRIs were reconstructed and 100 HRIs were generated by performing coherent compounding on every 5 LRIs. The processing throughputs of both implementations are shown in Figure 6.6.

Table 6.1: Field II simulation setup

Probe parameter		Imaging Parameter	
Probe	L12-3v	Imaging mode	Plane wave
Centre Frequency	8MHz	Transmit Frequency	8MHz
Number of Elements	128	Excitation pulse	1 cycle sinusoidal
Element Pitch	0.2mm	PRF	10kHz
Element Height	5mm	Compounding angle	5
Sampling Frequency	32MHz	Angle Range	20 ⁰
Elevational Focus	20mm	Imaging Depth	5cm

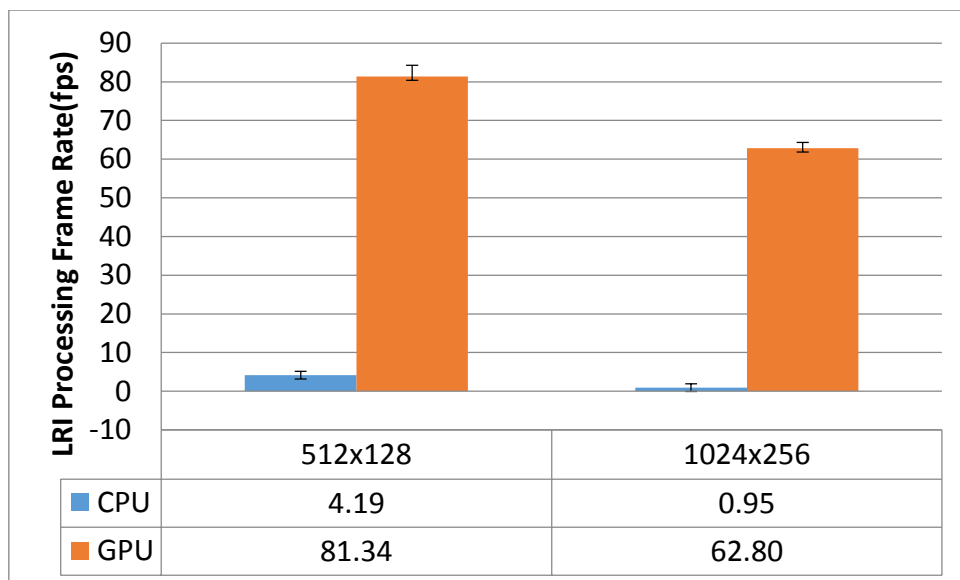


Figure 6.6: Processing throughput of the plane wave image reconstruction using CPU and

GPU. Note that the performance test was repeated for 5 times.

6.3.2 UIV analyses

To evaluate the performance of the UIV algorithm, pulsatile flow images in a model common carotid artery (CCA) (similar to Chapter 4 and Chapter 5) were generated using the setting summarised in Table 6.1. UIV analysis was performed iteratively over 3 different interrogation grids with 50% overlapping (32x32, 16x16 and 8x8 pixels). To illustrate the accuracy of both methods, vector images generated are shown in Figure 6.7. Consistent results were found between the CPU and GPU implementations.

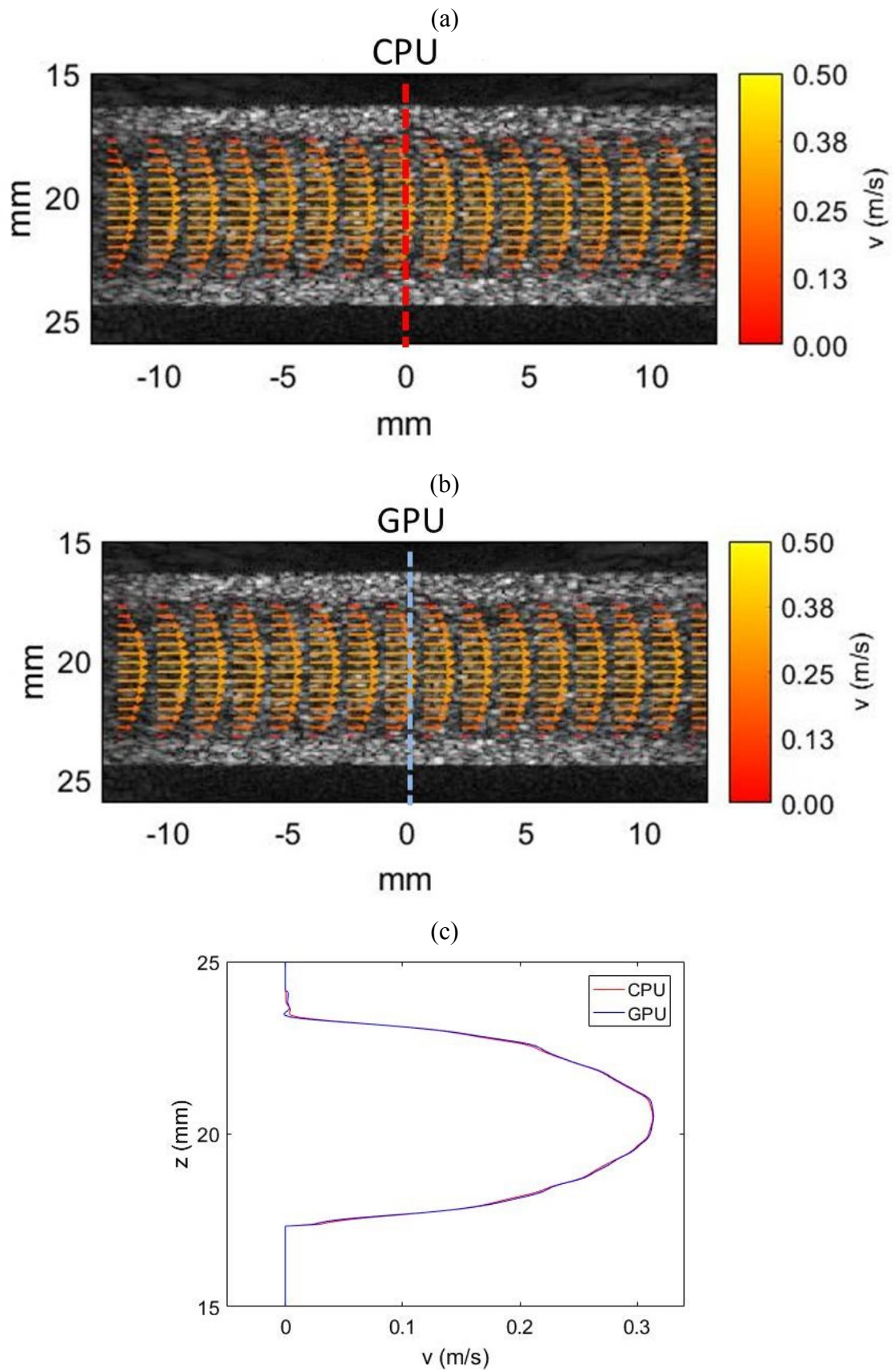


Figure 6.7: Vector images generated using (a) CPU implementation, (b) GPU implementation. (c) Comparison of the axial velocity profiles generated using different implementations.

To demonstrate the speed improvement when translating a CPU implementation to a GPU implementation, timings for normal UIV without ensemble correlation ($N=1$) and with ensemble correlation ($N=5$) were investigated. In total 100 HRI images were tested and the average time to generate one vector image for both CPU and GPU implementation are shown in Figure 6.8.

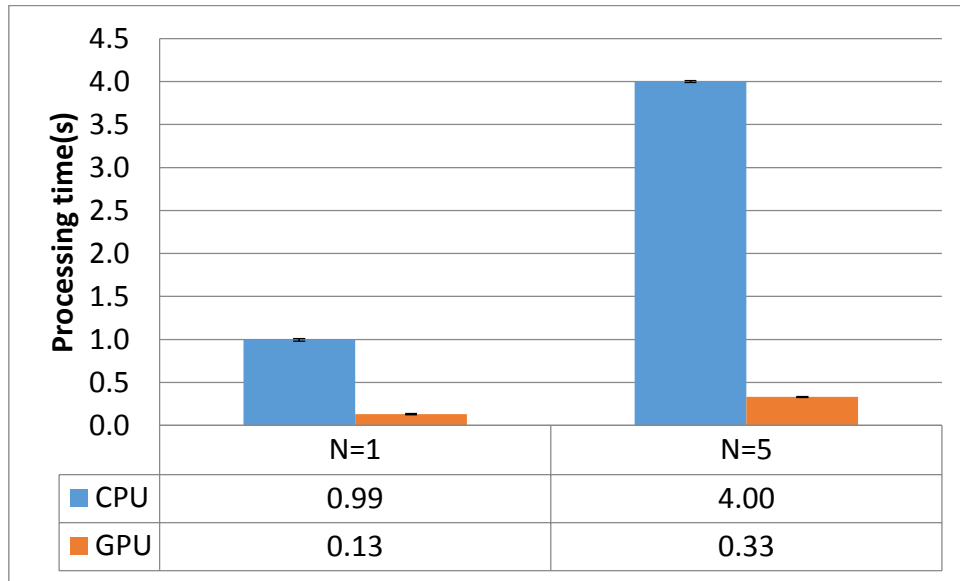


Figure 6.8: Comparison of the average processing time to generate single vector image using CPU- and GPU-based UIV implementation.

6.4 Discussion

The GPU-based implementations of the coherent plane wave image reconstruction and UIV algorithm were developed to pursue the real-time implementation of the UIV system. From the results in Figure 6.6 and Figure 6.8, there is a relative speedup of at least 19x for the image reconstruction algorithm and 8x improvement with the UIV algorithm. The performance increment becomes more significant when more computations were performed on the same set of input data. Relative speedup over 66x and 12x were found for the GPU image reconstruction and UIV analysis when the processing load increased. Such observations are expected as memory transfer between CPU and GPU requires time and the

memory transfer latency can be reduced when more computations are done using the same data.

Although initial evaluation indicates significant speed improvement when using the GPU implementation, several limitations have been found in our evaluations. First, MATLAB implementation is not considered to be the most computationally efficient platform for CPU implementation. Multi-threaded CPU implementation is used by invoking the built-in multithreading functions and parallel computing toolbox, but to what extent an optimised multi-threaded CPU implementation would affect the results needs to be investigated. Next, the precision difference, although it did not affect the calculation accuracy (Figure 6.5 and Figure 6.7), may have an impact on the computational time. Comparison should be done with consistent floating-point precision for both CPU and GPU implementations.

NVidia GTX980 is a high-end GPU which is capable of processing 4.6TFLOPS. In this study, one order of magnitude increment was achieved in both GPU implementations; however, further improvement of the implementation is still needed to fully accelerate the processing for real time applications. Further optimisation of the GPU implementation to maximise the independent parallelism and optimize the memory access in both algorithms is possible to increase the processing throughput. Alternative algorithms with lower computational complexity can also be adopted to increase the processing throughput. For instance, Fourier beamforming or a compressed sensing model which could reduce the processing demands by a factor of 20 is a good alternative for delay-and-sum beamforming in order to achieve real time implementation[240].

While higher computation power can be realised with a newer or faster GPU hardware, parallel processing is not restricted to a single GPU implementation. The performance of a GPU implementation can be easily scaled up by leveraging the multi-GPU processing. Note

that with such scalability, real-time implementation of the plane wave UIV system is possible in the future.

6.5 Conclusion

Plane wave image reconstruction and UIV analysis are computationally intensive task that required high performance computing to maintain efficiency. With the advancement of GPU parallel computing, we demonstrated the potential of a GPU-based implementation to accelerate the processing of a plane wave UIV system and the opportunity of such system as a real-time application for visualising and quantifying flow *in-vivo*.

Chapter 7 - Conclusion and future work

7.1 Summary and conclusions

The research reported in the thesis was driven by the aim to develop non-invasive techniques capable of visualising and quantifying blood flow using a high frame rate ultrasound system. In chapter 2, a plane wave UIV system which is capable of visualising and quantifying dynamic flow was developed. To the best of our knowledge, the use of plane wave imaging to track microbubbles in the blood stream has not been reported. Initial evaluations of the system *in-vitro* on both straight and carotid-mimicking vessels, and *in-vivo* in the rabbit aorta were conducted. Good agreements were found when comparing the UIV flow velocity mapping results to the theoretical predictions and Doppler measurements. The tracking of complex flow patterns and the transitory behaviour of the flow within a physiologically relevant geometry reveal the advantages of our developed system in visualising and quantifying complex flow dynamics which was not possible with a conventional flow imaging system. The *in-vitro* and *in-vivo* results also indicate the potential of the plane wave UIV system as a highly sensitive, accurate, angle dependent and full field-of-view velocity mapping tools.

In chapter 3, a modified UIV technique was developed to circumvent the motion artefacts that may affect the flow estimation when the coherent plane wave compounding technique is used to form an image. Simulation and experimental studies were conducted to evaluate the accuracy of both UIV algorithms and their robustness against motion artefacts. From the results, we demonstrated that the normal UIV method failed to estimate fast flow with high spatial velocity gradients. However, the motion artefact can be overcome using the modified UIV technique. Highly accurate and angle independent 2D velocity measurements with errors less than 10% under steady flow and 5% under pulsatile flow were found when using the modified UIV to estimate the flow. The motion artefacts which affect the normal UIV

estimation were also demonstrated in a diseased carotid phantom. Highly accelerated flow motion between emissions results in significant image artefacts which later affect the standard UIV estimation. With the modified UIV method, we showed that the motion artefacts can be avoided and the high-speed jet flow can be retrieved.

Once the capability of the plane wave UIV system to provide reliable flow velocity estimation was demonstrated, we extended our technique to derive WSS directly from the UIV velocity measurement in Chapter 4. Initial evaluations of our technique using simulated flow images has demonstrated the potential of our technique to provide accurate spatio-temporal WSS estimations with mean error of 8.56% under steady and 13.97% under pulsatile flow condition. However, a simulation study also reveals the need for accurate wall tracking up to sub-pixel accuracy. Derivation of the WSR directly from the flow velocity profile is very sensitive to the identified wall position as a 50um error on the wall position may result in as high as 20% WSR estimation error. It was assumed that the use of a high frame rate imaging system which is capable of imaging over one thousand frames per second and the contrast imaging which help in differentiating wall-fluid boundary, may minimize the wall tracking error. However, further evaluation is required to estimate the accuracy of the various wall-segmentation algorithms available. Initial *in-vitro* investigation on two carotid bifurcation phantoms was conducted and the differences in the WSS distribution due to their local geometry and flow were presented. The simulation and experimental results indicate the potential of such technique to quantify the WSS distribution in addition to the flow velocity.

In chapter 5, we reported a novel non-invasive technique for flow visualisation and quantification of flow-induced mixing using plane wave ultrasound imaging and controlled destruction of microbubble contrast agents. Initial experiments on three different model vessel geometries with known effects on the flow field and the mixing properties were conducted. The results indicate the capabilities of the technique to visualise secondary flow

and quantify the degree of mixing within the different configuration. The experimental results were cross-validated with the CFD simulations. of the good agreement between the CFD and the experimental results demonstrates the potential of the technique for cardiovascular application *in-vivo*.

In chapter 6, we developed a GPU-based implementation of the plane wave UIV system to accelerate the computationally demanding image reconstruction and flow estimation process. The plane wave image reconstruction and UIV flow estimation algorithm were reviewed and the initial GPU implementations of both algorithms were evaluated. Comparing to the CPU-based implementation, GPU-implementation speeded up the image formation process and UIV analysis over 66x and 12x respectively. As further improvement to the GPU implementation is possible, we concluded that the real-time application of the plane wave UIV system is possible in the near future.

Overall, techniques developed based on high frame rate ultrasound imaging and microbubble contrast agent has shown great potential for flow visualisation and quantification *in-vivo*. These techniques also hold the promise in being introduced as routine diagnostic tool to investigate human vascular flow dynamics by providing sensitive and accurate flow parameters such as flow velocity, wall shear stress and intraluminal mixing.

7.2 Future works

Because plane wave UIV technique has shown promising result in visualising and quantifying flow velocity, immediate efforts are being put into developing a real-time system. Initial GPU implementation has demonstrated a significant speedup when compared to the CPU-implementation; however, comparing to the GPU-based beamformer reported in [44], our image formation throughputs is 10 times less than their implementation. The main reason is that our implementation is not optimized where independent parallelism is not maximised

and the memory access is not efficient. With a better implementation, our implementation would benefit from at least another 10x performance speedup. In addition, multi-GPU implementation which can scale-up the processing power may well be done to achieve real-time processing.

To apply our techniques *in-vivo*, further work to improve the flow quantification and visualisation needs to be conducted. With respect to the flow velocity estimation, optimization of the acquisition parameters to enhance the image quality and the velocity estimation need to be investigated. For example, investigation of the number of compounding and imaging frame rate needs to be conducted to find a balance between spatial and temporal resolution while maintaining the tracking accuracy. In addition, a potential limitation lies in using the 2D imaging system to quantify 3D flow. The out-of-plane motion which affects the flow quantification was observed in the *in-vivo* experiment in Chapter 3. Although such error may well be resolved by using a 3D ultrasound system, suggesting future work to investigate the error due to the out-of-plane motion can also be done. Vector flow visualisation is another challenge that needs to be solved. In this study, static color-coded arrow displays were used to represent the magnitude and direction of the flow while streamline images were used to depict the separations location. Dynamic visualisation algorithm which update the position of the flow vector between frame imaging can be adopted to highlight the dynamic nature of the flow[73].

Apart from the 2D flow visualisation and quantification, 3D high frame rate flow imaging needs to be developed. As the anatomical structures are three-dimensional, 3D ultrasound imaging can overcome the limitations of the 2D imaging system to provide more comprehensive and accurate volumetric flow estimation. However, currently available 3D systems, which are based on the line-by-line imaging sequence, are limited to a small field-of-view and the imaging frame-rate are relatively low. The high frame rate ultrasound

imaging system provides a solution to increase the imaging frame rate while imaging a large field-of-view has been demonstrated in [241], [242]. To realise a 3D high frame rate flow imaging system, future work should include the expansion of our system to 3D acquisitions, extension of our technique to the 3D measurement, optimising the imaging settings for 3D measurements, accelerating the process to handle larger amount of data comparing to 2D acquisition, and provide a visualisation software to display the 3D data.

Another suggested future work is to improve the ultrasound flow simulation used in evaluating the flow velocity and WSS estimation. Such a simulation would be useful as a controlled environment can be simulated where the ground truth is known. In the current study, the rigid straight tube model with axisymmetric flow distribution is insufficient to represent the real vessels which generally present irregular geometries with complex flow structures. A more realistic and complex flow model that incorporates deformable wall motion, out-of-plane flow motion and spatially varying flow is necessary to fully evaluate the performance of our developed techniques in quantifying flow velocity and WSS. To realise such a simulation, the idealised flow simulation can be replaced with the CFD simulation as reported in [178]

For the microbubble void imaging studies, promising results were shown in visualising the secondary flow and quantifying the intraluminal flow mixing under steady flow condition in different geometries. Further studies include assessment under pulsatile flow condition, investigation of the effect of quantification when imaging at different site relative to the bubble destruction site and optimisation of the ultrasound imaging parameters.

Last but not least, as mainly *in-vitro* investigations were demonstrated in this thesis, the study should be extended to pre-clinical *in-vivo* measurements.

Bibliography

- [1] C. S. Fox, J. F. Polak, I. Chazaro, A. Cupples, P. A. Wolf, R. A. D'Agostino, and C. J. O'Donnell, "Genetic and Environmental Contributions to Atherosclerosis Phenotypes in Men and Women," *Stroke*, vol. 34, no. 2, pp. 397–401, Feb. 2003.
- [2] S. Kovacic and M. Bakran, "Genetic Susceptibility to Atherosclerosis," *Stroke Res. Treat.*, vol. 2012, p. e362941, Mar. 2012.
- [3] C. G. Caro, "Vascular fluid dynamics and vascular biology and disease," *Math. Methods Appl. Sci.*, vol. 24, no. 17–18, pp. 1311–1324, 2001.
- [4] E. Cecchi, C. Giglioli, S. Valente, C. Lazzeri, G. F. Gensini, R. Abbate, and L. Mannini, "Role of hemodynamic shear stress in cardiovascular disease," *Atherosclerosis*, vol. 214, no. 2, pp. 249–256, Feb. 2011.
- [5] G. Coppola and C. Caro, "Arterial geometry, flow pattern, wall shear and mass transport: potential physiological significance," *J. R. Soc. Interface*, vol. 6, no. 35, pp. 519–528, Jun. 2009.
- [6] C. G. Caro, "Discovery of the Role of Wall Shear in Atherosclerosis," *Arterioscler. Thromb. Vasc. Biol.*, vol. 29, no. 2, pp. 158–161, Feb. 2009.
- [7] D. Ku, D. Giddens, D. Phillips, and D. Strandness Jr, "Hemodynamics of the normal human carotid bifurcation: In vitro and in vivo studies," *Ultrasound Med. Biol.*, vol. 11, no. 1, pp. 13–26, 1985.
- [8] C. Caro and R. Schroter, "Arterial wall shear and distribution of early atheroma in man," *Nature*, vol. 223, pp. 1159–1161, 1969.
- [9] D. N. Ku, D. P. Giddens, C. K. Zarins, and S. Glagov, "Pulsatile flow and atherosclerosis in the human carotid bifurcation. Positive correlation between plaque location and low oscillating shear stress.," *Arterioscler. Thromb. Vasc. Biol.*, vol. 5, no. 3, pp. 293–302, 1985.
- [10] J.-J. Chiu and S. Chien, "Effects of Disturbed Flow on Vascular Endothelium: Pathophysiological Basis and Clinical Perspectives," *Physiol. Rev.*, vol. 91, no. 1, Jan. 2011.
- [11] M. J. Levesque, D. Liepsch, S. Moravec, and R. M. Nerem, "Correlation of endothelial cell shape and wall shear stress in a stenosed dog aorta," *Arterioscler. Thromb. Vasc. Biol.*, vol. 6, no. 2, pp. 220–229, Mar. 1986.
- [12] P. F. Davies, "Flow-mediated endothelial mechanotransduction," *Physiol. Rev.*, vol. 75, no. 3, pp. 519–560, 1995.
- [13] R. F. Furchgott and J. V. Zawadzki, "The obligatory role of endothelial cells in the relaxation of arterial smooth muscle by acetylcholine," *Nature*, vol. 288, no. 5789, pp. 373–376, Nov. 1980.
- [14] A. M. Shaaban and A. J. Duerinckx, "Wall shear stress and early atherosclerosis: a review," *Am. J. Roentgenol.*, vol. 174, no. 6, pp. 1657–1665, 2000.
- [15] O. VONRAMM and S. SMITH, "Beam Steering with Linear Arrays," *IEEE Trans. Biomed. Eng.*, vol. 30, no. 8, pp. 438–452, 1983.
- [16] S. I. Nikolov, J. Kortbek, and J. A. Jensen, "Practical applications of synthetic aperture imaging," in *Ultrasonics Symposium (IUS), 2010 IEEE*, 2010, pp. 350–358.

- [17] J. Powers and F. Kremkau, "Medical ultrasound systems," *Interface Focus*, vol. 1, no. 4, pp. 477–489, May 2011.
- [18] M. O'Donnell and L. J. Thomas, "Efficient synthetic aperture imaging from a circular aperture with possible application to catheter-based imaging," *Ultrason. Ferroelectr. Freq. Control IEEE Trans. On*, vol. 39, no. 3, pp. 366–380, 1992.
- [19] J. T. Ylitalo and H. Ermert, "Ultrasound synthetic aperture imaging: monostatic approach," *Ultrason. Ferroelectr. Freq. Control IEEE Trans. On*, vol. 41, no. 3, pp. 333–339, 1994.
- [20] L. F. Nock and G. E. Trahey, "Synthetic receive aperture imaging with phase correction for motion and for tissue inhomogeneities. I. Basic principles," *Ultrason. Ferroelectr. Freq. Control IEEE Trans. On*, vol. 39, no. 4, pp. 489–495, 1992.
- [21] G. E. Trahey and L. F. Nock, "Synthetic receive aperture imaging with phase correction for motion and for tissue inhomogeneities. II. Effects of and correction for motion," *Ultrason. Ferroelectr. Freq. Control IEEE Trans. On*, vol. 39, no. 4, pp. 496–501, 1992.
- [22] S. I. Nikolov, "Synthetic aperture tissue and flow ultrasound imaging," Technical University of Denmark, Center for Fast Ultrasound Imaging, 2001.
- [23] G. Lockwood and F. Foster, "Design of sparse array imaging systems," in *1995 IEEE Ultrasonics Symposium Proceeding*, 1995, pp. 1237–1243.
- [24] C. R. Hazard and G. R. Lockwood, "Theoretical assessment of a synthetic aperture beamformer for real-time 3-D imaging," *Ultrason. Ferroelectr. Freq. Control IEEE Trans. On*, vol. 46, no. 4, pp. 972–980, 1999.
- [25] G. R. Lockwood and F. S. Foster, "Optimizing sparse two-dimensional transducer arrays using an effective aperture approach," in *Ultrasonics Symposium, 1994. Proceedings., 1994 IEEE*, 1994, vol. 3, pp. 1497–1501.
- [26] G. R. Lockwood, J. R. Talman, and S. S. Brunke, "Real-time 3-D ultrasound imaging using sparse synthetic aperture beamforming," *Ultrason. Ferroelectr. Freq. Control IEEE Trans. On*, vol. 45, no. 4, pp. 980–988, 1998.
- [27] S. Nikolov, K. Gammelmark, and J. A. Jensen, "Recursive ultrasound imaging," in *1999 IEEE Ultrasonics Symposium, 1999. Proceedings*, 1999, vol. 2, pp. 1621–1625 vol.2.
- [28] Y. Tasinkevych, I. Trots, A. Nowicki, and P. A. Lewin, "Modified synthetic transmit aperture algorithm for ultrasound imaging," *Ultrasonics*, vol. 52, no. 2, pp. 333–342, Feb. 2012.
- [29] K. L. Gammelmark and J. A. Jensen, "Multielement synthetic transmit aperture imaging using temporal encoding," *IEEE Trans. Med. Imaging*, vol. 22, no. 4, pp. 552–563, Apr. 2003.
- [30] T. X. Misaridis and J. A. Jensen, "Space-time encoding for high frame rate ultrasound imaging," *Ultrasonics*, vol. 40, no. 1, pp. 593–597, 2002.
- [31] T. Misaridis and J. A. Jensen, "Use of modulated excitation signals in medical ultrasound. Part III: high frame rate imaging," *Ultrason. Ferroelectr. Freq. Control IEEE Trans. On*, vol. 52, no. 2, pp. 208–219, 2005.
- [32] G. Fredrik, "Spatio-temporal encoding in medical ultrasound imaging," DTU Electrical Engineering, 2005.

- [33] F. Gran and J. A. Jensen, "Spatial encoding using a code division technique for fast ultrasound imaging," *IEEE Trans. Ultrason. Ferroelectr. Freq. Control*, vol. 55, no. 1, pp. 12–23, Jan. 2008.
- [34] B. Delannoy, R. Torguet, C. Bruneel, E. Bridoux, J. M. Rouvaen, and H. Lasota, "Acoustical image reconstruction in parallel-processing analog electronic systems," *J. Appl. Phys.*, vol. 50, no. 5, pp. 3153–3159, May 1979.
- [35] D. P. Shattuck and M. D. Weinshenker, "Explososcan: A parallel processing technique for high speed ultrasound imaging with linear phased arrays.pdf," *J. Acoust. Soc. Am.*, pp. 1273–1282, Aug. 1983.
- [36] M. Fink, D. Cassereau, A. Derode, C. Prada, P. Roux, M. Tanter, Jean-Louis Thomas, and F. Wu, "Time-reversed acoustics," *Rep. Prog. Phys.*, vol. 63, no. 12, p. 1933, 2000.
- [37] M. Fink, C. Prada, F. Wu, and D. Cassereau, "Self focusing in inhomogeneous media with time reversal acoustic mirrors," in *Ultrasonics Symposium, 1989. Proceedings., IEEE 1989*, 1989, pp. 681–686 vol.2.
- [38] M. Fink, "Time reversal of ultrasonic fields. I. Basic principles," *IEEE Trans. Ultrason. Ferroelectr. Freq. Control*, vol. 39, no. 5, pp. 555–566, 1992.
- [39] Mathias Fink, Gabriel Montaldo, and M. Tanter, "Time-Reversal Acoustics in Biomedical Engineering," *Annu. Rev. Biomed. Eng.*, vol. 5, no. 1, pp. 465–497, 2003.
- [40] J.-Y. Lu and J. F. Greenleaf, "Ultrasonic nondiffracting transducer for medical imaging," *IEEE Trans. Ultrason. Ferroelectr. Freq. Control*, vol. 37, no. 5, pp. 438–447, 1990.
- [41] J.-Y. Lu and J. F. Greenleaf, "Pulse-echo imaging using a nondiffracting beam transducer," *Ultrasound Med. Biol.*, vol. 17, no. 3, pp. 265–281, Jan. 1991.
- [42] R. E. Daigle, "Ultrasound imaging system with pixel oriented processing," Oct. 2012.
- [43] K.-H. S. Hayden, J. Chen, B. Y. Yiu, and A. C. Yu, "Medical Ultrasound Imaging: To GPU or Not to GPU?(HTML)," 2011.
- [44] B. Y. S. Yiu, I. K. H. Tsang, and A. C. H. Yu, "GPU-based beamformer: Fast realization of plane wave compounding and synthetic aperture imaging," *IEEE Trans. Ultrason. Ferroelectr. Freq. Control*, vol. 58, no. 8, pp. 1698–1705, Aug. 2011.
- [45] L. Sandrin, S. Manneville, and M. Fink, "Ultrafast two-dimensional ultrasonic speckle velocimetry: A tool in flow imaging," *Appl. Phys. Lett.*, vol. 78, no. 8, pp. 1155–1157, 2001.
- [46] J. McLaughlin and D. Renzi, "Shear wave speed recovery in transient elastography and supersonic imaging using propagating fronts," *Inverse Probl.*, vol. 22, no. 2, pp. 681–706, Apr. 2006.
- [47] T. K. Song and J. H. Chang, "Synthetic aperture focusing method for ultrasound imaging based on planar waves," May 2004.
- [48] J. Cheng and J. –. Lu, "Extended high-frame rate imaging method with limited-diffraction beams," *Ultrason. Ferroelectr. Freq. Control IEEE Trans. On*, vol. 53, no. 5, pp. 880–899, 2006.
- [49] J. –. Lu, "Experimental study of high frame rate imaging with limited diffraction beams," *Ultrason. Ferroelectr. Freq. Control IEEE Trans. On*, vol. 45, no. 1, pp. 84–97, 1998.

- [50] G. Montaldo, M. Tanter, J. Bercoff, N. Benech, and M. Fink, “Coherent plane-wave compounding for very high frame rate ultrasonography and transient elastography,” *IEEE Trans. Ultrason. Ferroelectr. Freq. Control*, vol. 56, no. 3, pp. 489–506, Mar. 2009.
- [51] J. Bercoff, G. Montaldo, T. Loupas, D. Savery, F. Mézière, M. Fink, and M. Tanter, “Ultrafast compound doppler imaging: providing full blood flow characterization,” *IEEE Trans. Ultrason. Ferroelectr. Freq. Control*, vol. 58, no. 1, pp. 134–147, Jan. 2011.
- [52] F. Forsberg, D. Merton, J. Liu, L. Needleman, and B. Goldberg, “Clinical applications of ultrasound contrast agents,” *ULTRASONICS*, vol. 36, no. 1–5, pp. 695–701, Feb. 1998.
- [53] S. B. Feinstein, B. Coll, D. Staub, D. Adam, A. F. L. Schinkel, F. J. Cate, and K. Thomenius, “Contrast enhanced ultrasound imaging,” *J. Nucl. Cardiol.*, vol. 17, no. 1, pp. 106–115, Nov. 2009.
- [54] J. R. Lindner, “Microbubbles in medical imaging: current applications and future directions,” *Nat. Rev. Drug Discov.*, vol. 3, no. 6, pp. 527–533, 2004.
- [55] E. P. Stride and C. C. Coussios, “Cavitation and contrast: the use of bubbles in ultrasound imaging and therapy,” *Proc. Inst. Mech. Eng. [H]*, vol. 224, no. 2, pp. 171–191, 2010.
- [56] J.-M. Correas, L. Bridal, A. Lesavre, A. Méjean, M. Claudon, and O. Hélénon, “Ultrasound contrast agents: properties, principles of action, tolerance, and artifacts,” *Eur. Radiol.*, vol. 11, no. 8, pp. 1316–1328, Apr. 2014.
- [57] J. E. Powers, P. N. Burns, and J. Souquet, “Imaging instrumentation for ultrasound contrast agents,” in *Advances in Echo Imaging Using Contrast Enhancement*, Springer Netherlands, 1997, pp. 139–170.
- [58] F. Forsberg, W. T. Shi, and B. B. Goldberg, “Subharmonic imaging of contrast agents,” *Ultrasonics*, vol. 38, no. 1–8, pp. 93–98, Mar. 2000.
- [59] K. Wei, A. R. Jayaweera, S. Firoozan, A. Linka, D. M. Skyba, and S. Kaul, “Quantification of myocardial blood flow with ultrasound-induced destruction of microbubbles administered as a constant venous infusion,” *Circulation*, vol. 97, no. 5, pp. 473–483, 1998.
- [60] F. Lin, C. Cachard, F. Varray, and O. Basset, “Generalization of Multipulse Transmission Techniques for Ultrasound Imaging,” *Ultrason. Imaging*, vol. 37, no. 4, pp. 294–311, Oct. 2015.
- [61] O. Couture, M. Fink, and M. Tanter, “Ultrasound contrast plane wave imaging,” *IEEE Trans. Ultrason. Ferroelectr. Freq. Control*, vol. 59, no. 12, pp. 2676–2683, Dec. 2012.
- [62] M. Tanter and M. Fink, “Ultrafast imaging in biomedical ultrasound,” *Ultrason. Ferroelectr. Freq. Control IEEE Trans. On*, vol. 61, no. 1, pp. 102–119, 2014.
- [63] C. Kasai, K. Namekawa, A. Koyano, and R. Omoto, “Real-time two-dimensional blood flow imaging using an autocorrelation technique,” *IEEE Trans Sonics Ultrason*, vol. 32, no. 3, pp. 458–464, 1985.
- [64] T. Loupas, J. T. Powers, and R. W. Gill, “An axial velocity estimator for ultrasound blood flow imaging, based on a full evaluation of the Doppler equation by means of a

- two-dimensional autocorrelation approach,” *Ultrason. Ferroelectr. Freq. Control IEEE Trans. On*, vol. 42, no. 4, pp. 672–688, 1995.
- [65] D. H. Evans, J. A. Jensen, and M. B. Nielsen, “Ultrasonic colour Doppler imaging,” *Interface Focus*, vol. 1, no. 4, pp. 490–502, Aug. 2011.
- [66] P. R. Hoskins, “A review of the measurement of blood velocity and related quantities using Doppler ultrasound,” *Proc. Inst. Mech. Eng. [H]*, vol. 213, no. 5, pp. 391–400, May 1999.
- [67] B. Dunmire, K. W. Beach, K.-H. Labs, M. Plett, and D. E. Strandness Jr., “Cross-beam vector Doppler ultrasound for angle-independent velocity measurements,” *Ultrasound Med. Biol.*, vol. 26, no. 8, pp. 1213–1235, Oct. 2000.
- [68] B. Dunmire and K. W. Beach, “Brief history of vector Doppler,” in *Medical Imaging 2001*, 2001, pp. 200–214.
- [69] O. D. Kripfgans, J. M. Rubin, A. L. Hall, and J. B. Fowlkes, “Vector Doppler imaging of a spinning disc ultrasound Doppler phantom,” *Ultrasound Med. Biol.*, vol. 32, no. 7, pp. 1037–1046, Jul. 2006.
- [70] S. Ricci, L. Bassi, and P. Tortoli, “Information Engineering Department, Florence University, Firenze, Italy,” *Ultrason. Ferroelectr. Freq. Control IEEE Trans. On*, vol. 61, no. 2, pp. 314–324, 2014.
- [71] R. Steel, K. V. Ramnarine, A. Criton, F. Davidson, P. L. Allan, N. Humphries, H. F. Routh, P. J. Fish, and P. R. Hoskins, “Angle-dependence and reproducibility of dual-beam vector doppler ultrasound in the common carotid arteries of normal volunteers,” *Ultrasound Med. Biol.*, vol. 30, no. 2, pp. 271–276, Feb. 2004.
- [72] P. Tortoli, A. Dallai, E. Boni, L. Francalanci, and S. Ricci, “An Automatic Angle Tracking Procedure for Feasible Vector Doppler Blood Velocity Measurements,” *Ultrasound Med. Biol.*, vol. 36, no. 3, pp. 488–496, Mar. 2010.
- [73] B. Y. S. Yiu, S. S. M. Lai, and A. C. H. Yu, “Vector Projectile Imaging: Time-Resolved Dynamic Visualization of Complex Flow Patterns,” *Ultrasound Med. Biol.*, vol. 40, no. 9, pp. 2295–2309, Sep. 2014.
- [74] M. E. Aderson, “Multi-dimensional velocity estimation with ultrasound using spatial quadrature,” *Ultrason. Ferroelectr. Freq. Control IEEE Trans. On*, vol. 45, no. 3, pp. 852–861, 1998.
- [75] J. A. Jensen and P. Munk, “A new method for estimation of velocity vectors,” *Ultrason. Ferroelectr. Freq. Control IEEE Trans. On*, vol. 45, no. 3, pp. 837–851, 1998.
- [76] P. Munk, “Estimation of the 2-D flow vector in ultrasonic imaging: a new approach,” *Masters Thesis Dep. Inf. Technol. Tech. Univ. Den.*, 1996.
- [77] J. A. Jensen and P. Munk, “An improved estimation and focusing scheme for vector velocity estimation,” in *1999 IEEE Ultrasonics Symposium, 1999. Proceedings, 1999*, vol. 2, pp. 1465–1470 vol.2.
- [78] M. Lenge, A. Ramalli, P. Tortoli, C. Cachard, and H. Liebgott, “Plane-wave transverse oscillation for high-frame-rate 2-D vector flow imaging,” *IEEE Trans. Ultrason. Ferroelectr. Freq. Control*, vol. 62, no. 12, pp. 2126–2137, Dec. 2015.

- [79] J. A. Jensen, "A new estimator for vector velocity estimation [medical ultrasonics]," *Ultrason. Ferroelectr. Freq. Control IEEE Trans. On*, vol. 48, no. 4, pp. 886–894, 2001.
- [80] O. Bonnefous, P. Pesque, and X. Bernard, "A New Velocity Estimator for Color Flow Mapping," in *IEEE 1986 Ultrasonics Symposium*, 1986, pp. 855–860.
- [81] S. G. Foster, P. M. Embree, and W. D. O'Brien, "Flow velocity profile via time-domain correlation: error analysis and computer simulation," *IEEE Trans. Ultrason. Ferroelectr. Freq. Control*, vol. 37, no. 3, pp. 164–175, May 1990.
- [82] J. A. Jensen, "Implementation of ultrasound time-domain cross-correlation blood velocity estimators," *Biomed. Eng. IEEE Trans. On*, vol. 40, no. 5, pp. 468–474, 1993.
- [83] J. A. Jensen and I. R. Lacasa, "Estimation of blood velocity vectors using transverse ultrasound beam focusing and cross-correlation," in *Ultrasonics Symposium, 1999. Proceedings. 1999 IEEE*, 1999, vol. 2, pp. 1493–1497.
- [84] J. A. Jensen and R. Bjerngaard, "Directional velocity estimation using focusing along the flow direction. II: experimental investigation," *IEEE Trans. Ultrason. Ferroelectr. Freq. Control*, vol. 50, no. 7, pp. 873–880, Jul. 2003.
- [85] J. A. Jensen and N. Oddershede, "Estimation of Velocity Vectors in Synthetic Aperture Ultrasound Imaging," *IEEE Trans. Med. Imaging*, vol. 25, no. 12, pp. 1637–1644, Dec. 2006.
- [86] J. Jensen and S. Nikolov, "Directional synthetic aperture flow imaging," *IEEE Trans. Ultrason. Ferroelectr. Freq. CONTROL*, vol. 51, no. 9, pp. 1107–1118, Sep. 2004.
- [87] J. Kortbek and J. Jensen, "Estimation of velocity vector angles using the directional cross-correlation method," *IEEE Trans. Ultrason. Ferroelectr. Freq. Control*, vol. 53, no. 11, pp. 2036–2049, Nov. 2006.
- [88] J. Flynn, R. Daigle, L. Pflugrath, and P. Kaczkowski, "High framerate vector velocity blood flow imaging using a single planewave transmission angle," 2012, pp. 323–325.
- [89] J. Udesen, F. Gran, K. Hansen, J. A. Jensen, C. Thomsen, and M. B. Nielsen, "High frame-rate blood vector velocity imaging using plane waves: simulations and preliminary experiments," *Ultrason. Ferroelectr. Freq. Control IEEE Trans. On*, vol. 55, no. 8, pp. 1729–1743, 2008.
- [90] L. N. Bohs, B. J. Geiman, M. E. Anderson, S. C. Gebhart, and G. E. Trahey, "Speckle tracking for multi-dimensional flow estimation," *Ultrasonics*, vol. 38, no. 1, pp. 369–375, 2000.
- [91] G. E. Trahey, J. W. Allison, and O. T. von Ramm, "Angle independent ultrasonic detection of blood flow," *Biomed. Eng. IEEE Trans. On*, no. 12, pp. 965–967, 1987.
- [92] I. A. Hein and W. D. O'Brien, "Current time-domain methods for assessing tissue motion by analysis from reflected ultrasound echoes-a review," *IEEE Trans. Ultrason. Ferroelectr. Freq. Control*, vol. 40, no. 2, pp. 84–102, Mar. 1993.
- [93] E. Yeom, K.-H. Nam, D.-G. Paeng, and S. J. Lee, "Improvement of ultrasound speckle image velocimetry using image enhancement techniques," *Ultrasonics*, May 2013.
- [94] R. J. Adrian, "Twenty years of particle image velocimetry," *Exp. Fluids*, vol. 39, no. 2, pp. 159–169, Jul. 2005.

- [95] C. E. Willert and M. Gharib, "Digital particle image velocimetry," *Exp. Fluids*, vol. 10, no. 4, pp. 181–193, 1991.
- [96] M. Crapper, T. Bruce, and C. Gouble, "Flow field visualization of sediment-laden flow using ultrasonic imaging," *Dyn. Atmospheres Oceans*, vol. 31, no. 1, pp. 233–245, 2000.
- [97] H. B. Kim, J. R. Hertzberg, and R. Shandas, "Development and validation of echo PIV," *Exp. Fluids*, vol. 36, no. 3, pp. 455–462, Mar. 2004.
- [98] L. Liu, H. Zheng, L. Williams, F. Zhang, R. Wang, J. Hertzberg, and R. Shandas, "Development of a custom-designed echo particle image velocimetry system for multi-component hemodynamic measurements: system characterization and initial experimental results," *Phys. Med. Biol.*, vol. 53, no. 5, pp. 1397–1412, Mar. 2008.
- [99] F. Zhang, C. Lanning, L. Mazzaro, A. J. Barker, P. E. Gates, W. D. Strain, J. Fulford, O. E. Gosling, A. C. Shore, N. G. Bellenger, B. Rech, J. Chen, J. Chen, and R. Shandas, "In Vitro and Preliminary In Vivo Validation of Echo Particle Image Velocimetry in Carotid Vascular Imaging," *Ultrasound Med. Biol.*, vol. 37, no. 3, pp. 450–464, Mar. 2011.
- [100] C. Poelma, R. M. E. van der Mijle, J. M. Mari, M.-X. Tang, P. D. Weinberg, and J. Westerweel, "Ultrasound imaging velocimetry: Toward reliable wall shear stress measurements," *Eur. J. Mech. - BFluids*, vol. 35, pp. 70–75, Sep. 2012.
- [101] J. Westerdale, M. Belohlavek, E. M. McMahon, P. Jiamsripong, J. J. Heys, and M. Milano, "Flow Velocity Vector Fields by Ultrasound Particle Imaging Velocimetry In Vitro Comparison With Optical Flow Velocimetry," *J. Ultrasound Med.*, vol. 30, no. 2, pp. 187–195, 2011.
- [102] M. Raffel, Ed., *Particle image velocimetry: a practical guide*, 2nd ed. Heidelberg ; New York: Springer, 2007.
- [103] H. Nobach and M. Honkanen, "Two-dimensional Gaussian regression for sub-pixel displacement estimation in particle image velocimetry or particle position estimation in particle tracking velocimetry," *Exp. Fluids*, vol. 38, no. 4, pp. 511–515, Mar. 2005.
- [104] H. Nobach, N. Damaschke, and C. Tropea, "High-precision sub-pixel interpolation in particle image velocimetry image processing," *Exp. Fluids*, vol. 39, no. 2, pp. 299–304, Jun. 2005.
- [105] T. Roesgen, "Optimal subpixel interpolation in particle image velocimetry," *Exp. Fluids*, vol. 35, no. 3, pp. 252–256, Jul. 2003.
- [106] S. T. Wereley and C. D. Meinhart, "Second-order accurate particle image velocimetry," *Exp. Fluids*, vol. 31, no. 3, pp. 258–268, 2001.
- [107] J. Westerweel, D. Dabiri, and M. Gharib, "The effect of a discrete window offset on the accuracy of cross-correlation analysis of digital PIV recordings," *Exp. Fluids*, vol. 23, no. 1, pp. 20–28, 1997.
- [108] F. Scarano and M. L. Riethmuller, "Iterative multigrid approach in PIV image processing with discrete window offset," *Exp. Fluids*, vol. 26, no. 6, pp. 513–523, 1999.
- [109] K.-H. Park, J.-W. Son, W.-J. Park, S.-H. Lee, U. Kim, J.-S. Park, D.-G. Shin, Y.-J. Kim, J.-H. Choi, H. Houle, M. A. Vannan, and G.-R. Hong, "Characterization of the Left Atrial Vortex Flow by Two-Dimensional Transesophageal Contrast

- Echocardiography Using Particle Image Velocimetry,” *Ultrasound Med. Biol.*, vol. 39, no. 1, pp. 62–71, Jan. 2013.
- [110] L. Niu, M. Qian, K. Wan, W. Yu, Q. Jin, T. Ling, S. Gao, and H. Zheng, “Ultrasonic particle image velocimetry for improved flow gradient imaging: algorithms, methodology and validation,” *Phys. Med. Biol.*, vol. 55, no. 7, pp. 2103–2120, Apr. 2010.
- [111] J. Westerweel and F. Scarano, “Universal outlier detection for PIV data,” *Exp. Fluids*, vol. 39, no. 6, pp. 1096–1100, Aug. 2005.
- [112] C. Willert, “Adaptive PIV processing based on ensemble correlation,” in *14th international symposium on applications of laser techniques to fluid mechanics*, July, 2008, pp. 07–10.
- [113] C. D. Meinhart, S. T. Wereley, and J. G. Santiago, “A PIV Algorithm for Estimating Time-Averaged Velocity Fields,” *Tech. Pap.*, vol. 285, 2000.
- [114] C. Poelma, J. M. Mari, N. Foin, M.-X. Tang, R. Krams, C. G. Caro, P. D. Weinberg, and J. Westerweel, “3D Flow reconstruction using ultrasound PIV,” *Exp. Fluids*, vol. 50, no. 4, pp. 777–785, Nov. 2009.
- [115] A. Kheradvar, H. Houle, G. Pedrizzetti, G. Tonti, T. Belcik, M. Ashraf, J. R. Lindner, M. Gharib, and D. Sahn, “Echocardiographic Particle Image Velocimetry: A Novel Technique for Quantification of Left Ventricular Blood Vorticity Pattern,” *J. Am. Soc. Echocardiogr.*, vol. 23, no. 1, pp. 86–94, Jan. 2010.
- [116] M. Qian, L. Niu, Y. Wang, B. Jiang, Q. Jin, C. Jiang, and H. Zheng, “Measurement of flow velocity fields in small vessel-mimic phantoms and vessels of small animals using micro ultrasonic particle image velocimetry (micro-EPIV),” *Phys. Med. Biol.*, vol. 55, no. 20, pp. 6069–6088, Oct. 2010.
- [117] G.-R. Hong, G. Pedrizzetti, G. Tonti, P. Li, Z. Wei, J. K. Kim, A. Baweja, S. Liu, N. Chung, H. Houle, J. Narula, and M. A. Vannan, “Characterization and Quantification of Vortex Flow in the Human Left Ventricle by Contrast Echocardiography Using Vector Particle Image Velocimetry,” *JACC Cardiovasc. Imaging*, vol. 1, no. 6, pp. 705–717, Nov. 2008.
- [118] P. P. Sengupta, G. Pedrizzetti, and J. Narula, “Multiplanar Visualization of Blood Flow Using Echocardiographic Particle Imaging Velocimetry,” *JACC Cardiovasc. Imaging*, vol. 5, no. 5, pp. 566–569, May 2012.
- [119] C. Prinz, R. Faludi, A. Walker, M. Amzulescu, H. Gao, T. Uejima, A. G. Fraser, and J.-U. Voigt, “Can echocardiographic particle image velocimetry correctly detect motion patterns as they occur in blood inside heart chambers? A validation study using moving phantoms,” *Cardiovasc. Ultrasound*, vol. 10, no. 1, p. 24, 2012.
- [120] B. Zhou, K. H. Fraser, C. Poelma, J.-M. Mari, R. J. Eckersley, P. D. Weinberg, and M.-X. Tang, “Ultrasound Imaging Velocimetry: Effect of Beam Sweeping on Velocity Estimation,” *Ultrasound Med. Biol.*, vol. 39, no. 9, pp. 1672–1681, Sep. 2013.
- [121] C. H. Leow, E. Bazigou, R. J. Eckersley, A. C. H. Yu, P. D. Weinberg, and M.-X. Tang, “Flow velocity mapping using high frame-rate plane wave ultrasound and microbubble contrast agents,” 2015.

- [122] P. F. Davies, “Hemodynamic shear stress and the endothelium in cardiovascular pathophysiology,” *Nat. Clin. Pract. Cardiovasc. Med.*, vol. 6, no. 1, pp. 16–26, Nov. 2008.
- [123] R. S. Reneman, T. Arts, and A. P. G. Hoeks, “Wall Shear Stress -an Important Determinant of Endothelial Cell Function and Structure - in the Arterial System in vivo,” *J. Vasc. Res.*, vol. 43, no. 3, pp. 251–269, 2006.
- [124] P. Yim, K. DeMarco, M. A. Castro, and J. Cebral, “Characterization of Shear Stress on the Wall of the Carotid Artery Using Magnetic Resonance Imaging and Computational Fluid Dynamics,” vol. 113, 2005, pp. 412–442.
- [125] P. Hoskins, “Peak velocity estimation in arterial stenosis models using colour vector Doppler,” *Ultrasound Med. Biol.*, vol. 23, no. 6, pp. 889–897, 1997.
- [126] R. Steel, K. V. Ramnarine, F. Davidson, P. J. Fish, and P. R. Hoskins, “Angle-independent estimation of maximum velocity through stenoses using vector Doppler ultrasound,” *Ultrasound Med. Biol.*, vol. 29, no. 4, pp. 575–584, Apr. 2003.
- [127] D. H. Evans and P. N. T. Wells, “Colour flow and motion imaging,” *Proc. Inst. Mech. Eng. [H]*, vol. 224, no. 2, pp. 241–253, Feb. 2010.
- [128] A. Pastorelli, G. Torricelli, M. Scabia, E. Biagi, and L. Masotti, “A Real-Time 2-D Vector Doppler System for Clinical Experimentation,” *IEEE Trans. Med. Imaging*, vol. 27, no. 10, pp. 1515–1524, Oct. 2008.
- [129] S. Ohtsuki and M. Tanaka, “The flow velocity distribution from the Doppler information on a plane in three-dimensional flow,” *J. Vis.*, vol. 9, no. 1, pp. 69–82, 2006.
- [130] T. Uejima, A. Koike, H. Sawada, T. Aizawa, S. Ohtsuki, M. Tanaka, T. Furukawa, and A. G. Fraser, “A New Echocardiographic Method for Identifying Vortex Flow in the Left Ventricle: Numerical Validation,” *Ultrasound Med. Biol.*, vol. 36, no. 5, pp. 772–788, May 2010.
- [131] M. M. Pedersen, M. J. Pihl, P. Haugaard, K. L. Hansen, T. Lange, L. Lönn, M. B. Nielsen, and J. A. Jensen, “Novel Flow Quantification of the Carotid Bulb and the Common Carotid Artery with Vector Flow Ultrasound,” *Ultrasound Med. Biol.*, vol. 40, no. 11, pp. 2700–2706, Nov. 2014.
- [132] J. Udesen and J. A. Jensen, “Investigation of transverse oscillation method,” *Ultrason. Ferroelectr. Freq. Control IEEE Trans. On*, vol. 53, no. 5, pp. 959–971, 2006.
- [133] D. H. Simpson, C. T. Chin, and P. N. Burns, “Pulse inversion Doppler: a new method for detecting nonlinear echoes from microbubble contrast agents,” *Ultrason. Ferroelectr. Freq. Control IEEE Trans. On*, vol. 46, no. 2, pp. 372–382, 1999.
- [134] Charles Tremblay-Darveau, R. Williams, L. Milot, M. Bruce, and P. N. Burns, “Combined perfusion and doppler imaging using plane-wave nonlinear detection and microbubble contrast agents,” *IEEE Trans. Ultrason. Ferroelectr. Freq. Control*, vol. 61, no. 12, pp. 1988–2000, Dec. 2014.
- [135] K.-H. Nam, E. Yeom, H. Ha, and S.-J. Lee, “Velocity field measurements of valvular blood flow in a human superficial vein using high-frequency ultrasound speckle image velocimetry,” *Int. J. Cardiovasc. Imaging*, vol. 28, no. 1, pp. 69–77, Dec. 2010.
- [136] A. Swillens, P. Segers, H. Torp, and L. Lovstakken, “Two-dimensional blood velocity estimation with ultrasound: speckle tracking versus crossed-beam vector doppler based

- on flow simulations in a carotid bifurcation model,” *IEEE Trans. Ultrason. Ferroelectr. Freq. Control*, vol. 57, no. 2, pp. 327–339, Feb. 2010.
- [137] J. A. Jensen, S. I. Nikolov, K. L. Gammelmark, and M. H. Pedersen, “Synthetic aperture ultrasound imaging,” *Ultrasonics*, vol. 44, pp. e5–e15, Dec. 2006.
- [138] I. K. Ekroll, A. Swillens, P. Segers, T. Dahl, H. Torp, and L. Lovstakken, “Simultaneous quantification of flow and tissue velocities based on multi-angle plane wave imaging,” *IEEE Trans. Ultrason. Ferroelectr. Freq. Control*, vol. 60, no. 4, Apr. 2013.
- [139] M. Lenge, A. Ramalli, A. Cellai, P. Tortoli, C. Cachard, and H. Liebgott, “A new method for 2D-vector blood flow imaging based on unconventional beamforming techniques,” in *Acoustics, Speech and Signal Processing (ICASSP), 2014 IEEE International Conference on*, 2014, pp. 5125–5129.
- [140] P. S. Sheeran, S. Luois, P. A. Dayton, and T. O. Matsunaga, “Formulation and Acoustic Studies of a New Phase-Shift Agent for Diagnostic and Therapeutic Ultrasound,” *Langmuir*, vol. 27, no. 17, pp. 10412–10420, Sep. 2011.
- [141] C. A. Sennoga, J. S. M. Yeh, J. Alter, E. Stride, P. Nihoyannopoulos, J. M. Seddon, D. O. Haskard, J. V. Hajnal, M.-X. Tang, and R. J. Eckersley, “Evaluation of Methods for Sizing and Counting of Ultrasound Contrast Agents,” *Ultrasound Med. Biol.*, vol. 38, no. 5, pp. 834–845, May 2012.
- [142] H. Mulvana, E. Stride, M.-X. Tang, J. V. Hajnal, and R. J. Eckersley, “The Influence of Gas Saturation on Microbubble Stability,” *Ultrasound Med. Biol.*, vol. 38, no. 6, pp. 1097–1100, Jun. 2012.
- [143] M. Tang and R. Eckersley, “Nonlinear propagation of ultrasound through microbubble contrast agents and implications for imaging,” *IEEE Trans. Ultrason. Ferroelectr. Freq. Control*, vol. 53, no. 12, pp. 2406–2415, Dec. 2006.
- [144] M.-X. Tang, N. Kamiyama, and R. J. Eckersley, “Effects of Nonlinear Propagation in Ultrasound Contrast Agent Imaging,” *Ultrasound Med. Biol.*, vol. 36, no. 3, pp. 459–466, Mar. 2010.
- [145] R. J. Adrian, “Particle-imaging techniques for experimental fluid mechanics,” *Annu. Rev. Fluid Mech.*, vol. 23, no. 1, pp. 261–304, 1991.
- [146] D. McDonald, *Blood flow in arteries*, 2nd Edn. Edward Arnold, London, 1974.
- [147] S. S. M. Lai, B. Y. S. Yiu, A. K. K. Poon, and A. C. H. Yu, “Design of Anthropomorphic Flow Phantoms Based on Rapid Prototyping of Compliant Vessel Geometries,” *Ultrasound Med. Biol.*, vol. 39, no. 9, pp. 1654–1664, Sep. 2013.
- [148] K. V. Ramnarine, D. K. Nassiri, P. R. Hoskins, and J. Lubbers, “Validation of a new blood-mimicking fluid for use in Doppler flow test objects,” *Ultrasound Med. Biol.*, vol. 24, no. 3, pp. 451–459, 1998.
- [149] P. R. Hoskins, “Estimation of blood velocity, volumetric flow and wall shear rate using Doppler ultrasound,” *Ultrasound*, vol. 19, no. 3, pp. 120–129, Aug. 2011.
- [150] P. Hoskins, “Accuracy of maximum velocity estimates made using Doppler ultrasound systems,” *Br. J. Radiol.*, vol. 69, no. 818, pp. 172–177, 1996.
- [151] P. Tortoli, F. Guidi, R. Mori, and H. J. Vos, “The use of microbubbles in Doppler ultrasound studies,” *Med. Biol. Eng. Comput.*, vol. 47, no. 8, pp. 827–838, Aug. 2009.

- [152] X. He and D. N. Ku, "Unsteady entrance flow development in a straight tube," *J. Biomech. Eng.*, vol. 116, no. 3, pp. 355–360, 1994.
- [153] D. N. Ku, "Blood flow in arteries," *Annu. Rev. Fluid Mech.*, vol. 29, no. 1, pp. 399–434, 1997.
- [154] T. Yamaguchi, S. Kikkawa, and K. Parker, "Simulation of nonstationary spectral analysis of turbulence in the aorta using a modified autoregressive or maximum entropy (AR/ME) method," *Med. Biol. Eng. Comput.*, vol. 25, no. 5, pp. 533–542, 1987.
- [155] U. Gülan, B. Lüthi, M. Holzner, A. Liberzon, A. Tsinober, and W. Kinzelbach, "Experimental study of aortic flow in the ascending aorta via Particle Tracking Velocimetry," *Exp. Fluids*, vol. 53, no. 5, pp. 1469–1485, Nov. 2012.
- [156] R. Lencioni, *Enhancing the role of ultrasound with contrast agents*. Milan; Berlin: Springer, 2006.
- [157] R. Willink and D. H. Evans, "Volumetric blood flow calculation using a narrow ultrasound beam," *Ultrasound Med. Biol.*, vol. 21, no. 2, pp. 203–216, 1995.
- [158] P. Tortoli, E. Boni, M. Corsi, M. Arditi, and P. Frinking, "Different effects of microbubble destruction and translation in Doppler measurements," *Ultrason. Ferroelectr. Freq. Control IEEE Trans. On*, vol. 52, no. 7, pp. 1183–1188, 2005.
- [159] B. Denarie, T. A. Tangen, I. K. Ekroll, N. Rolim, H. Torp, T. Bjastad, and L. Lovstakken, "Coherent Plane Wave Compounding for Very High Frame Rate Ultrasonography of Rapidly Moving Targets," *IEEE Trans. Med. Imaging*, vol. 32, no. 7, pp. 1265–1276, Jul. 2013.
- [160] P. Hoskins, "Review of the design and use of flow phantoms," in *Testing of Doppler ultrasound equipment*, Institute of Physical Sciences in Medicine, York, UK, 1994, pp. 12–29.
- [161] P. Hoskins and K. Ramnarine, "Doppler test devices," *Doppler Ultrasound Phys. Instrum. Signal Process. II Ed Chichester UK Wiley*, vol. 4, no. 18, p. 2010, 2000.
- [162] A. J. Y. Chee, C. K. Ho, B. Y. S. Yiu, and A. C. H. Yu, "Walled Carotid Bifurcation Phantoms for Imaging Investigations of Vessel Wall Motion and Blood Flow Dynamics," *IEEE Trans. Ultrason. Ferroelectr. Freq. Control*, vol. PP, no. 99, pp. 1–1, 2016.
- [163] C. R. Hazard and G. R. Lockwood, "Effects of motion on a synthetic aperture beamformer for real-time 3D ultrasound," in *1999 IEEE Ultrasonics Symposium, 1999. Proceedings*, 1999, vol. 2, pp. 1221–1224 vol.2.
- [164] Wang Jing and Lu Jian-yu, "Motion Artifacts of Extended High Frame Rate Imaging," *IEEE Trans. Ultrason. Ferroelectr. Freq. Control*, vol. 54, no. 7, pp. 1303–1315, Jul. 2007.
- [165] N. Oddershede and J. Jensen, "Effects Influencing Focusing in Synthetic Aperture Vector Flow Imaging," *IEEE Trans. Ultrason. Ferroelectr. Freq. Control*, vol. 54, no. 9, pp. 1811–1825, Sep. 2007.
- [166] M. Karaman, H. S. Bilge, and M. O'Donnell, "Adaptive multi-element synthetic aperture imaging with motion and phase aberration correction," *IEEE Trans. Ultrason. Ferroelectr. Freq. Control*, vol. 45, no. 4, pp. 1077–1087, Jul. 1998.

- [167] K. S. Kim, J. S. Hwang, J. S. Jeong, and T. K. Song, "An Efficient Motion Estimation and Compensation Method for Ultrasound Synthetic Aperture Imaging," *Ultrason. Imaging*, vol. 24, no. 2, pp. 81–99, Apr. 2002.
- [168] D. H. Evans and W. N. McDicken, *Doppler ultrasound: physics, instrumentation and signal processing*. John Wiley & Sons, 2000.
- [169] J. R. Womersley, "Method for the calculation of velocity, rate of flow and viscous drag in arteries when the pressure gradient is known," *J. Physiol.*, vol. 127, no. 3, pp. 553–563, 1955.
- [170] D. H. Evans, "Some aspects of the relationship between instantaneous volumetric blood flow and continuous wave doppler ultrasound recordings—III. The calculation of doppler power spectra from mean velocity waveforms, and the results of processing these spectra with maximum, mean, and rms frequency processors," *Ultrasound Med. Biol.*, vol. 8, no. 6, pp. 617–623, Jan. 1982.
- [171] J. Jensen, "Field: A Program for Simulating Ultrasound Systems," presented at the 10th Nordic-Baltic Conference on Biomedical Imaging, 1996.
- [172] J. A. Jensen and N. B. Svendsen, "Calculation of pressure fields from arbitrarily shaped, apodized, and excited ultrasound transducers," *Ultrason. Ferroelectr. Freq. Control IEEE Trans. On*, vol. 39, no. 2, pp. 262–267, 1992.
- [173] P. R. Stepanishen, "The Time-Dependent Force and Radiation Impedance on a Piston in a Rigid Infinite Planar Baffle," *J. Acoust. Soc. Am.*, vol. 49, no. 3, pp. 841–849, 1971.
- [174] G. E. Topholme, "Generation of acoustic pulses by baffled plane pistons," *Mathematika*, vol. 16, no. 209–224, p. 149, 1969.
- [175] J. M. Thijssen, "Ultrasonic speckle formation, analysis and processing applied to tissue characterization," *Pattern Recognit. Lett.*, vol. 24, no. 4–5, pp. 659–675, Feb. 2003.
- [176] A. Stanziola, M. Toulemonde, Y. O. Yildiz, R. J. Eckersley, and M.-X. Tang, "Ultrasound Imaging with Microbubbles [Life Sciences]," *IEEE Signal Process. Mag.*, vol. 33, no. 2, pp. 111–117, Mar. 2016.
- [177] T. L. Poepping, R. N. Rankin, and D. W. Holdsworth, "Flow Patterns in Carotid Bifurcation Models Using Pulsed Doppler Ultrasound: Effect of Concentric vs. Eccentric Stenosis on Turbulence and Recirculation," *Ultrasound Med. Biol.*, vol. 36, no. 7, pp. 1125–1134, Jul. 2010.
- [178] A. Swillens, L. Lovstakken, J. Kips, H. Torp, and P. Segers, "Ultrasound simulation of complex flow velocity fields based on computational fluid dynamics," *IEEE Trans. Ultrason. Ferroelectr. Freq. Control*, vol. 56, no. 3, pp. 546–556, Mar. 2009.
- [179] F. Varray, C. Cachard, P. Tortoli, and O. Basset, "Nonlinear radio frequency image simulation for harmonic imaging: Creanuis," in *Ultrasonics Symposium (IUS), 2010 IEEE*, 2010, pp. 2179–2182.
- [180] D. Katritsis, L. Kaiktsis, A. Chaniotis, J. Pantos, E. P. Efstathopoulos, and V. Marmarelis, "Wall Shear Stress: Theoretical Considerations and Methods of Measurement," *Prog. Cardiovasc. Dis.*, vol. 49, no. 5, pp. 307–329, Mar. 2007.
- [181] T. G. Papaioannou and C. Stefanadis, "Vascular wall shear stress: basic principles and methods," *Hell. J Cardiol*, vol. 46, no. 1, pp. 9–15, 2005.

- [182] J. P. Mynard, B. A. Wasserman, and D. A. Steinman, "Errors in the estimation of wall shear stress by maximum Doppler velocity," *Atherosclerosis*, vol. 227, no. 2, pp. 259–266, Apr. 2013.
- [183] C. P. Cheng, D. Parker, and C. A. Taylor, "Quantification of Wall Shear Stress in Large Blood Vessels Using Lagrangian Interpolation Functions with Cine Phase-Contrast Magnetic Resonance Imaging," *Ann. Biomed. Eng.*, vol. 30, no. 8, pp. 1020–1032, Sep. 2002.
- [184] A. M. Masaryk, R. Frayne, O. Unal, E. Krupinski, and C. M. Strother, "In Vitro and In Vivo Comparison of Three MR Measurement Methods for Calculating Vascular Shear Stress in the Internal Carotid Artery," *Am. J. Neuroradiol.*, vol. 20, no. 2, pp. 237–245, Feb. 1999.
- [185] A. F. Stalder, M. F. Russe, A. Frydrychowicz, J. Bock, J. Hennig, and M. Markl, "Quantitative 2D and 3D phase contrast MRI: Optimized analysis of blood flow and vessel wall parameters," *Magn. Reson. Med.*, vol. 60, no. 5, pp. 1218–1231, Nov. 2008.
- [186] A. Savitzky and M. J. Golay, "Smoothing and differentiation of data by simplified least squares procedures.," *Anal. Chem.*, vol. 36, no. 8, pp. 1627–1639, 1964.
- [187] S. Lankton and A. Tannenbaum, "Localizing Region-Based Active Contours," *IEEE Trans. Image Process.*, vol. 17, no. 11, pp. 2029–2039, Nov. 2008.
- [188] J. Charonko, S. Karri, J. Schmieg, S. Prabhu, and P. Vlachos, "In vitro, time-resolved PIV comparison of the effect of stent design on wall shear stress," *Ann. Biomed. Eng.*, vol. 37, no. 7, pp. 1310–1321, Jul. 2009.
- [189] Kundu, Pijush K., "Chapter 2 - Cartesian Tensors," in *Fluid Mechanics*, Fifth Edition., I. M. Cohen and D. R. Dowling, Eds. Boston: Academic Press, 2012, pp. 39–64.
- [190] Z. Lou, W.-J. Yang, and P. D. Stein, "Errors in the estimation of arterial wall shear rates that result from curve fitting of velocity profiles," *J. Biomech.*, vol. 26, no. 4, pp. 383–390, Apr. 1993.
- [191] S. Kefayati, J. S. Milner, D. W. Holdsworth, and T. L. Poepping, "In Vitro Shear Stress Measurements Using Particle Image Velocimetry in a Family of Carotid Artery Models: Effect of Stenosis Severity, Plaque Eccentricity, and Ulceration," *PLoS ONE*, vol. 9, no. 7, p. e98209, Jul. 2014.
- [192] D. A. Steinman, T. L. Poepping, M. Tambasco, R. N. Rankin, and D. W. Holdsworth, "Flow patterns at the stenosed carotid bifurcation: effect of concentric versus eccentric stenosis," *Ann. Biomed. Eng.*, vol. 28, no. 4, pp. 415–423, 2000.
- [193] R. S. Fatemi and S. E. Rittgers, "Derivation of Shear Rates From Near-Wall LDA Measurements Under Steady and Pulsatile Flow Conditions," *J. Biomech. Eng.*, vol. 116, no. 3, pp. 361–368, Aug. 1994.
- [194] H.-B. Kim, J. Hertzberg, C. Lanning, and R. Shandas, "Noninvasive measurement of steady and pulsating velocity profiles and shear rates in arteries using echo PIV: in vitro validation studies," *Ann. Biomed. Eng.*, vol. 32, no. 8, pp. 1067–1076, 2004.
- [195] S. Ricci, A. Swillens, A. Ramalli, P. Segers, and P. Tortoli, "Wall Shear Rate Measurement: Validation of a New Method through Multi-Physics Simulations," *IEEE Trans. Ultrason. Ferroelectr. Freq. Control*, vol. PP, no. 99, pp. 1–1, 2016.
- [196] C. H. Leow, F. Iori, R. Corbett, N. Duncan, C. Caro, P. Vincent, and M.-X. Tang, "Microbubble Void Imaging: A Non-invasive Technique for Flow Visualisation and

- Quantification of Mixing in Large Vessels Using Plane Wave Ultrasound and Controlled Microbubble Contrast Agent Destruction,” *Ultrasound Med. Biol.*
- [197] M. H. Friedman, O. J. Deters, F. F. Mark, C. Brent Barger, and G. M. Hutchins, “Arterial geometry affects hemodynamics: A potential risk factor for atherosclerosis,” *Atherosclerosis*, vol. 46, no. 2, pp. 225–231, Feb. 1983.
- [198] D. N. Ku and D. P. Giddens, “Pulsatile flow in a model carotid bifurcation,” *Arterioscler. Thromb. Vasc. Biol.*, vol. 3, no. 1, pp. 31–39, 1983.
- [199] S. G. Carlier, “Augmentation of Wall Shear Stress Inhibits Neointimal Hyperplasia After Stent Implantation: Inhibition Through Reduction of Inflammation?,” *Circulation*, vol. 107, no. >21, pp. 2741–2746, Jun. 2003.
- [200] C. G. Caro, A. Seneviratne, K. B. Heraty, C. Monaco, M. G. Burke, R. Krams, C. C. Chang, G. Coppola, and P. Gilson, “Intimal hyperplasia following implantation of helical-centreline and straight-centreline stents in common carotid arteries in healthy pigs: influence of intraluminal flow,” *J. R. Soc. Interface*, vol. 10, no. 89, pp. 20130578–20130578, Oct. 2013.
- [201] C. Caro, N. Cheshire, D. Ellis, M. Cerini, and S. Cremers, “Implications of 3D vascular geometry,” 2006, pp. S299–S299.
- [202] C. G. Caro, N. Watkins, D. J. Doorly, S. J. Sherwin, and J. Peiro, “Influence of non-planar geometry on flow separation,” *J. Physiol. Camb.*, vol. 513P, p. 2P–3P, Dec. 1998.
- [203] M. H. Friedman and Z. Ding, “Relation between the structural asymmetry of coronary branch vessels and the angle at their origin,” *J. Biomech.*, vol. 31, no. 3, pp. 273–278, 1997.
- [204] C. G. Caro, D. J. Doorly, M. Tarnawski, K. T. Scott, Q. Long, and C. L. Dumoulin, “Non-Planar Curvature and Branching of Arteries and Non-Planar-Type Flow,” *Proc. R. Soc. Math. Phys. Eng. Sci.*, vol. 452, no. 1944, pp. 185–197, Jan. 1996.
- [205] C. G. Caro, N. J. Cheshire, and N. Watkins, “Preliminary comparative study of small amplitude helical and conventional ePTFE arteriovenous shunts in pigs,” *J. R. Soc. Interface*, vol. 2, no. 3, pp. 261–266, Jun. 2005.
- [206] T. V. How, R. K. Fisher, J. A. Brennan, and P. L. Harris, “Swirling flow pattern in a non-planar model of an interposition vein cuff anastomosis,” *Med. Eng. Phys.*, vol. 28, no. 1, pp. 27–35, Jan. 2006.
- [207] T. Shinke, K. Robinson, P. Gilson, M. Bruke, N. Cheshire, and C. Caro, “Novel helical stent design elicits spiral blood flow pattern and inhibits neointima formation in porcine carotid arteries,” 2007, p. 186L–186L.
- [208] E. T. Petersen, I. Zimine, Y.-C. L. Ho, and X. Golay, “Non-invasive measurement of perfusion: a critical review of arterial spin labelling techniques,” *Br. J. Radiol.*, vol. 79, no. 944, pp. 688–701, Aug. 2006.
- [209] P. R. Hoskins, “Simulation and Validation of Arterial Ultrasound Imaging and Blood Flow,” *Ultrasound Med. Biol.*, vol. 34, no. 5, pp. 693–717, May 2008.
- [210] R. Y. Chiao, L. Y. Mo, A. L. Hall, S. C. Miller, and K. E. Thomenius, “B-mode blood flow (B-flow) imaging,” in *Ultrasonics Symposium, 2000 IEEE*, 2000, vol. 2, pp. 1469–1472.

- [211] L. Lovstakken, S. Bjaerum, D. Martens, and H. Torp, "Blood flow imaging—a new real-time, flow imaging technique," *Ultrason. Ferroelectr. Freq. Control IEEE Trans. On*, vol. 53, no. 2, pp. 289–299, 2006.
- [212] P. R. Hoskins and P. N. T. Wells, "Haemodynamics and blood flow measured using ultrasound imaging," *Proc. Inst. Mech. Eng. [H]*, vol. 224, no. 2, pp. 255–271, Feb. 2010.
- [213] D. Cosgrove and N. Lassau, "Imaging of perfusion using ultrasound," *Eur. J. Nucl. Med. Mol. Imaging*, vol. 37, no. S1, pp. 65–85, Jul. 2010.
- [214] J. R. Lindner, "Molecular imaging of cardiovascular disease with contrast-enhanced ultrasonography," *Nat. Rev. Cardiol.*, vol. 6, no. 7, pp. 475–481, Jul. 2009.
- [215] V. Sboros, M.-X. Tang, and P. N. T. Wells, "The assessment of microvascular flow and tissue perfusion using ultrasound imaging," *Proc. Inst. Mech. Eng. [H]*, vol. 224, no. 2, pp. 273–290, Feb. 2010.
- [216] K. Ferrara, R. Pollard, and M. Borden, "Ultrasound Microbubble Contrast Agents: Fundamentals and Application to Gene and Drug Delivery," *Annu. Rev. Biomed. Eng.*, vol. 9, no. 1, pp. 415–447, Aug. 2007.
- [217] A. N. Cookson, D. J. Doorly, and S. J. Sherwin, "Mixing Through Stirring of Steady Flow in Small Amplitude Helical Tubes," *Ann. Biomed. Eng.*, vol. 37, no. 4, pp. 710–721, Apr. 2009.
- [218] J. M. Tarbell, "Mass Transport in Arteries and The Localization of Atherosclerosis," *Annu. Rev. Biomed. Eng.*, vol. 5, no. 1, pp. 79–118, Aug. 2003.
- [219] M.-X. Tang, H. Mulvana, T. Gauthier, A. K. P. Lim, D. O. Cosgrove, R. J. Eckersley, and E. Stride, "Quantitative contrast-enhanced ultrasound imaging: a review of sources of variability," *Interface Focus*, vol. 1, no. 4, pp. 520–539, Aug. 2011.
- [220] C. G. Caro, T. J. Pedley, R. C. Schroter, and W. A. Seed, *The Mechanics of the Circulation*, 2nd ed. Cambridge University Press, 2012.
- [221] F. and D. A. FDA, *Guidance for industry and FDA staff—information for manufacturers seeking marketing clearance of diagnostic ultrasound systems and transducers. 2008*. Accessed, 2010.
- [222] S. Garg, B. R. Sharma, K. Cohen, and M. Kumar, "A Proper Orthogonal Decomposition based algorithm for smoke filtering in videos," in *American Control Conference (ACC), 2013*, 2013, pp. 3529–3534.
- [223] P. Holmes, J. L. Lumley, and G. Berkooz, *Turbulence, coherent structures, dynamical systems and symmetry*. Cambridge university press, 1998.
- [224] L. Sirovich, "Turbulence and the dynamics of coherent structures. I-Coherent structures. II-Symmetries and transformations. III-Dynamics and scaling," *Q. Appl. Math.*, vol. 45, pp. 561–571, 1987.
- [225] M.-X. Tang, J. Loughran, E. Stride, D. Zhang, and R. J. Eckersley, "Effect of bubble shell nonlinearity on ultrasound nonlinear propagation through microbubble populations," *J. Acoust. Soc. Am.*, vol. 129, no. 3, pp. EL76–EL82, 2011.
- [226] U. F. and D. A. FDA, "Information for manufacturers seeking marketing clearance of diagnostic ultrasound systems and transducers," *Cent. Devices Radiol. Health FDA*, Sep. 2008.

- [227] R. Fåhræus and T. Lindqvist, “The Viscosity of the Blood in Narrow Capillary Tubes,” *Am. J. Physiol. -- Leg. Content*, vol. 96, no. 3, pp. 562–568, Mar. 1931.
- [228] D. A. Fedosov and G. Gompper, “White blood cell margination in microcirculation,” *Soft Matter*, vol. 10, no. 17, pp. 2961–2970, 2014.
- [229] H. Zhao and E. S. G. Shaqfeh, “Numerical simulation of the margination of platelets in the microvasculature,” *Cent. Turbul. Res. Annu. Res. Briefs*, pp. 365–374, 2010.
- [230] C. H. Leow, R. J. Eckersley, A. C. H. Yu, and M.-X. Tang, “Plane Wave Ultrasound Imaging and Tracking of Microbubbles in Large Vessels for Flow Quantification: Methods and Initial Evaluation on a Carotid Bifurcation Phantom,” presented at the 20th European symposium on Ultrasound Contrast Imaging, Rotterdam, 2015, pp. 94–96.
- [231] G. Montaldo, E. Macé, I. Cohen, J. Berckhoff, M. Tanter, and M. Fink, “Ultrafast compound doppler imaging: a new approach of doppler flow analysis,” in *Biomedical Imaging: From Nano to Macro, 2010 IEEE International Symposium on*, 2010, pp. 324–327.
- [232] K. Jambunathan, X. Ju, B. Dobbins, and S. Ashforth-Frost, “An improved cross correlation technique for particle image velocimetry,” *Meas. Sci. Technol.*, vol. 6, no. 5, p. 507, 1995.
- [233] C. Wachinger, T. Klein, and N. Navab, “The 2D analytic signal for envelope detection and feature extraction on ultrasound images,” *Med. Image Anal.*, vol. 16, no. 6, pp. 1073–1084, Aug. 2012.
- [234] L. Marple, “Computing the discrete-time analytic signal via FFT,” *IEEE Trans. Signal Process.*, vol. 47, no. 9, pp. 2600–2603, Sep. 1999.
- [235] A. R. Selfridge, G. S. Kino, and B. T. Khuri-Yakub, “A theory for the radiation pattern of a narrow-strip acoustic transducer,” *Appl. Phys. Lett.*, vol. 37, no. 1, pp. 35–36, Jul. 1980.
- [236] Y. Tasinkevych, A. Nowicki, and I. Trots, “Element directivity influence in the synthetic focusing algorithm for ultrasound imaging.”
- [237] C. Nvidia, “Programming Guide Version 2.3. 1,” *Nvidia Corp.*, 2009.
- [238] C. U. D. A. Nvidia, “CUFFT library version 2.1,” 2008.
- [239] M. Harris, “Optimizing parallel reduction in CUDA,” *NVIDIA Dev. Technol.*, vol. 2, no. 4, 2007.
- [240] T. Chernyakova and Y. C. Eldar, “Fourier domain beamforming: The path to compressed ultrasound imaging,” *ArXiv Prepr. ArXiv13076345*, 2013.
- [241] M. Correia, J. Provost, M. Tanter, and M. Pernot, “4D ultrafast ultrasound flow imaging: *in vivo* quantification of arterial volumetric flow rate in a single heartbeat,” *Phys. Med. Biol.*, vol. 61, no. 23, pp. L48–L61, Dec. 2016.
- [242] J. Provost, C. Papadacci, J. E. Arango, M. Imbault, M. Fink, J.-L. Gennisson, M. Tanter, and M. Pernot, “3D ultrafast ultrasound imaging *in vivo*,” *Phys. Med. Biol.*, vol. 59, no. 19, pp. L1–L13, Oct. 2014.